Application of the Transient Hot-Wire Technique for Measurement of Effective Thermal Conductivity of Catalyzed Sodium Alanate for Hydrogen Storage

Michael Donald Christopher

Thesis submitted to the faculty of the
Virginia Polytechnic Institute and State University
in partial fulfillment of the requirements for the degree of

Master of Science

in

Mechanical Engineering

Dr. Michael Ellis, Chair
Dr. Douglas Nelson
Dr. Michael von Spakovsky

April 15, 2006
Blacksburg, Virginia

Keywords: Effective thermal conductivity, hot-wire, sodium alanate, hydrogen storage, fuel cells

Application of the Transient Hot-Wire Technique for Measurement of Effective Thermal Conductivity of Catalyzed Sodium Alanate for Hydrogen Storage

Michael Donald Christopher

ABSTRACT

Sodium alanate, or the Na-Al-H system, has been the focus of intense research over the past decade due to its ability to hold almost 5 wt% of hydrogen. In this research, the effective thermal conductivity, k, of a sample of titanium-doped sodium alanate is studied over a range of operating conditions pertinent to practical on-board hydrogen storage. A transient technique employing a platinum hot-wire is used to make the measurements. A cylindrical experimental apparatus was designed with the aide of a finite element model that was used to quantify the cylinder boundary effects. The apparatus dimensions were optimized based on the finite element results with the goal of minimizing measurement uncertainty and temperature rise during testing. Finite element results were also used to predict test times and current requirements. A sample of sodium alanate was obtained and loaded into the experimental apparatus which was enclosed in a pressure vessel with a controlled atmosphere. Effective thermal conductivity was measured as a function of pressure at the fully-hydrided and fully-dehydrided states. The results from the pressure-dependence investigation were compared to an existing study that utilized an alternate measurement technique. The results matched well qualitatively – the effective thermal conductivity was highly dependent on pressure, and was found to be significantly higher in the fully-dehydrided state. However, the results of this study were 20 to 30% lower than the existing available data. Additionally, an exploratory investigation used the pressure-composition isotherm (PCI) technique to study the effect of varying composition between the fully-hydrided state and the intermediate decomposition step at a relatively constant pressure. Effective thermal conductivity did not vary significantly over this range of composition.

ACKNOWLEDGEMENTS

I would like to thank Dr. Darlene Slattery at the Florida Solar Research Center for synthesizing and doping the sodium alanate used in this work. Without her willingness to help and expertise, this project would not have happened.

I would also like to thank Dr. Paul Deck and his graduate student Brian Hickory for providing access their glovebox.

I would also like to thank Josh Sole and Ken Henderson for many interesting discussions about metal hydrides and fuel cells. The opportunity to explain my work to others undoubtedly helped me understand many things I would otherwise have no clue about. And of course thank you to Josh for helping me collect data while I was 300 miles away from Blacksburg.

Finally, I would like to thank Dr. Mike Ellis for his guidance and determination to find the right answer to every problem.

TABLE OF CONTENTS

LIST OF TABLES

LIST OF FIGURES

NOMENCLATURE

C	specific heat
C_H	metal hydride composition
d	molecule diameter
D	diameter
dt	time step
d_{wire}	diameter of wire
Ei	exponential integral
i	current
k	effective thermal conductivity
Kn	Knudsen number
L/D	ratio of cylinder length to diameter
L_0	undistrubed length
L_C	characteristic length
m	slope of linear fit
N	number of points in linear fit
N_A	Avagadro's number
N_{FE}	number of time steps in finite element model
P	pressure
Q	energy input to wire
Q'	heat flux per unit length
q_0	boundary heat input per unit area
r	radius
r_{wire}	radius of wire
R_G	universal gas constant
R	resistance
R_0	nominal resistance
T	temperature
t	time
t_{bnd}	time for heat to reach outer boundary
V	voltage
α	temperature-resistance coefficient of platinum
γ	Euler's constant
κ	thermal diffusivity
λ	mean free path of gas molecules
ρ	density
σ	uncertainty
τ	natural log of time

1 INTRODUCTION

Hydrogen and fuel cells present an attractive opportunity to end society's dependence on fossil fuel use and have been the focus of intense study over the past decade. In particular, the Proton Exchange Membrane Fuel Cell (PEMFC) has been at the forefront of research for vehicular applications. The potential for zero emissions at the point of use and the eventual transition to renewable sources of hydrogen are two of the main reasons for the focus on fuel cell technologies.

One of the major technological barriers facing large-scale implementation of fuel cells in vehicular applications is effective on-board storage of hydrogen [1]. In order to compete with gasoline as an energy carrier in passenger vehicles, hydrogen storage systems must meet requirements for energy densities, refueling time, durability, and other criteria. Table 1-1 presents selected parameters from the FreedomCAR and Fuel Partnership, a collaboration between the Department of Energy, U. S. Council for Automotive Research and several major energy companies [2].

Demonstrated technologies for storing hydrogen on-board vehicles such as compressed gas, cryogenic liquid and low temperature metal hydrides are not able to meet all of the requirements set out in Table 1-1 due to fundamental physical limitations [3]. Compressed gas tanks, even those at 10,000 psi, are not able to meet the volumetric storage requirement, and higher pressures are considered impractical due to safety concerns and losses to compression work. Additionally, due to non-ideal behavior above 10,000 psi, the mass of tank required increases faster than the rate of added Hydrogen mass. Cryogenic liquid hydrogen storage offers improved volumetric and gravimetric energy density, and concept vehicles have been demonstrated [4]. However, the energy and monetary costs of producing liquid hydrogen and the energy losses due to boil-off are considerable issues. Low temperature metal hydrides offer still better volumetric storage densities as well as low-temperature and low-pressure operation, but are extremely heavy, having system gravimetric storage efficiencies of about 1-2 wt% of hydrogen.

Medium temperature metal hydrides, such as the complex hydride sodium alanate ($NaAlH_4$), show much promise as hydrogen storage media because of their higher

gravimetric storage densities and operating characteristics around the temperature of PEMFC stack waste gas (< 80°C). A major research focus in the field of hydrogen storage in recent years has been improving the storage capacity, release and regeneration rates and cycle stability of these materials, with much of the emphasis on catalyzed sodium alanate. In addition, researchers have been attempting to understand the mechanisms of catalytic action in order to make informed improvements in doping methods and materials. Efforts to develop prototype storage systems using $NaAlH_4$ have only recently begun, and such work requires knowledge of a host of engineering properties of the substance over a wide range of conditions. One of the most important of these properties is thermal conductivity, which plays a significant role in the kinetics of hydrogen absorption and desorption in metal hydride systems.

Table 1-1 Selected FreedomCAR Storage System 2007 Targets [2].

Metric	Minimum
System Hydrogen Storage Capacity (wt%)	4.5%
System Gravimetric Energy Density(kWh/kg) [1]	1.5
System Volumetric Energy Density (kWh/liter) [1]	1.2
Cycle Life (# cycles)	500
Minimum Full Flow Rate (g/s) per kW of FC Output	0.02
Minimum Delivery Pressure (atm-abs)	8
System Fill Rate (kg H_2/min)	0.5

1.1 Fundamentals of Metal Hydrides

Metal hydrides are solid materials that are chemical combinations of metal atoms and hydrogen [5]. They follow the general reaction

$$MH \Leftrightarrow M + \tfrac{1}{2} H_2, \qquad 1.1$$

where *M* is a metallic element or intermetallic compound and is referred to as the substrate of the metal hydride. In common nomenclature, a metal hydride bed is considered charged, or

[1] Based on lower heating value of hydrogen.

"hydrided" when all substrate atoms contain hydrogen (*MH*) and discharged, or "dehydrided" when they do not (*M*). The composition of a metal hydride bed (C_H) ranges between a maximum value ($C_H = H/M$) when the material is fully hydrided and a minimum of zero when the material is fully dehydrided. Composition can also be reported based on the known maximum weight percent of hydrogen in the material. For example, magnesium hydride (MgH_2) is 7.9 % hydrogen by mass, and composition is often reported as some portion of this amount.

The type and combination of elements in a metal hydride has a dramatic effect on its performance and characteristics. There are myriad known combinations of hydrogen and substrate atoms, but not all of these are suitable for hydrogen storage. For a metal hydride to be useful for on-board storage it must be reversible and must be able to release hydrogen within a useful range of temperatures suitable to vehicles. Reversibility as it pertains to metal hydrides is not strictly defined, but typically refers to the ability to charge and discharge a metal hydride repeatedly without reduction in the amount of hydrogen stored.

When classified by chemical structure, metal hydrides are differentiated by their complexity and are referred to as "simple" or "complex." Simple metal hydrides may be either binary compounds such as MgH_2 that are single-element combinations with hydrogen, or intermetallic compounds such as $LaNi_5H_6$. These simple metal hydrides undergo a single decomposition step, following the reaction in Equation 1.1. Complex metal hydrides are characterized by more than one decomposition step. They first decompose into simple metal hydrides and then further decompose into constituent metallic elements following Equation 1.1, with a release of hydrogen during both steps. Complex metal hydrides are often formed of combinations of metallic elements or intermetallic compounds with charged complexes such as alane $(AlH_4)^{+1}$ and borane $(BH_4)^{+1}$.

When classified by thermodynamic performance, metal hydrides are grouped based on operating temperature range. Low-temperature metal hydrides operate near room temperature, releasing hydrogen freely at ambient conditions, and in some cases well below freezing [6]. This is a desirable characteristic for many applications, and low-temperature hydrides have been demonstrated in prototype vehicles [7]. However, low-temperature metal

hydrides also have low gravimetric energy densities, (usually between 0.33 and 0.67 kWh/kg) and thus are extremely heavy. For example, the low-temperature intermetallic hydride $LaNi_5H_6$ will release hydrogen at 15 psig at 12 °C, but storing 5 kg of hydrogen (typical for a passenger vehicle) would require about 180 kg (396 lbs) of the metal hydride material alone. Accounting for the tank required to hold the material and other equipment, the total system mass could be almost double this, resulting in a system with a gravimetric energy density of about 0.5 kWh/kg. On the other end of the spectrum, high-temperature metal hydrides typically have higher storage capacities, but require much higher temperatures to release hydrogen. For example, the high-temperature simple metal hydride MgH_2 can hold 7.9 wt% hydrogen (2.6 kWh/kg), but requires a temperature of 573 K to release hydrogen at 15 psig. Medium-temperature hydrides fall in between these two extremes, releasing hydrogen at or near the operating temperatures of a PEMFC, while having a theoretically high enough capacity to meet the gravimetric energy density goal in Table 1-1.

Under isothermal conditions, metal hydrides exhibit the pressure-composition behavior of a phase change. Figure 1-1 provides an arbitrarily-scaled illustration of this relationship for a single-step decomposition of a metal hydride. Composition is plotted on the *x*-axis and pressure is plotted on a logarithmic scale on the *y*-axis. At a given temperature, the metal hydride will absorb or release hydrogen along a plateau pressure, with a sharp decrease in pressure at low compositions and a sharp increase at high compositions. Termed a pressure-composition-isotherm (PCI), this plot is commonly used by researchers to illustrate the thermodynamic behavior of a metal hydride. Taking the pressure value at the midpoint of each plateau and plotting versus the inverse of temperature results in a Van't Hoff plot, also illustrated in Figure 1-1. This plot displays the temperature-pressure relationship at steady-state conditions and is useful for comparing the behavior of various metal hydrides.

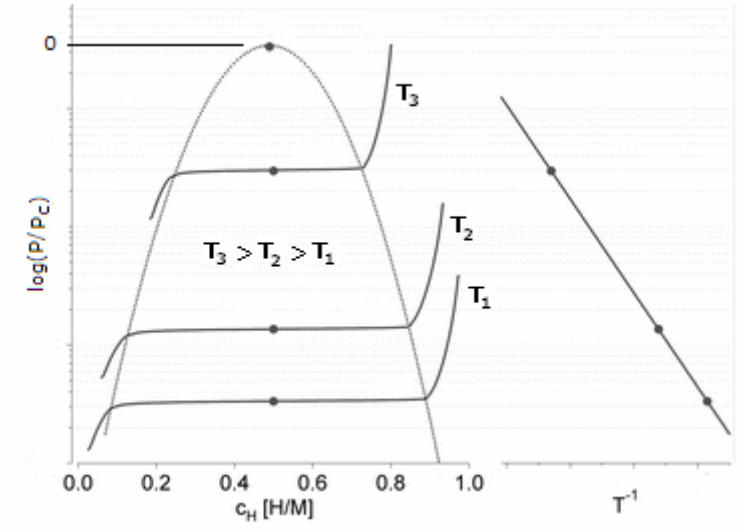

Figure 1-1 Example of pressure-composition isotherms and Van't Hoff plot.

The temperature-pressure behavior of a metal hydride is very important for its practical use. In order to charge a metal hydride, hydrogen gas must be supplied above the plateau pressure at a given temperature. Likewise, hydrogen gas liberated from a metal can only be supplied at or below the plateau pressure. Additionally, the rate of reaction is commensurate with temperature and the difference between over-pressure and plateau-pressure. Therefore, charging and discharging kinetics are dependent on both the temperature and over-pressure.

As with any chemical reaction, there is a heat of formation associated with Equation 1.1. This means that the hydriding reaction is exothermic and the dehydriding reaction is endothermic. In order to maintain a reaction in either direction, the temperature must be maintained by removal or addition of heat corresponding to the heat of formation. A failure to maintain temperature will result in a reduction of the reaction rate. Unless heat is removed during the hydriding reaction, the temperature increase will cause a pressure increase, reducing the difference in over-pressure and the rate of reaction. Unless heat is added during the dehydriding reaction, the temperature decrease will cause a rate reduction through both reaction kinetics and pressure difference. The latter provides a built-in safety mechanism for slowing hydrogen release in case of a tank rupture. In PEMFC vehicles, it is envisioned that stack waste heat can be used in the hydrogen release process, where heat must be added to

maintain adequate release rates. This heat is usually available at or below 80 °C, the typical stack operating temperature. This motivates the development of metal hydride systems for PEMFC vehicles which have acceptable release rates around this temperature.

1.2 Metal Hydride Storage Systems

To create a storage system, a reversible metal hydride in the form of a fine power is packed into a pressure vessel. Some portion of the volume occupied by the powder is made up of the solid particles, and the rest of the volume is made up of voids. The fraction of the total volume that is made up of voids is the porosity of the bed. Hydrogen gas is able to move throughout the voids in the powder and is exposed to the large particle surface area. It has been shown that reduction in particle size improves reaction kinetics by increasing the available surface area [8].

The implementation of any metal hydride in a practical storage system requires knowledge of its engineering properties. Because of the need to transfer heat in and out of the system during reaction, one of the most important of these properties is thermal conductivity. In most prototype systems, heat exchange devices must be used in to improve the transfer of heat into and out of the hydride tank [9]. Typically, one or more internal heat exchange tubes are installed, through which a fluid is passed to add or remove heat. The ability of the metal hydride powder to accept heat from or reject heat to these heat exchange devices is critical to system performance. As explained above, reaction kinetics depend greatly on this ability to transfer heat.

1.3 Effective Thermal Conductivity

Since metal hydrides in storage systems exist as a powder in the presence of hydrogen gas, it is necessary to measure an “apparent” or “effective” thermal conductivity of the powder/gas mixture as opposed to the thermal conductivity of the solid hydride material. The effective thermal conductivity is a combined property of the metal hydride powder and the interstitial gas that is highly dependent on gas pressure. The Knudsen number [10] is a non-dimensional number used to characterize the effect of pressure, and is defined as

$$Kn = \frac{\lambda}{L_C}, \tag{1.2}$$

where λ is the mean free path of gas molecules and L_C is a characteristic length, in this case the average size of pore spaces in between metal hydride particles. An estimate of the mean free path is

$$\lambda = \frac{RT}{\sqrt{2}\pi d^2 N_A P}, \tag{1.3}$$

where R is the universal gas constant, T is temperature, d is molecule diameter, N_A is Avagadro's number and P is pressure.

Figure 1-2 shows a representation of the Kundsen effect. At very low pressures the Knudsen number is much greater than one. Gas molecules have a mean free path that is much larger than the pore size and thus little heat is transferred by molecule to molecule collisions through the gas. This results in a heat transfer path that consists primarily of solid particle-to-particle interactions and presents a convoluted route for the movement of heat, resulting in low effective thermal conductivity. At very high gas pressures the Knudsen number is much less than one. The mean free path of gas molecules is much shorter than the pore spaces and heat is conducted through parallel pathways in gas molecule interactions and solid particles, resulting in higher thermal conductivity. The transitional region between these two extremes occurs when the Knudsen number is close to one, or the mean free path of the gas molecules is on the same order of magnitude as the pore spaces. This phenomenon has been observed in many effective thermal conductivity studies [6, 11, 12]. In general, metal hydrides operate in the transitional regime of the Knudsen effect. Thus, the thermal conductivity can vary dramatically with gas pressure, in some cases an order of magnitude. Additionally, the effective thermal conductivity can vary with particle size and porosity. Smaller particles results in smaller void spaces as well as more solid particle-to-particle interactions per unit volume, increasing effective thermal conductivity. A hydride bed that is more tightly packed has a lower porosity, resulting in more particle-to-particle interactions per unit volume and higher effective thermal conductivity. These effects have important

implications for the development of metal hydride storage systems where heat transfer is critical to maintaining reaction rates.

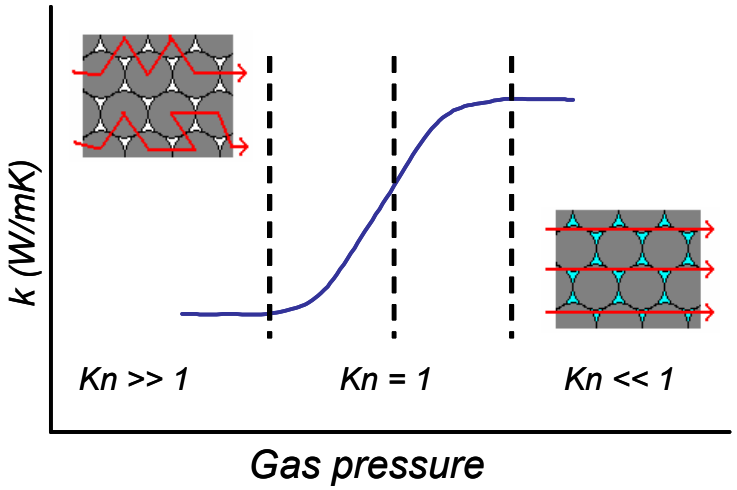

Figure 1-2 Representation of the Knudsen effect.

1.4 Motivation

Sodium alanate, or $NaAlH_4$, is a complex, medium-temperature metal hydride and is the focus of this study. It has a maximum useable capacity of 5.6 wt% hydrogen (1.87 kWh/kg). The decomposition/combination reaction has two steps, as follows:

$$3NaAlH_4 \leftrightarrow Na_3AlH_6 + 2Al + 3H_2 \leftrightarrow 3NaH + 3Al + 4.5H_2 \qquad 1.4$$

This group of interrelated compounds is more conveniently referred to as the Na-Al-H system. Since $NaAlH_4$ exists alone only at a fully hydrided state, it can be misleading to refer to the entire system by its compound name. Under different conditions, the Na_3AlH_6, NaH and Al phases can exist in various ratios.

This system is not inherently reversible, but recent research has shown that adding small amounts of titanium catalyzes the reaction steps and makes the compound reversible [13]. This advance gives the Na-Al-H system much promise as a solid-state hydrogen storage material. Because the thermal properties of any prospective metal hydride are extremely important, the goal of the current study is to investigate the effective thermal

conductivity of this material over a range of practical operating conditions including pressure, temperature, and composition. The extent to which the effective thermal conductivity varies with these parameters is vital to development of its use in on-board storage applications.

Although thermal conductivity studies have been performed previously on other materials [6, 14-17], only one such study exists for the Na-Al-H system [12]. In this study, the thermal probe method (based on the ASTM D 5334-00 standard) was applied to a cylindrical bed of sodium alanate. The current work extends these existing results in two ways. First, the use of the hot wire method will provide verification of the results from Dedrick [12] through an alternate measurement technique. Second, this work aims to contribute to the base of knowledge of the Na-Al-H system through an exploratory investigation into the relationship of composition and effective thermal conductivity. These results will be directly applicable to the design and prototyping of storage systems using sodium alanate.

1.5 Summary

The promise of renewable and zero-emissions fuels for vehicular transportation is the impetus for a growing body of research into hydrogen and fuel cells. Metal hydrides offer the potential for a practical form of on-board hydrogen storage. Sodium alanate is one of the most promising metal hydrides currently under study, and detailed knowledge of its thermal properties is a valuable contribution to realizing practical fuel cell vehicles.

The following chapter presents a review of available literature on sodium alanate and thermal conductivity measurement techniques. This review will provide a historical context, demonstrate the uniqueness of this study, and collect and present important information from previous research. Chapter 3 will describe the analytical approach used to design the measurement apparatus, while Chapter 4 will detail its construction. Chapter 5 presents details of the experimental investigation, and Chapter 6 the resulting data. Chapter 7 will summarize the findings and make conclusions and recommendations for future work.

2 LITERATURE REVIEW

Sodium alanate, or the Na-Al-H system, holds much promise as a viable alternative to gaseous and cryogenic liquid for on-board storage of hydrogen in vehicles. This chapter aims to provide a historical context, demonstrate the uniqueness of this study, and collect and present important findings from other research. First, this chapter will outline the major milestones and improvements in the development of the Na-Al-H system, which has been ongoing for almost a decade. Then, the benefits and drawbacks of several thermal conductivity measurement techniques are discussed, with emphasis on measurements on metal hydrides and similar porous materials.

2.1 Developments in the Na-Al-H System

Over the past nine years, interest in the Na-Al-H system has steadily gained momentum, and so have the number and variety of synthesis methods, doping methods, catalysts and other additives. Knowledge of these methods is important in obtaining or synthesizing material for this work. A brief history and a summary of the state-of-the-art in the Na-Al-H system are presented.

A breakthrough paper in 1997 by Bogdanovic and Schwickwardi [13] showed the Na-Al-H system could be made reversible by the addition of the titanium-based precursors $TiCl_3$ and $Ti(OBu^n)_4$[1]. Prior to this work, it was held that $NaAlH_4$ and Na_3AlH_6 were non-reversible metal hydrides. The selected dopants were added through a solvent-mediated, or "wet" chemical method. It was shown that the organic catalyst $Ti(OBu^n)_4$[1] was superior to the inorganic β-$TiCl_3$, although reduction in reversible capacity was observed upon repeated cycling, indicating some kind of morphology changes in the bed.

Two years later, the groups of Zaluski [8] and Huot [18] independently showed that high-energy ball milling could improve the kinetic performance of the Na-Al-H system beyond that achieved by Bogdanovic and Schwickwardi without the use of catalysts. Their synthesis methods used no solvents and are thus considered "dry" techniques. These works showed that a reduction in particle size is also an effective method to improve the

[1] Titanium tetra-n-butoxide, $Ti(OCH_2CH_2CH_2CH_3)_4$

performance of sodium alanate. Furthermore, the work of Jensen [19] showed that dry synthesis techniques enhanced the kinetic performance as well as the cycle stability over wet synthesis techniques.

Efforts to improve catalysis continued with the investigation of zirconium-based organic catalysts [20]. While the $Zr(OPr)_4$[1] catalyst was found to be inferior to titanium for catalysis of the first decomposition step of $NaAlH_4$, it was found to be superior for the catalysis of the second decomposition step. A combination of the two catalysts yielded a reversible capacity greater than 4 wt% and improved kinetics in both reaction steps. Figure 2-1 shows a comparison of this work with that of Bogdanovic and Schwickwardi [13]. Furthermore, work by Gross [21] confirmed the kinetic enhancements of titanium-zirconium doping through in-situ X-ray diffraction measurements, although the role of the catalysts was still not understood. Their study examined the phase evolution of sodium alanate, as seen in Figure 2-2 (*y*-axis is normalized to full-scale for each plot). They noted the two decomposition steps are interdependent; the reaction of Na_3AlH_6 to NaH and Al only proceeds once the $NaAlH_4$ to Na_3AlH_6 reaction is near completion. The discovery of an aluminum crystallite phase led to the conclusion that long-range transport of metal species takes place during the decomposition reaction. Separate X-ray diffraction work by Bogdanovic [22] showed that reduction in storage capacity due to cycling was due to this aluminum species not bonding with Na_3AlH_6 to form $NaAlH_4$ at the end of the hydrogenation process.

[1] Zirconium tetra-n-propoxide, $Zr(OCH_2CH_2CH_3)_4$

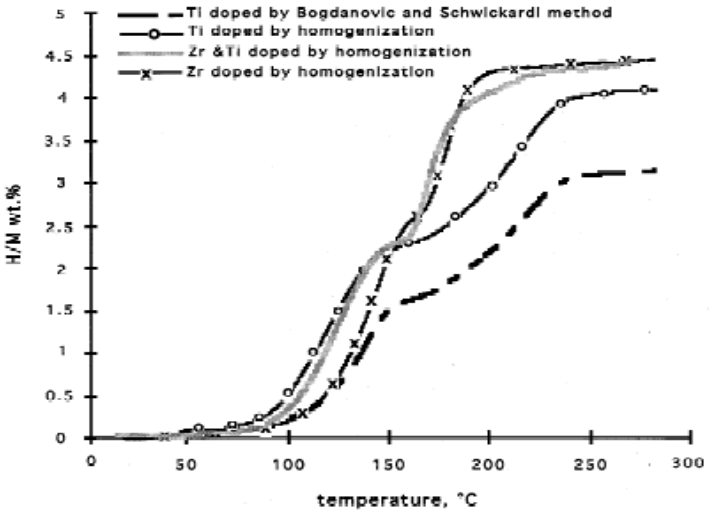

Figure 2-1 Comparison of desorption results [21].[1]

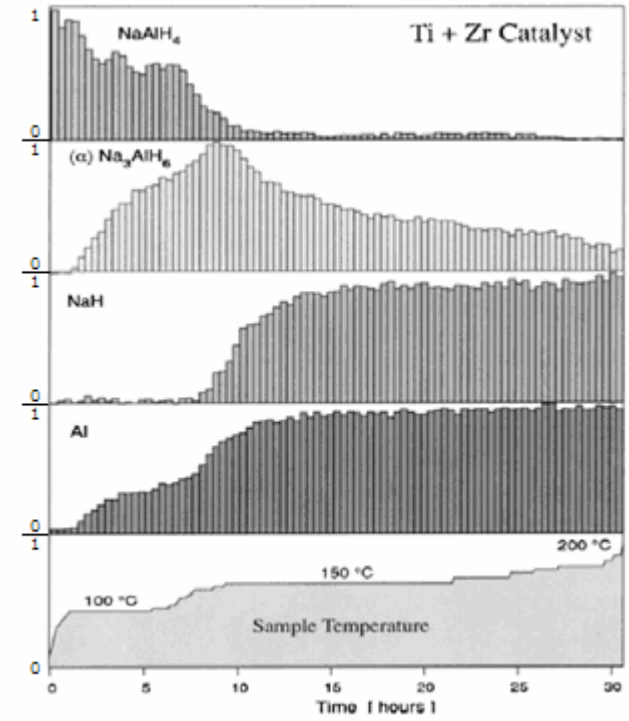

Figure 2-2 Phase composition of sodium alanate [21].[1]

Further enhancement of the performance of the complex hydride sodium alanate focused for some time on improving the reaction kinetics through addition of different

[1] Reprinted with permission from Elsevier.

catalysts and other additives. Numerous catalysts have been tested by various groups [21, 23-28], with an emphasis on formulations of titanium.

The work of Gross [26] described the state-of-the-art formulation at the time of writing in 2002 and the associated performance - reversible capacity exceeded 4.2 wt%, with 3 wt% available in 1 hour of desorption at 125 °C. They also showed measurable release rates near room temperature for the first time. Doping methods were developed using inorganic catalysts such as $TiCl_3$ that not only improved kinetics and storage capacity, they eliminated the impurities associated with using traditional organic formulations of titanium.

An important study in 2003 demonstrated much improved performance in the Na-Al-H system when using titanium nanoparticles as a catalyst. Bogdanovic [28] doped sodium alanate with colloidal titanium nanoparticles and found this formulation to improve storage capacity and kinetics significantly over previous work. In the first few cycles, the material could be hydrogenated to almost 5 wt% in less than 15 minutes. Continued cycling showed an increase in the hydrogenation time to 100 minutes, but a leveling off of storage capacity around 4.5 wt%.

Graphite was shown to have a synergistic effect with titanium on performance in the Na-Al-H system in a paper by Wang [29] in 2005. The addition of 10 wt% graphite powder to a titanium-doped sample decreased the dehydrogenation temperature in the 95-150 °C range by 15 °C over the titanium-doped sample alone. Graphite alone was shown to have a negligible impact, however. Improvements in desorption rates up to six times better than titanium-doping alone were observed in the sample with graphite. The combination of graphite with the $TiCl_3$ catalyst formulation showed especially good results, and noted by the authors to be perhaps the best performance ever seen for the Na-Al-H system. The obvious drawback to the addition of graphite is the reduction of overall hydrogen capacity. It was noted that graphite had no catalytic effect on its own; it was only in combination with titanium that the improved performance was seen. Investigation into the mechanisms of the catalytic action of graphite is ongoing.

2.2 Thermal Conductivity Measurement Techniques

Several well-known thermal conductivity measurement techniques have previously been applied to various metal hydride materials. These include steady-state methods [30, 31], and transient methods using either the hot wire [6, 11, 32] or the thermal probe [12, 33] technique. Additionally, some applications of these techniques to materials other than metal hydrides have yielded important results [14, 15]. A summary of important results from these investigations is presented at the end of this section in Table 2-1.

Suda [30] measured the effective thermal conductivity of $TiMn_{1.5}$ metal hydride powder using a steady-state apparatus. Their device used an array of thermocouples to measure the radial temperature gradient in a cylindrical vessel with a differential temperature of 21 or 38 °C. The dependence of thermal conductivity on pressure, mean temperature and hydride composition was investigated. The thermal conductivity was found to increase with pressure in accordance with the Knudsen effect, although the hydride exhibited hysteresis between absorption and desorption processes. They also found the thermal conductivity increased linearly with increasing hydride composition. Their results were summarized in an empirical expression as a function of pressure and composition.

In another study, Suissa [31] used a similar steady-state method to investigate the thermal conductivity of Mg_2NiH_4 and $MmNiFeH_{5.2}$ (Mm = Mischmetal) metal hydrides as a function of temperature and pressure. Their conclusions matched closely with those of Suda [30]. They found a very small temperature-dependence and a linear-dependence on hydride composition. Their conclusions also showed that the thermal conductivity rose with pressure to 1 W/mK but remained at that level once the pressure rose above about 40 atm. This observation can be attributed to the transitional and high-pressure regimes of the Knudsen effect.

Ishido [11] used the transient hot wire method to study the effective thermal conductivity of magnesium hydrides (Mg, Mg/10wt%Ni, Mg_2Ni). Their transient test method produced only a small temperature change, allowing them to measure thermal conductivity at specific temperatures. A 0.3 mm nichrome wire was embedded in a cylindrical bed 5 cm in diameter and 15 cm in length and heated to create the transient

response. A furnace maintained the outer wall temperature of the vessel and a thermocouple spot welded to the center of the wire recorded temperature. The effective thermal conductivity was measured as a function of pressure, temperature and fractional solid content (1/porosity). Figure 2-3 shows the results for the Mg_2Ni hydride over the full range of variables. The thermal conductivity was found to increase with fractional solid content and pressure, but the relationship with temperature was dependent on hydride type and fractional solid content.

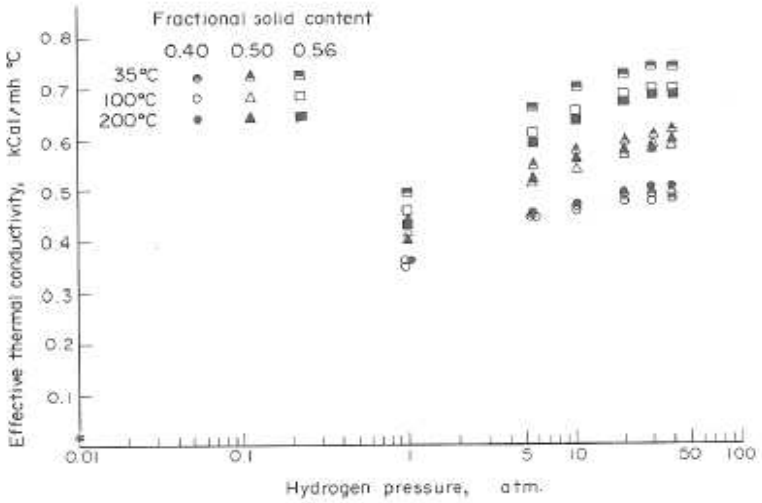

Figure 2-3 Results from Ishido [11].[1]

Hahne and Kallweit [6] also utilized the transient hot wire method, but in a slightly different configuration. They used a heating wire made of platinum, which doubled as a resistance-based temperature measurement. The effective thermal conductivity of $LaNi_{4.7}Al_{0.3}H_5$ and the commercial hydride HWT 5800 was measured over a wide range of pressures and included tests with and without hydride formation. The apparatus used was a cylindrical vessel with a central platinum heating wire of 0.2 mm diameter that kept the temperature rise to below 1 K. Two additional thermocouples were used to verify the temperature homogeneity of the bed before and during testing. Effective thermal conductivity was measured over a temperature range of -80 to 140 °C and a pressure range of

[1] Reprinted with permission from the International Journal of Hydrogen Energy.

10^{-6} to 60 bar. Four different fill gases were used, with hydrogen giving the highest effective thermal conductivity, as expected. The powders were tested in the as-delivered state without hydride formation, activated through procedures specified by the manufacturers, and then tested with hydride formation. It was found that over the range of pressures tested, the effective thermal conductivity varied by three orders of magnitude. These results strongly resemble the work of others [11], having the characteristic pressure-dependent "S" shape due to the Knudsen effect. For the tests with hydride formation, pressure-composition isotherm (PCI) curves were produced, with thermal conductivity measurements taken at each composition point (Figure 2-4). The PCI curves provided the data to examine the effects of pressure and composition separately, as well as combined with the results of the non-hydride formation results. Figure 2-5 shows these combined results plotted against pressure, where the upper curve is the pressure dependency at the fully hydrided state, the lower curve is the pressure dependency at the fully dehydrided state, and the curves in between are the PCI results.

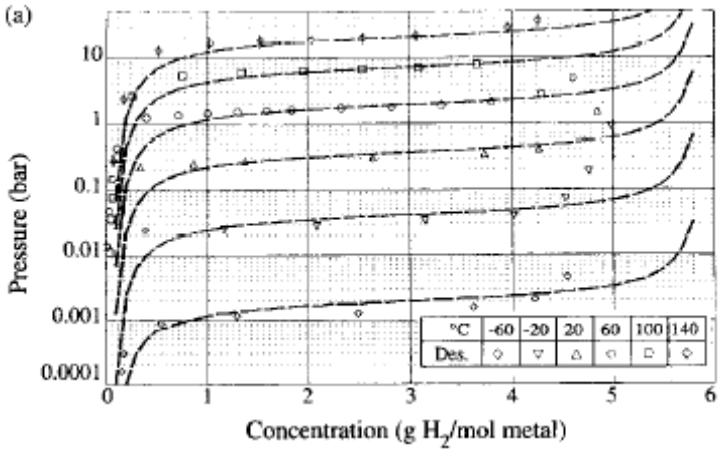

Figure 2-4 PCI curves taken during tests with hydride formation [6].[1]

[1] Reprinted with permission from the International Journal of Hydrogen Energy.

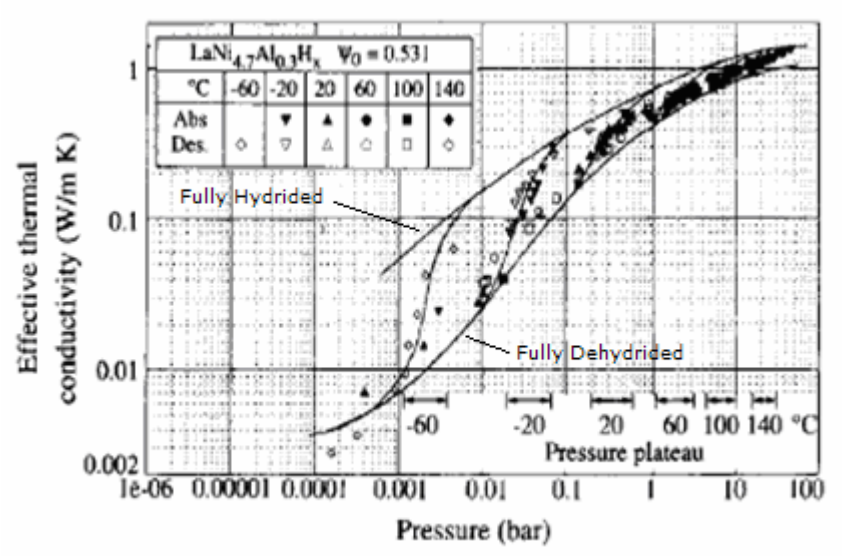

Figure 2-5 Combined results of tests with and without hydride formation [6].[1]

Several others have used the transient hot wire technique to study zeolites. The results are directly applicable to the current study due the similarity between zeolites and metal hydrides. Both are porous materials with similar ranges of effective thermal conductivity values. In fact, zeolites have been proposed as hydrogen storage materials because of their ability to adsorb hydrogen.

Liu [14] developed a method for measuring the effective thermal conductivity of zeolite bricks with adsorbed water using the transient hot wire method. A constantan wire of 0.127 mm diameter was used as a heat source while a separate thermocouple measured temperature. The transient temperature response was used to determine the thermal conductivity based on a linear fit of the temperature versus ln(*time*) data. An important observation is that the tests strived to minimize the temperature increase, power input and test time to avoid desorbing water from the zeolite material. Samples were approximately 7 cm long and 3 cm in width with test times running up to several hundred seconds. Teflon bricks were used as a reference material, and good agreement was found with published values.

[1] Reprinted with permission from the International Journal of Hydrogen Energy.

More recently, Griesinger [15] employed the transient hot wire method to measure the effective thermal conductivity of zeolite materials with adsorbed hydrogen in powder form. The apparatus was a platinum wire of diameter 0.2 mm embedded in the center of a cylindrical vessel filled with powder. The effects of different fill gases were investigated across pressures from 0.001 to 10 bar and temperatures from 210 to 550 K. The effect of particle size was also investigated and it was found that thermal conductivity was higher for large, spherical particles. As seen in Figure 2-6, the thermal conductivity of a sample consisting of 3.88 mm spheres was only weakly dependant on pressure. For the finer powders, however, the pressure effect is much more pronounced. In general, it was found that the thermal conductivity was highly dependent on all three parameters, increasing with both increasing pressure and temperature. They also investigated the effect of the number of storing cycles and the addition of graphite powder. Thermal conductivity was not significantly affected by the number of storing cycles. However, it was increased significantly by the addition of graphite, as seen in Figure 2-7. The addition of even 10 wt% of graphite powder increased the thermal conductivity by roughly 50 %.

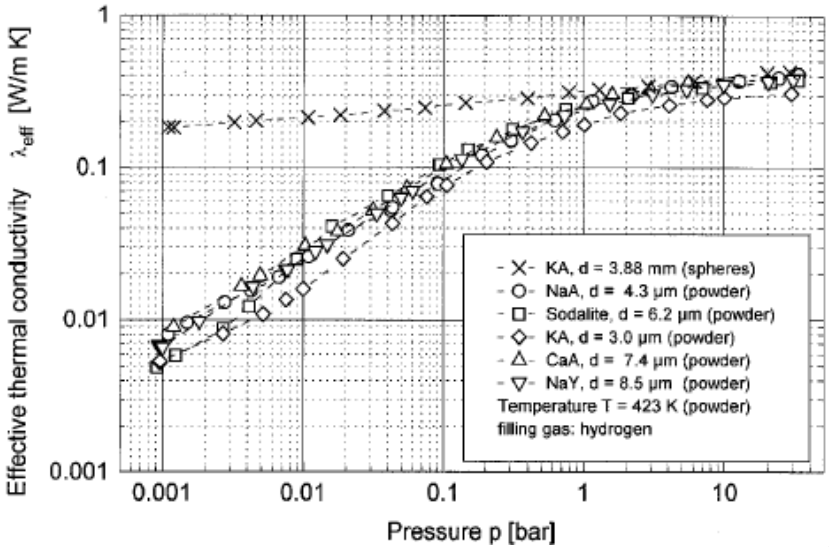

Figure 2-6 Effect of particle size on *k* of zeolite powders [15].[1]

[1] Reprinted with permission from Elsevier.

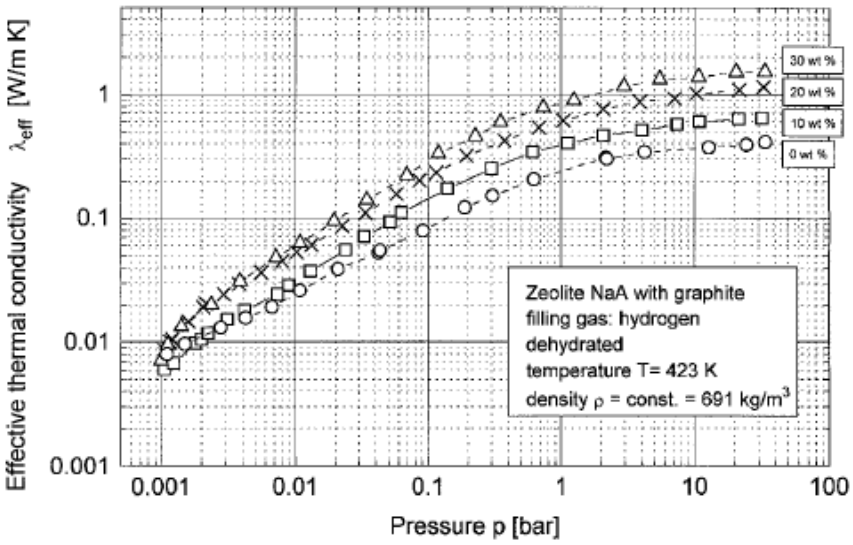

Figure 2-7 Effect of graphite powder on *k* of zeolite powders [15].[1]

The ASTM C 1113-99 standard [32] addresses the measurement of thermal conductivity of both bricks and powders using a transient hot wire method. Similar to other works [14], the ASTM standard recommends a separate thermocouple to measure temperature and a platinum heating wire of diameter 0.330 to 0.508 mm. The specimens are standardized to 22 cm in length with a width as large as allowable by the test equipment. No information is provided on validation using a reference sample.

In a recent study, Dedrick [12] used another transient technique, the thermal probe method, to study the thermal conductivity of the Na-Al-H system in detail for the first time. The researchers used a method based on the ASTM D 5334 protocol [33] and examined the effective thermal conductivity in terms of several conditions: cycle number, composition, pressure and temperature. The probe design relies on the same assumptions for a line source used in the hot wire technique but calls for encasing a nichrome heater wire and separate thermocouple in a stainless steel tube. The test vessel was a cylindrical chamber instrumented with radial thermocouples used to validate the numerical model utilized in its design. It was found the radial thermocouples had a deleterious effect on the measurement of higher conductivity values, and they were removed. The probe and vessel were validated

[1] Reprinted with permission from Elsevier.

using three reference materials (Teflon, polyurethane foam and Ottawa sand), and found to give values that matched closely with published values for the materials.

Results from Dedrick [12] are presented in Figure 2-8, which shows the effect of phase composition and pressure on effective thermal conductivity. The phase of the hydride clearly has an effect on the thermal conductivity. The improvement in thermal conductivity at vacuum with cycle number suggests sintering and other activation changes induced by cycling. With pressure held above the plateau pressure of the sodium alanate to prevent desorption, the thermal conductivity was measured for temperatures from 22 to 130 °C. Temperature was found to have little effect, varying less than 6% for all measurements. All pressure measurements were made at room temperature, again to prevent desorption during testing. As expected, thermal conductivity was highly dependent on pressure and displayed Knudsen behavior. In order to eliminate the chance that hydrogen was reacting with the material and producing misleading results, the researchers duplicated the test using Helium gas, which demonstrated similar Knudsen behavior. The thermal conductivity proved to be highly dependent on the alanate phase present. The fully desorbed state (NaH + Al) had the highest thermal conductivity, while the fully absorbed state had the lowest. It was proposed that this was due to the presence of free aluminum particles in the bed. It was noted that because the particular formulation used had excess free aluminum in the fully absorbed state, pure $NaAlH_4$ would have an even lower thermal conductivity than was measured. With a second batch of sodium alanate using smaller aluminum particles, it was found the effective thermal conductivity was significantly enhanced. Additionally, a finite element model allowed determination of the wall contact resistance at both the probe/hydride and wall/hydride interfaces through an iterative refinement technique. Contact resistance was measured in the fully absorbed state under two different hydrogen pressures and in the desorbed state under two different helium pressures, as well as at vacuum. It was found that between the probe and alanate, the contact resistance was in the range of 300 to 560 W/m^2K, while between the wall and alanate, the contact resistance was only 30 to 150 W/m^2K. It was observed that contact between the probe and alanate was much better than at the wall interface, most likely due to changes in bed geometry due to cycling. No strong correlations are observable from the data provided. The finite element model also permitted the determination of high effective thermal conductivity values (>0.7 W/mK), where the

geometry of the apparatus prohibited direct measurement due to interference from radial-located thermocouples. Details of the model were not provided.

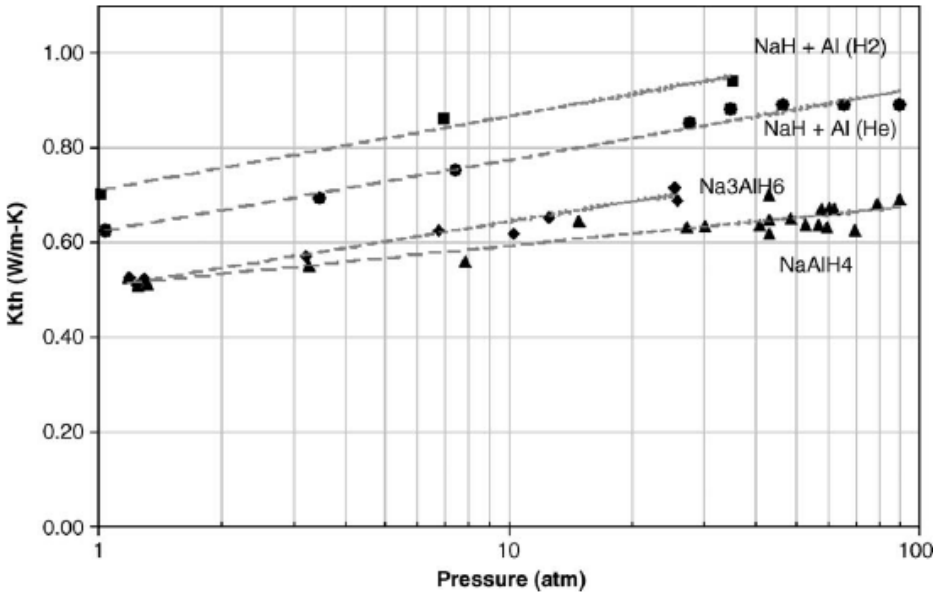

Figure 2-8 Effect of phase composition and cycle number [12].[1]

Manohar [17] studied the validity and uncertainty of the thermal probe method, based on the ASTM D 5334 protocol. Their analysis shows the uncertainty in measuring low thermal conductivity samples is predominantly dependant on the slope of the linear fit ($dT/d\ln(t)$) and not on the voltage and current measurements, which have negligible uncertainty by comparison. Their probes were constructed of 3mm OD stainless steel tubes with a heater wire and thermocouple embedded inside, and demonstrated a repeatability of ±3.5%. They tested sand and soil samples for 1000 s in a 10.8 cm diameter by 20 cm high cylindrical vessel.

2.3 Summary

Table 2-1 presents a summary of important information from the effective thermal conductivity investigations reviewed here. The limitations of the steady state method for

[1] Reprinted with permission from Elsevier.

measuring thermal conductivity include large temperature differentials across the bed and the invalidation of the assumption of a homogenous bed by the thermocouples necessary to measure the temperature gradient. Transient techniques are more attractive for use in this study due primarily to short test times, but also because of the small temperature differential (both in space and time). Although it has been shown temperature by itself does not have a large effect on the effective thermal conductivity of $NaAlH_4$ [12], temperature-induced changes in composition can affect thermal conductivity. The hot-wire method with an independent temperature probe has often been used historically, but is improved upon by the use of a platinum wire serving a dual purpose as heating source and resistance-based temperature measurement. The removal of the extraneous temperature measurement device, such as a thermocouple, creates an apparatus that more closely approximates a homogenous bed.

Table 2-1 Summary of results from effective thermal conductivity investigations.

	Suda [30]	Suissa [31]	Ishido [11]	Hahne [6]	ASTM C 1113 [32]	Dedrick [12]	ASTM D 5334 [33]	Griesinger [15]	Liu [14]
Method	Steady state	Steady state	Transient hot-wire	Transient hot-wire	Transient hot-wire	Thermal probe	Thermal Probe	Transient hot-wire	Transient hot-wire
Material	$TiMn_{1.5}$	Mg_2NiH_4 $MmNi_4FeH_{5.2}$[1]	MgH_2 Mg_2NiH_4	$LaNi_{4.7}Al_{0.3}H_x$[2] HWT 5800[3]	n/a	$NaAlH_4$	n/a	Zeolites	Zeolites
k range (W/mK)	0.25-1.3	u/k	0.8-1.4	0.01-1	n/a	0.5-0.9	n/a	0.01-1.5	0.24-0.24
P range (bar)	0.5-50	u/k	1-50	10^{-6}-60	n/a	1-100	n/a	10^{-5}-50	u/k
T range (°C)	30-50	u/k	30-200	-80-140	n/a	22-130	n/a	-60-180	22-33
Test time (s)	u/k	u/k	u/k	100	5-10 min	100-1000	n/a	100	15-360
Wire Diameter (mm)	n/a	u/k	0.3	0.2	0.330-0.508	n/a	n/a	0.2	0.127
Sample Length (cm)	u/k	u/k	15	u/k	22	u/k	n/a	u/k	7
Sample Diameter (cm)	14	u/k	5	u/k	n/a	u/k	n/a	u/k	n/a
Ratio of Length to Diameter	u/k	u/k	3	u/k	u/k	u/k	u/k	u/k	u/k

[1] Mm = Mischmetal
[2] $x_{max} = 6$
[3] $Ti_{0.98}Zr_{0.02}V_{0.43}Fe_{0.09}Cr_{0.05}Mn_{1.5}H_x$; $x_{max} = 2.982$

The thermal probe method is advantageous because of the physical robustness of the probe itself, which can be inserted into a sample in-situ. However, this ability is not crucial in a laboratory setting where in-situ measurements are not required. Because the probe method is essentially the hot-wire method in an integrated package, it does not offer any other advantages over the basic hot-wire technique. In fact, it may be detrimental, as the sheath required to house the apparatus greatly increases the radius of the heat source, and the encased heating wire may not distribute the heat flux evenly. Increasing the radius of the probe reduces the validity of the assumption of an infinitely thin wire, which is required for the idealized physical model. The lack of radial symmetry in the probe could also cause non-uniform distribution of heat, invalidating another assumption of the physical model. The best solution and one that is easily adaptable to the measurement of sodium alanate powder is the platinum hot-wire method with integrated temperature measurement. This method will therefore be used in the current study. The literature suggests the wire have a diameter between 0.2 and 0.5 mm.

The work of Hahne and Kallweit [6] is one of the most thorough investigations of effective thermal conductivity of a metal hydride. Their use of the PCI curve to study the interrelated effects of pressure, temperature and composition reflects a motivation to understand effective thermal conductivity in terms of practical operating conditions. In addition, the PCI curve is commonly used by researchers developing metal hydride materials, and is thus a common tool for understanding metal hydride behavior in general. For these reasons, the current study will emulate this approach with the Na-Al-H system.

Sodium alanate has been the focus of intense research, if not for its potential for improvement, then for its role in helping researchers learn how to tailor metal hydrides to a specific need. At the very least, the Na-Al-H system will serve as an invaluable model for development of a host of new hydrides at the forefront of research [34-36], and could conceivably provide a viable solution given continued improvements in performance through synthesis and catalysis methods. For these reasons and for those of familiarity and accessibility, $NaAlH_4$ was chosen as the focus of this study. However, this work is directly applicable to other metal hydride materials, porous materials, or even liquid- or slurry-based hydrogen storage systems.

Chapter 3 will discuss the analytical approach and design of the test apparatus using finite element methods. The results of that design are applied to the construction of the hot-wire apparatus, described in Chapter 4. The experimental approach is discussed in Chapter 5, followed by results in Chapter 6.

3 APPARATUS DESIGN

This chapter describes the analytical investigation undertaken in the design of the effective thermal conductivity measurement apparatus. First, the transient hot wire measurement technique is explained. Then, a description of the finite element approach used in the design is given. Finally, the finite element results were used to assign optimal dimensions to the sample cylinder and predict electrical current requirements and test times for various values of *k*.

3.1 Measurement Technique

The transient hot wire method is used in this study based on information described in the literature review. This technique assumes an idealized linear heat source that is infinitely long and thin and undergoes a step input in electrical power at $t = 0$. Based on assumptions described in this section, the ideal equations are used as an approximation for a wire of finite radius which is a non-ideal source.

3.1.1 Theoretical Basis

Carslaw and Jaeger [37] show that the transient temperature response at a distance *r* from an ideal continuous linear source in an infinite homogenous medium is:

$$T = \frac{q}{4\pi\kappa} \int_{r^2/4\kappa t}^{\infty} \frac{e^{-u}\,du}{u}, \text{ and} \qquad 3.1$$

$$q = \frac{Q'}{\rho C}, \qquad 3.2$$

where κ is the thermal diffusivity of the medium ($\kappa = k/\rho C$), ρ is the density of the medium, *Q'* is the heat flux per unit length of the linear source, *C* is the effective specific heat of the medium and *k* is the effective thermal conductivity of the medium. This equation has a solution which takes the form shown in Figure 3-1. For times greater than zero, the temperature increases in the infinite medium. The temperature is always at a maximum at the ideal linear source and decreases with increasing *r*. At a given time, the influence of the

heat produced by the ideal linear source reaches some maximum value of r. This heat flux boundary moves outward to greater values of r as time increases.

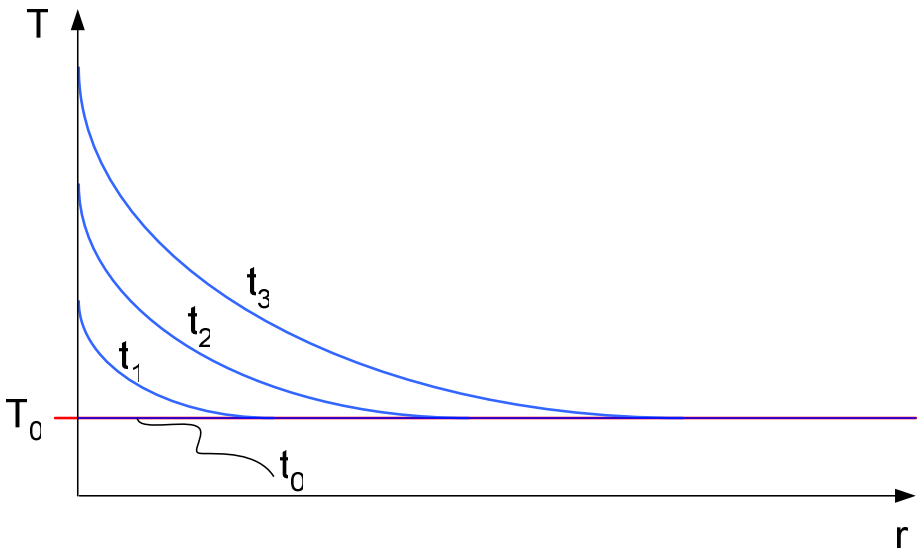

Figure 3-1 Form of the solution of Equation 3.1

The integral in the Equation 3.1 is also known as the exponential integral:

$$Ei(x) = -\int_{-x}^{\infty} \frac{e^{-u}\,du}{u}, \text{ or} \qquad 3.3$$

$$-Ei(-x) = \int_{x}^{\infty} \frac{e^{-u}\,du}{u}. \qquad 3.4$$

where $x = r^2/4\kappa t$.

Figure 3-2 describes the relationship of x and k over the range of wire radii suggested by the literature and for several orders of magnitude of k. The density and specific heat, ρC, for sodium alanate are known from the literature [12]. The term x is very small even in the worst case and several orders of magnitude smaller for values of k in the range expected for the Na-Al-H system. Therefore, at times greater than one second, x is assumed to be insignificantly small. An approximation for $Ei(x)$ for small values of x is taken from [37]:

$$Ei(-x) = \gamma + \ln x + x + \tfrac{1}{4}x^2 + O(x^3)\,, \tag{3.5}$$

where γ is Euler's constant (~0.522). Calling on the same assumption used above, the last two terms in Equation 3.5 are assumed insignificant relative to the first two. Substituting for x yields,

$$T = \frac{Q'}{4\pi k}\left[-\gamma + \ln\left(\frac{4\kappa t}{r^2}\right)\right]. \tag{3.6}$$

Simplifying,

$$T = \frac{Q'}{4\pi k}\ln t + \frac{Q'}{4\pi k}\ln\frac{4\kappa}{r^2} - \frac{Q'\gamma}{4\pi k}\,. \tag{3.7}$$

Taking the derivative of T with respect to ln(t) we find,

$$\frac{dT}{d(\ln t)} = \frac{Q'}{4\pi k}\,. \tag{3.8}$$

Solving for k,

$$k = \frac{Q'}{4\pi}\left(\frac{dT}{d(\ln t)}\right). \tag{3.9}$$

It is clear that Equation 3.9 can be used to calculate k directly from experimental data and therefore will be the basis of the measurement technique used here. However, this formula must not be used for very short times based on the assumptions above, and should be restricted to times greater than one second past the start of wire heating.

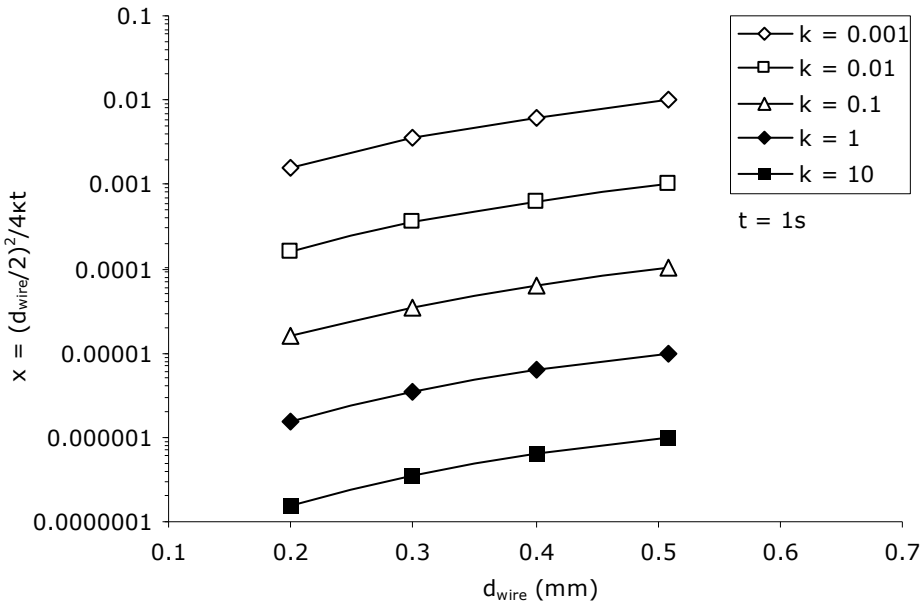

Figure 3-2 Relationship of the parameter x to wire diameter and k for t = 1s.

3.1.2 Test Apparatus Concept

From Equation 3.9, the effective thermal conductivity of a sample can be determined experimentally using an instantaneous linear heat source while measuring the power output of the source and the change of wire temperature with time. Thus, the core of the apparatus is a wire that approximates the linear heat source of Equation 3.2. When a current is passed through the wire, its resistance converts the electrical energy into heat through Joule heating. It is assumed this will produce a constant heat flux per unit length, *Q'*, increasing the temperature of the surrounding bed (see Figure 3-3). It is also assumed that all the electrical energy dissipated in the wire by its resistance is converted to heat and is transmitted to the test bed. An additional assumption is that the effects of convection and radiation are insignificant compared to the effects of conduction. By keeping the test apparatus vertical, the temperature gradients induced by the heating of the wire will be perpendicular to the force of gravity, thus preventing natural convection. It has been noted in another study that the measurement of "effective" thermal conductivity should capture the effects of heat conduction through solid particles and gas as well as radiation across the pores [6]. Since it is not clear what contribution radiation makes to the effective thermal conductivity measurement, here it is assumed that by minimizing its effects, its contribution to effective

thermal conductivity can be considered insignificantly small. To minimize radiation effects, the applied current is kept as low as possible; a practice used in similar thermal conductivity studies [6, 12]. Furthermore, it is assumed that the majority of the current flow is carried by the wire, and that any current that flows into the bed will travel parallel to the wire. The thermal conductivity of Platinum is 71.6 W/mK, or roughly two orders of magnitude greater than the expected effective thermal conductivity of the bed. Because electrical conductivity is typically proportionate to thermal conductivity, current flow in the bed is assumed negligible.

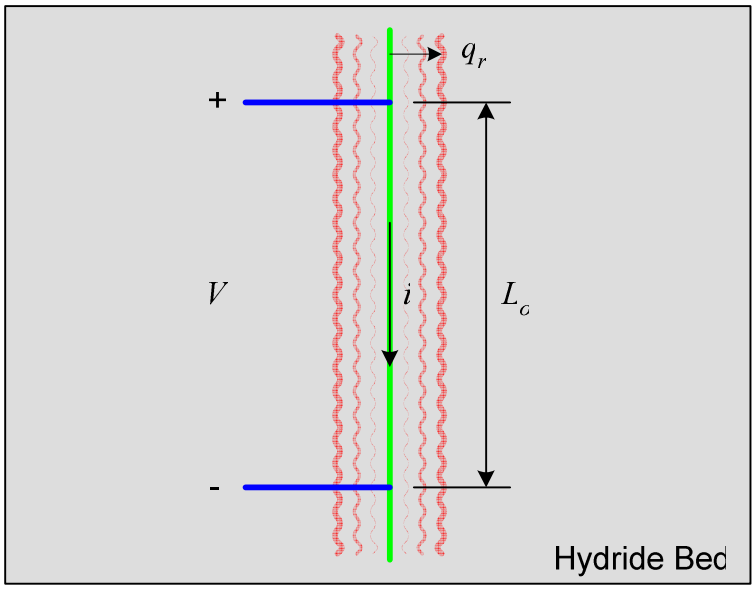

Figure 3-3 Test apparatus concept.

As explained in Chapter 2, the selection of platinum for the wire material is advantageous because the wire can serve a dual purpose. In addition to producing a constant heat flux, the platinum wire is a resistance-based temperature measuring device, allowing the temperature response of the wire to be measured. Because the resistance is a property of the wire segment between the voltage leads, the temperature measurement is averaged over this length of wire. This averaging reduces the effects of variations in porosity and grain size along the wire length. A measurement device such as a thermocouple would be more

susceptible to these local variations and thus could invalidate the assumption of a homogenous bed.

Because temperature will be measured via the resistance change in the platinum wire, it is convenient to rearrange the formulation of Equation 3.9 to one that contains R. The temperature and resistance of platinum are related by:

$$R(T) = R_0(1 + \alpha(T - 273)). \tag{3.10}$$

where α is a known constant for platinum ($\alpha = 0.003925\ \mathrm{K}^{-1}$), and R_0 is given by:

$$R_0 = R(273K), \tag{3.11}$$

which can be measured directly in an ice bath. Taking the derivative of Equation 3.10 with respect to T, and substituting into Equation 3.9:

$$k = \frac{\alpha Q' R_0}{4\pi}\left(\frac{dR}{d\ln(t)}\right)^{-1} = \frac{\alpha Q R_0}{4\pi L_0}\left(\frac{dR}{d\ln(t)}\right)^{-1}. \tag{3.12}$$

where Q is the total energy input to the wire and L_0 is the length of the test section of the bed.

In order to measure resistance accurately, it is advantageous to use a "four-point" measurement technique. In this method, a voltage measurement is made between two points on the current-carrying wire separated by a distance L_0 (see Figure 3-3). Assuming the voltage measurement device has very high impedance, no current will flow through the voltage leads and a high-accuracy measurement can be made without concern for the length of the leads. Resistance is then calculated using Ohm's law.

The derivative of R with respect to $\ln(t)$ can be approximated by the slope from a first order regression fit of experimental R vs. $\ln(t)$ data. Experimental results confirm that this relationship is linear [14]. The method for calculating a slope based on a least squares fit is:

$$m = \frac{N\left(\sum x_i y_i\right) - \left(\sum x_i\right)\left(\sum y_i\right)}{N\left(\sum x_i^2\right) - \left(\sum x_i\right)^2}, \tag{3.13}$$

where N is the number of (x_i, y_i) point pairs. In this case, the points are (τ_i, R_i) pairs, where $\tau_i = \ln(t)$. Thus the calculation for k becomes:

$$k = \frac{\alpha}{4\pi}\frac{QR_0}{L_0}\frac{1}{m}, \tag{3.14}$$

where $$m = \frac{dR}{d(\ln(t))} = \frac{N\left(\sum \tau_i R_i\right) - \left(\sum \tau_i\right)\left(\sum R_i\right)}{N\left(\sum \tau_i^2\right) - \left(\sum \tau_i\right)^2}. \tag{3.15}$$

3.1.3 Estimation of Uncertainty

When calculating a quantity from experimental measurements, the uncertainty of each of the measured values propagates as error in the final calculated quantity. In the design of the apparatus the uncertainty calculation is used in conjunction with a finite element analysis of the apparatus to identify the design parameters that minimize uncertainty. In the experimental investigation, the same uncertainty relationships will be used to determine experimental uncertainty.

The propagation of uncertainty in the calculation of a parameter x is given by:

$$\sigma_x^2 = \sum\left(\frac{\partial x}{\partial \theta}\sigma_\theta^2\right) \text{[38]}, \tag{3.16}$$

where θ is each of the measured variables in the equation and σ_θ is the uncertainty of each measurement. Using Equation 3.16, the uncertainty in k is:

$$\sigma_k^2 = \left(\frac{\alpha}{4\pi}\right)^2\left[\left(\frac{R_0}{L_0}\frac{1}{m}\cdot\sigma_Q\right)^2 + \left(\frac{Q}{L_0}\frac{1}{m}\cdot\sigma_{R_0}\right)^2 + \left(-\frac{R_0 Q}{L_0^2}\frac{1}{m}\cdot\sigma_{L_0}\right)^2 + \left(-\frac{R_0 Q}{L_0}\frac{1}{m^2}\cdot\sigma_m\right)^2\right]. \tag{3.17}$$

where the constants α, and π are known. In the finite element uncertainty analysis, the effects on uncertainty of the undisturbed length, L_o, nominal resistance, R_o, and power, Q, are based on uncertainties from their respective measurement devices. In the experimental investigation, these quantities will be measured directly.

The calculation of the slope, m, is based on a differential measurement of resistance (Equations 3.12 and 3.15), so it is assumed that any measurement bias (or systematic error) is eliminated when considering uncertainty. Thus, measurement precision is of primary concern in calculation of the uncertainty in the slope. Data for the experimental precision of the resistance measurement device were not separately identified in the manufacturer's specifications. For the purpose of apparatus design, the uncertainty in the slope is taken to be less than ± 0.5 %. Experimental results (see Section 5.1.2) confirm this assumption.

The change in resistance caused by the temperature increase in the wire introduces additional uncertainty in the power input to the wire. Using Ohm's law and Equation 3.10,

$$\Delta Q = I^2 R_0 \alpha \Delta T \,. \qquad 3.18$$

The maximum temperature change during testing directly affects the variation, and thus the uncertainty, in the power supplied to the wire. The uncertainty in Q will therefore be a combination of instrument uncertainty and uncertainty induced by variation in temperature. It is clear from Equation 3.18 that it is advantageous to have a temperature change that is as small as possible.

3.2 Finite Element Model

Figure 3-3 illustrates the effective thermal conductivity measurement device without any geometric constraints. Ideally, the hydride bed surrounding the wire would be extremely large in order to approximate an infinite medium, but this is clearly impractical. A cylinder is the most efficient means of approximating an infinite medium when the heat source is linear, and this shape is chosen for the test apparatus. Ascertaining the effects of cylinder length (L) and diameter (D) on uncertainty over a range of k values is the primary goal of the finite element (FE) model.

Quantification of end effects will be used to optimize apparatus geometric parameters L and D. The cylinder ends create a pathway for heat to travel in a non-radial direction, and create regions at either end of the wire where temperature gradients exist. The extent of these end regions dictates where the voltage measurement leads should be placed. It is also

necessary to define a time, t_{bnd} that represents the point when the heat flux produced by the wire reaches the outer boundary of the test bed. The time at which the infinite bed assumption is no longer valid is then approximately $2t_{bnd}$, as the influence of the boundary has to propagate back to the wire. The FE model will also be used to estimate the amount of current necessary to produce a desired temperature rise in the wire and also to determine approximate test times.

3.2.1 Definition and Assumptions

Figure 3-4 shows the definition of the FE model including PDE's, boundary and initial conditions and physical constants. To simplify the solver routine, the physical properties listed in Figure 3-4 were assumed to be constant for all temperatures and hydride phases, although the heat capacity is known to change somewhat with phase for the Na-Al-H system [12]. By assuming angular symmetry, the FE model can be simplified to a transient two-dimensional problem. The domain is rectangular, which represents the cylinder in the *r*- and *z*-dimensions. The left edge of the domain represents the bed/wire interface, while the right edge of the domain represents the bed/outer wall interface. Although the model mesh is rectangular, the partial differential equations (PDE's) are in cylindrical form to account for the variation of physical parameters in the r-direction. Boundary 1 (left) is set to produce a constant heat flux per surface area of wire, q_0, modeling the behavior of the platinum heater wire. Boundaries 2, 3, and 4 are held at a constant temperature, T_0, modeling the un-insulated boundaries of the test fixture. The initial condition of the model is uniform temperature, T_0, throughout at $t = 0$.

Governing Equation
$\frac{1}{\kappa}\frac{\partial T}{\partial t} = \frac{\partial^2 T}{\partial z^2} + \frac{1}{r}\frac{\partial}{\partial r}\left(r\frac{\partial T}{\partial r}\right)$

Physical Constants
$\rho = 1.24$ g/cm^3 [1]
C = 1583 kJ/kgK [2]
$r_{wire} = 0.25$ mm

Boundary & Initial Conditions	
1	$\frac{\partial T}{\partial r} = \frac{q_0}{k}, r = r_{wire}$
2	$T = T_0, r = r_{wall} = D/2$
3	$T = T_0, z = 0$
4	$T = T_0, z = L$
	$T(r,z) = T_0, t = 0$

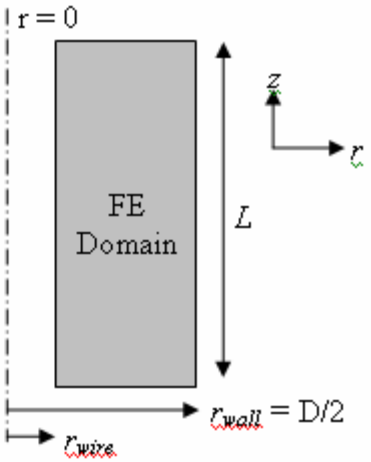

Figure 3-4 Definition of the finite element model.

3.2.2 Numerical Solution and Calculation

A custom computer program was written and applied in conjunction with commercially available finite element software to numerically solve the problem. The full code for the solver routine (written in MATLAB m-file script) is presented in Appendix A. The model was solved over a range of values for *k* and *L/D* ratio, which are listed in Table 3-1 along with the parameters *L* and r_{wire}. Cylinder length, *L*, was held constant at 10 cm because it was found from preliminary results that the *L/D* ratio was the controlling factor in the model outcomes. The minimum value for the *L/D* ratio is taken to be 3 from the summary of available literature presented in Table 2-1, and the maximum is based on practical sizing constraints. The reasonable maximum and minimum values of *k* were also estimated from the data presented in Table 2-1. The radius of the platinum wire, r_{wire}, was selected as the largest from the range shown in Figure 3-2 for robustness against the large-scale volume changes inherent to the Na-Al-H system during phase changes [12]. The only

[1] Personal communication with Dr. Darlene Slattery of FSEC.
[2] [12]

other variable to be specified in the model was the boundary heat input per unit area, q_0. There is no direct method of determining q_0, so for each combination of variables, an iterative process was undertaken to determine the value that resulted in a temperature rise at the center of the wire of 3 ± 0.01 K at time $2t_{bnd}$.

Table 3-1 FE model parameters.

Parameter	Value
k – min	0.01 W/mK
k – max	3 W/mK
L/D – min	3
L/D – max	7
d_{wire}	0.5 mm
L	10 cm

The time step was 0.1 seconds for k values above 0.1 W/mK. At k values below this, computing times were prohibitively long and a time step of 1 second was used. Although the model is simplified as much as possible, the nature of the iterative process of determining q_0 necessitated solving the model several times for each case, resulting in significantly more processing operations.

Once each model was solved, a set of raw temperature data over the geometric domain and at all time steps up to $2t_{bnd}$ was obtained. Characterization of end effects was accomplished by using the resultant raw data to calculate an "undisturbed length," L_0, at time $2t_{bnd}$ at the wire boundary. The undisturbed length is defined as the length of the central portion of the wire that varies by less than 5 % from an average value taken at the midpoint. Figure 3-5 shows a typical temperature profile at the wire, where z is the length along the wire. In this example, the quantity L_0 is the length of the central linear portion between about 0.02 and 0.08 m. Quantifying L_0 is essential to the development of a test apparatus that

accurately approximates an infinite cylinder, as the distance between the voltage leads should be no more than its value.

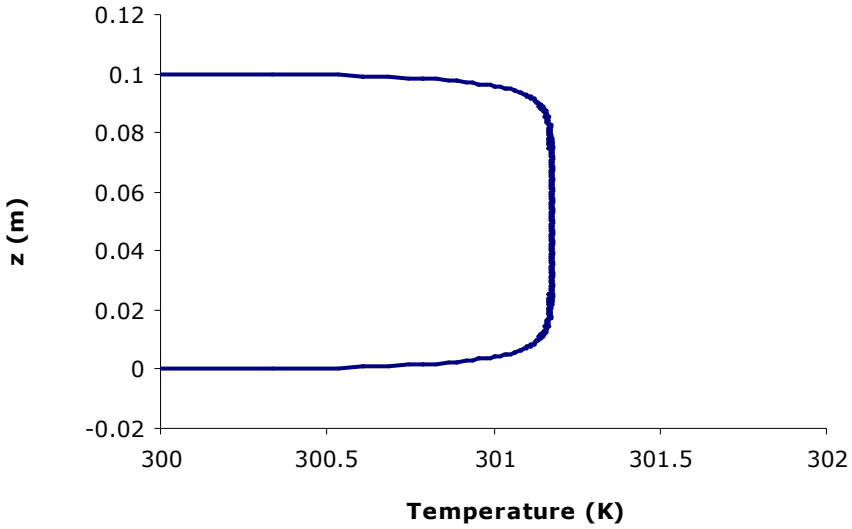

Figure 3-5 Typical temperature profile at the wire-hydride interface.

The second phase of the FE simulation was to use the transient temperature response from each of the FE runs to simulate the calculation of k and the uncertainty. The transient temperature response at the surface of the midpoint of the wire (r_{wire}, $L/2$) was used for this analysis. The raw temperature data was converted to resistance data using Equation 3.10.

An example of the FE transient results is shown in Figure 3-6 and full results are provided in Appendix B. The slope, m, was calculated as it would be from experimental results using resistance and the natural log of time. The green lines represent t_{start} and t_{stop}, the portion of the data considered linear for this calculation. Several routines were considered for determining these extents based on pre-determined criteria, but they were complex and results were unsatisfactory. Instead, the linear portion was selected by inspection, using the correlation coefficient from the linear fit as a guide.

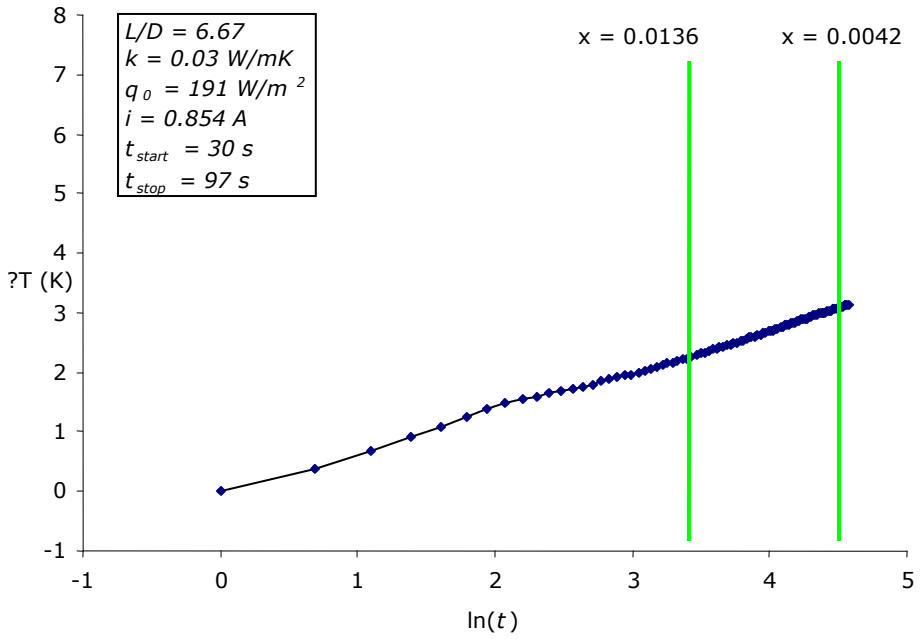

Figure 3-6 Example of transient finite element results.

The uncertainty was computed using Equation 3.17, where L_0 is the cylinder length and R_0 is based on L_0 and the resistivity of platinum. The uncertainty in the slope is assumed constant at ± 0.5 %. A constant power, Q, was assumed and calculated from the value of q_0 determined during the simulation as

$$Q = q_0 SA_{wire} = q_0 L \pi D_{wire} . \qquad 3.19$$

From Q and the resistance data, an estimate of current was calculated. In an actual test, the power will not be constant, as explained above. Equation 3.18 was used to calculate the change in power to be used in the uncertainty calculation that would be expected in an experiment based on the temperature rise.

3.3 Results

The finite element results were first validated by comparing the values of k that were input to the model to the values of k calculated from the results. The data were then

examined to determine the relationship of the input parameters to the undisturbed length, the uncertainty, and the contributions to uncertainty of the measurements of m, L_0, R_0 and Q. Finally, the data were used to predict experimental test times and current requirements.

3.3.1 Validation

To asses the validity of the FE model, the values of k calculated from the FE results were compared to the input values of k used in the model. The percent difference is plotted versus the input k value in Figure 3-7. Except for the input k value of 3 W/mK, the values of k predicted from the FE data are within ± 4% of input k values for L/D ratios from 4.0 to 6.67. Within this range, the FE results suggest that the assumptions inherent in the transient hot-wire technique are satisfied. The increase in the percent difference at the input k value of 3 W/mK is likely due to the extremely short $2t_{bnd}$ times associated at this conductivity, which range from 4.9 to 1.3 seconds for L/D ratios of 3.33 to 6.67, respectively. Because the primary existing study on the thermal conductivity of the Na-Al-H system did not record values for k above 1 W/mK, the apparatus will only be designed to accommodate thermal conductivities at this value and below [12].

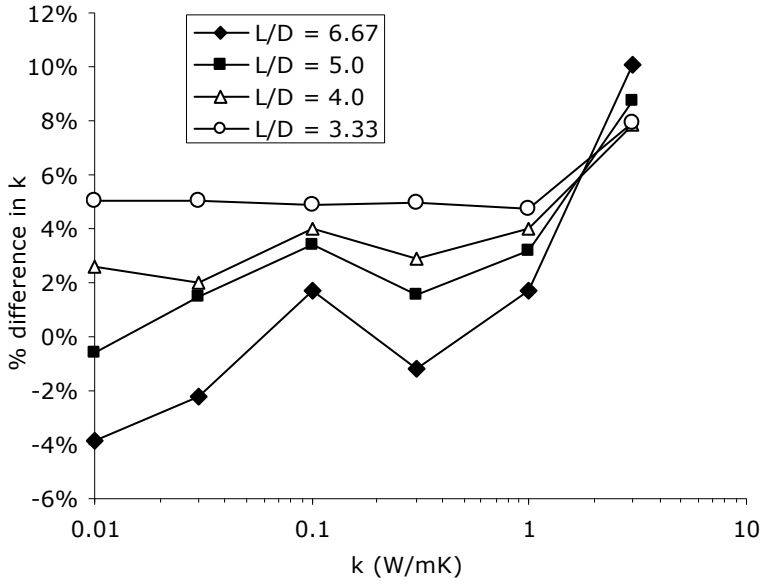

Figure 3-7 Percent difference between FE model input values and calculated values of *k*.

3.3.2 Quantification of Undisturbed Length

It is desirable to maximize the undisturbed length in order to maximize the region of testable material within the cylinder and thus minimize the "wasted" material at the ends. Additionally, a longer undisturbed length provides more material across which variations in grain size and particle distribution can be averaged. Figure 3-8 shows the relationship of the undisturbed length (plotted as L_0/L) to the effective thermal conductivity for several L/D ratios. It is clear that the size of the undisturbed length is primarily a function of the L/D ratio. The undisturbed length is also somewhat dependant on the effective thermal conductivity of the bed, but this relationship is not clear. Higher thermal conductivity generally results in a longer undisturbed length, as do those geometries that are longer and thinner (higher L/D ratios). However, at the three smallest L/D ratios, the undisturbed length decreases at higher values of effective thermal conductivity. It is not clear what is responsible for this result. The transient finite element results show that undisturbed length decreases with time as end effects propagate inward, so these values should be considered best case. The actual test apparatus geometry will be built with a conservative safety factor to account for this.

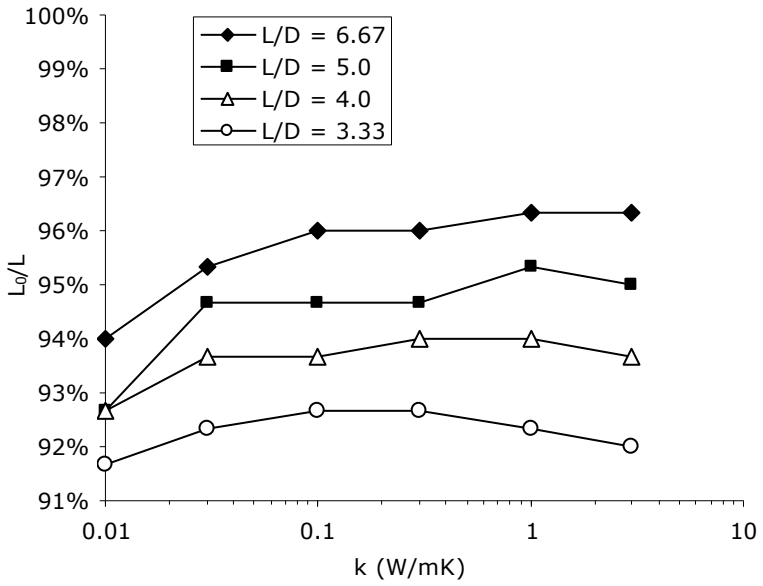

Figure 3-8 Effect of k on the undisturbed length, L_0, calculated from FE results.

3.3.3 Quantification of Uncertainty

It is desirable to minimize the measurement uncertainty in *k* as much as possible. Figure 3-9 shows the relationship between the input *k* values and the uncertainty in the calculated values of *k*. In general, the uncertainty is very good and is below 3% for all values of *k*. Uncertainty is seen to decrease slightly with increasing *L/D* ratio, with *L/D* = 3.33 having the highest uncertainty and *L/D* = 6.67 having the lowest. Uncertainty also decreases with increasing *k*, reaching an asymptote above a thermal conductivity of 0.3 W/mK. These results suggest that maximizing the *L/D* ratio will minimize the uncertainty in the measurement of *k*. However, all *L/D* ratios examined produce good uncertainty results.

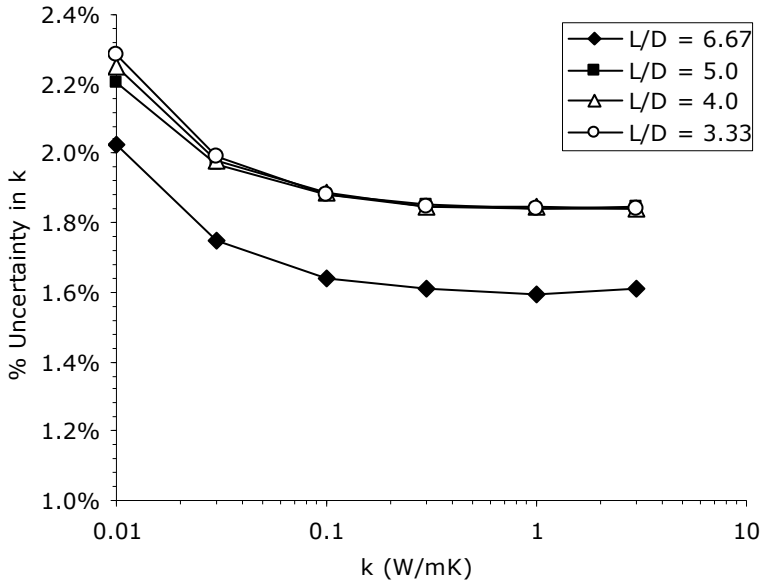

Figure 3-9 Total uncertainty in *k* calculated from the FE model.

Figure 3-10 illustrates the contributions of each of the terms in Equation 3.17 to the total uncertainty in the calculated value of *k* for *L/D* = 4.0. It was found that the contributions do not vary significantly with *L/D* ratio, but Figure 3-10 demonstrates that the contributions do vary with *k*. The contribution of uncertainty in the measurement of undisturbed length is insignificant for all values of *k*. For a thermal conductivity of 0.01, the largest contributor to total uncertainty is the measurement of power to the wire. For values of thermal conductivity above 0.01 W/mK, the major contributor to uncertainty is the

nominal resistance measurement. No improvements can be made to the accuracy of either of these measurements given the current test setup. A voltage measurement device with higher accuracy and precision would improve these, but the total measurement uncertainty is already sufficiently low for the current setup. The uncertainty in the slope contributes relatively equally at all values of *k*, which is expected given the assumption made in Section 3.1.3.

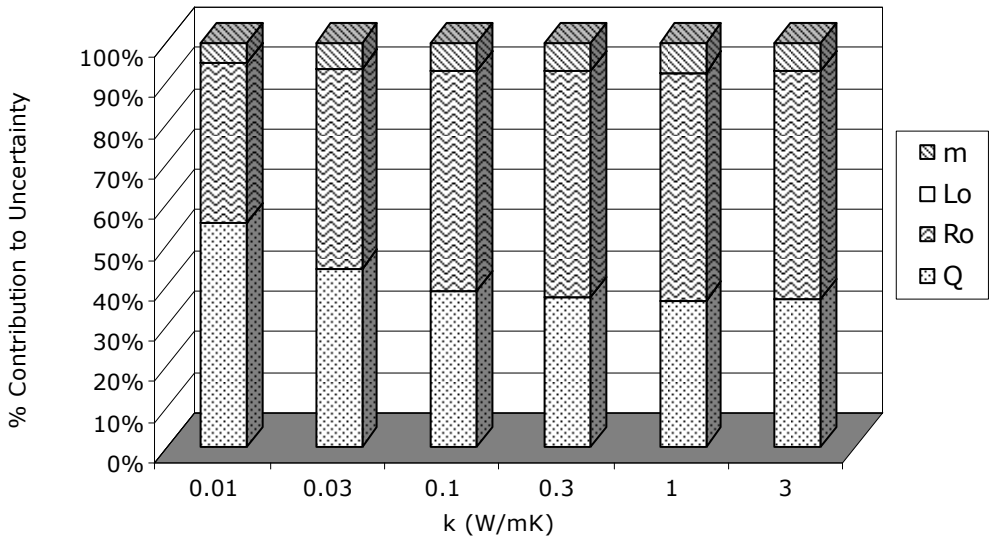

Figure 3-10 Percent contributions to uncertainty in the calculated value of *k* for *L/D* = 4.0

3.3.4 Prediction of Experimental Test Times and Currents

In addition to optimizing the apparatus geometry, the finite element results can be used to predict test times and current requirements. Figure 3-11 shows the test times for all *L/D* ratios and for all relevant values of *k*. Test time is a function of both *L/D* ratio and *k*, decreasing with both parameters. In terms of *L/D* ratio, heat has further to travel with smaller *L/D* ratios (larger diameters), thus taking longer to reach the cylinder wall. In terms of *k*, heat is conducted faster for higher *k* values, thus reaching the cylinder wall faster. It can be

seen that test times are very long for small values of k, up to 2000 seconds in the worst case. Tests for values of k between 0.1 and 1 W/mK should only require 10-200 seconds.

Figure 3-12 shows input current requirements for the same range of parameters. The equipment used in the experimental investigation has a limit of 4000 mA output current, also shown in Figure 3-12. The finite element results show that at k = 1 W/mK, the current requirements do slightly exceed the limit of the equipment. The experimental data may show actual tests require more or less current, but the finite element estimates suggest the equipment will be able to meet or fall just short of meeting the predicted requirements. Operating at a slightly lower current will only have the effect of reducing the temperature rise slightly. This information on test times and current requirements will be used when making initial experimental runs.

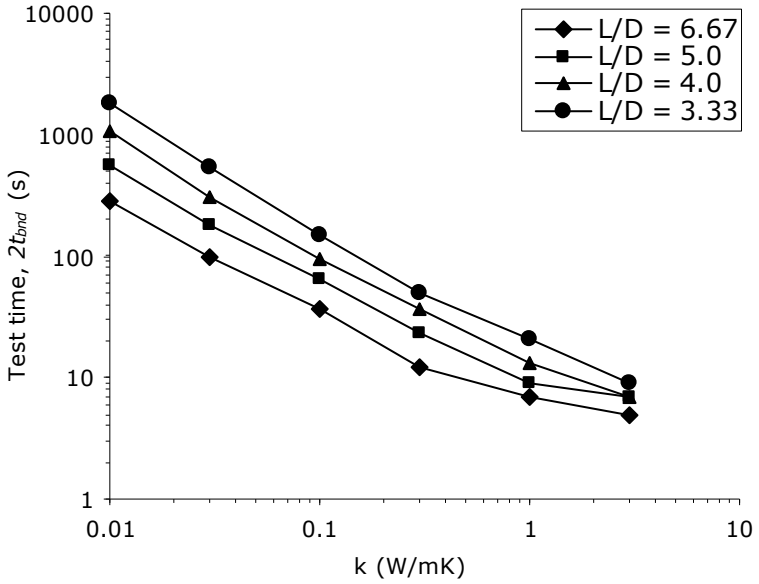

Figure 3-11 Test times predicted by finite element results.

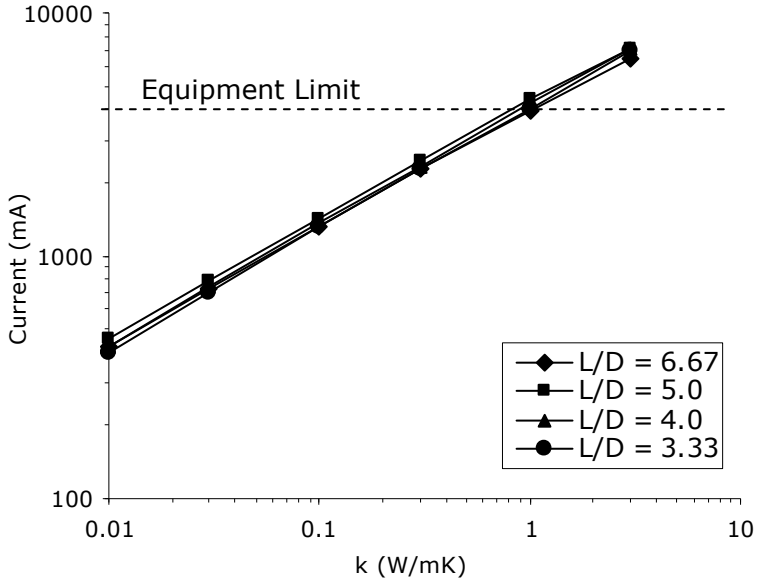

Figure 3-12 Current requirements predicted by finite element results.

3.4 Summary

A finite element model was used to explore the effect of geometric parameters (*L/D* ratio) on a sample cylinder measurement apparatus. The effect of the geometric parameters on undisturbed length, measurement uncertainty, test time and current requirements were considered. Validation of the finite element results showed the calculated values for *k* were within ± 4% of actual model input values for $k \leq 1$ W/mK. The undisturbed length was high for all geometries, but slightly better for large *L/D* ratios (i.e., geometries that are longer and thinner). Uncertainty was estimated at better than 3% for all geometric conditions and values of *k* and was slightly improved for large values of *L/D*. Over the range of *k* expected for the Na-Al-H system, test times were predicted to be between 10 and 200 seconds. Current requirements are predicted to be between 1500 and 4000 mA.

Based on these results, sample cylinder geometries having a length-to-diameter (*L/D*) ratio between 3.33 and 6.67 are predicted to produce satisfactory levels of uncertainty and to have acceptable test times and current requirements. Because all designs within the constraints specified in Table 3-1 were shown to be acceptable, the apparatus design can focus more on other criteria such as ease of sample loading and availability of materials. However, an appropriate sample cylinder should still have an *L/D* ratio that falls in the range

of 3.3 to 6.67, and the spacing between the voltage leads should not exceed 91% of the total cylinder length. Following these criteria, the experimental apparatus should produce data with acceptable levels of uncertainty. Furthermore, test times and current requirements are estimated in advance, aiding in the experimental procedure.

The following chapter will describe the construction of the experimental apparatus based on these results. Chapter 5 will discuss the experimental investigation using the apparatus and Chapter 6 presents experimental results.

4 EXPERIMENTAL APPARATUS

The experimental apparatus was constructed based on the results presented in Chapter 3. This chapter addresses the construction of the sample cylinder, the support equipment and data acquisition.

4.1 Sample Cylinder

The heart of the apparatus is the sample cylinder that holds the metal hydride. This cylinder also serves as a structural support for the platinum wire and voltage measurement leads. Other desirable characteristics considered in the design are ease of sample loading, transparency, chemical and temperature stability, and permeability to gas flow. The materials used must be able to withstand a temperature up to 150 °C. The sample cylinder is contained in a pressure vessel that is designed to withstand a pressure of at least 1500 psi (100 bar).

4.1.1 Components

Figure 4-1 illustrates the main components of the sample cylinder. Specifications of the cylinder are shown in Table 4-1. The sample cylinder consists of a tube and end caps with centrally-located and offset holes for the platinum heater wire and voltage leads, respectively. The bottom cap is a full plug and fits snugly in the bottom of the tube while the top cap is reduced in width to act only as a support spar and not as a full plug. Figure 4-1 (b) shows how the three main pieces fit together, the platinum wire and voltage leads, and the locations of two thermocouples that are imbedded in the sides of the cylinder. The platinum wire is secured and kept taught by set-screw collets at either end of the cylinder. The end caps provide structure to maintain tension on the wire. The voltage leads are angled towards the ends and exit the cylinder parallel to the main wire in order to minimize their effect on the homogeneity of the bed. Because the heat transfer is predominately in the radial direction, a scheme in which the leads exited perpendicular to the current-carrying wire would create a small, but significant path for heat to travel outwards, in effect bypassing the desired route through the material. The thermocouples are situated such that they are flush with the inside wall of the cylinder.

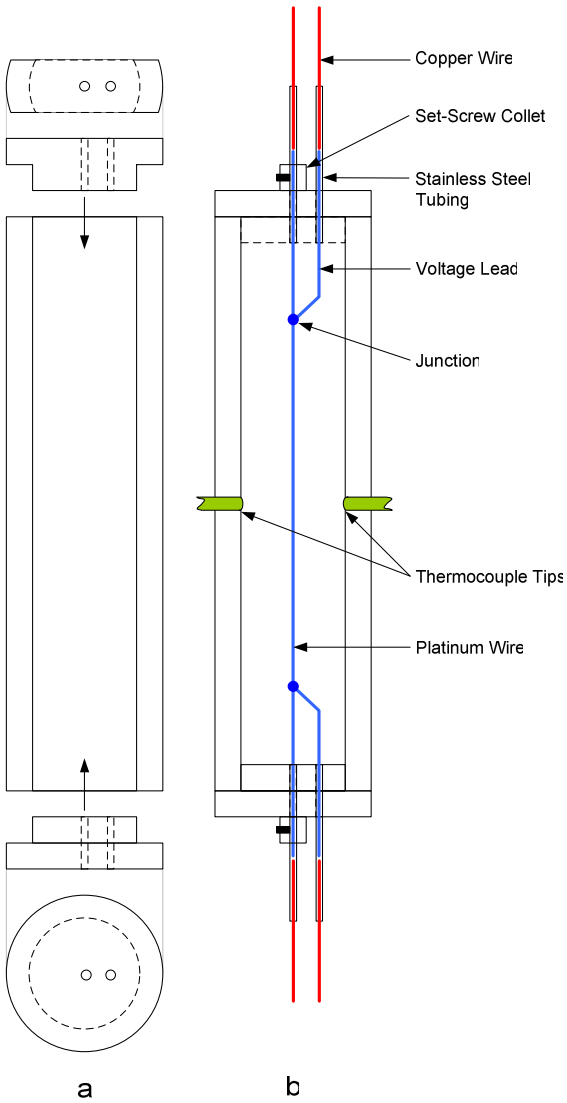

Figure 4-1 Components of the sample cylinder.

The openings at the top facilitate the filling of the cylinder and also allow for the ingress and egress of gas. However, they also dictate that the cylinder not be inverted, as this would result in spillage of material. Given the dimensions of the reactor vessel, a diameter was chosen such that material can be easily poured into the top. This resulted in an *L/D* ratio somewhat lower than the optimal value, but still within the acceptable range established by the finite element results. The platinum wire is kept in the central axis of the cylinder by then end caps, which is a criteria necessitated by the assumptions of the analysis of the previous chapter. In the final fabrication of the bottom end cap, the thickness was increased

and a grove added to the bottom to accommodate the set-screw collet and wires. This allows the cylinder to stand upright on a flat surface which aids in test setup and keeps the cylinder vertical in the pressure vessel.

Table 4-1 Sample cylinder specifications.

Parameter	Value
Total height	11.11 cm (4.37 in)
Total interior height	10.48 cm (4.126 in)
Usable interior height	10.30 cm (4.06 in)
Interior diameter	2.06 cm (0.812 in)
L/D Ratio	5
Voltage lead separation (L_0)	7.35 cm (2.89 in)
L_0/L	0.71
Usable volume	34.3 cm^3

4.1.2 Materials

A primary criterion for the sample cylinder is transparency because of the need to measure the material depth (to calculate porosity) and more importantly the desire to view the material for qualitative examination. For temperature stability, glass is the only material that provides transparency, as all plastics that can operate at 150 °C are opaque. Hollow cylindrical stock (0.812 in ID) glass was selected for the main tube and solid cylindrical stock (1.0 in OD) PEEK plastic was selected for the end caps. All pieces were cut or machined to specifications, cleaned of tool marks, and polished. The thermal capacity of the glass also serves to maintain the constant-temperature boundary condition.

High purity (99.9999%) platinum of 0.508 mm (0.020 in) diameter was used for the heater wire and voltage leads. For data acquisition, the wires exiting the sample cylinder must be extended some distance to instrumentation, but due to the high cost of platinum another material must be used for this purpose. Solid copper wire (20 awg) was selected to extend the wires, and this choice will be explained below. To join the platinum and copper

wire, short lengths of stainless steel hypodermic tubing were cut and used to splice the two materials together. Due to the low temperature rise during testing, thermal expansion of the platinum wire is negligible.

4.1.3 Assembly

The platinum wire and voltage lead subassembly was built first using acid-free solder. The areas to be joined were cleaned, coated with flux and a small bead of solder was applied. This created a strong but compact joint. Following this, sections of stainless steel tubing were cut, the interior surface cleaned with a rough wire and coated with flux. The four platinum wire ends were cleaned, fluxed and dry fitted into one end of each section of stainless steel tubing. Heat was applied to the outside of the joint and solder was fed in. This procedure was repeated with the copper wire at the other end of the stainless steel tubing.

The copper extension wire has insulation that makes its overall diameter greater than the inner diameter of the collets and the holes in the end caps. For this reason, the insulation was cut along its length on the four extension wires so that it can be slipped off, allowing the collets and end caps to be installed. This also allows the collets and end caps to be easily removed for disassembly. The insulation can be replaced after assembly to prevent shorting of the wires.

After completion of all solder joints and removal of wire insulation, the cylinder, end caps, wire and collets were fitted together as shown in Figure 4-1 (b). The bottom collet was tightened over the stainless steel tubing to prevent damage to the platinum wire. Tension was applied to the central wire and the top collet was then tightened. The copper extension wire insulation was replaced and the bottom two wires were bent to lay in the groove cut into the bottom plug. The wires were then extended vertically to run parallel to the top two wires. These wires were trimmed and a four-contact connector installed. Additionally, two holes were drilled in the vertical center of the cylinder 180 degrees apart for the two thermocouple tips. These thermocouples will be used to determine when steady-state temperature is reached within the sample. A photograph of the completed sample cylinder is shown in Figure 4-2.

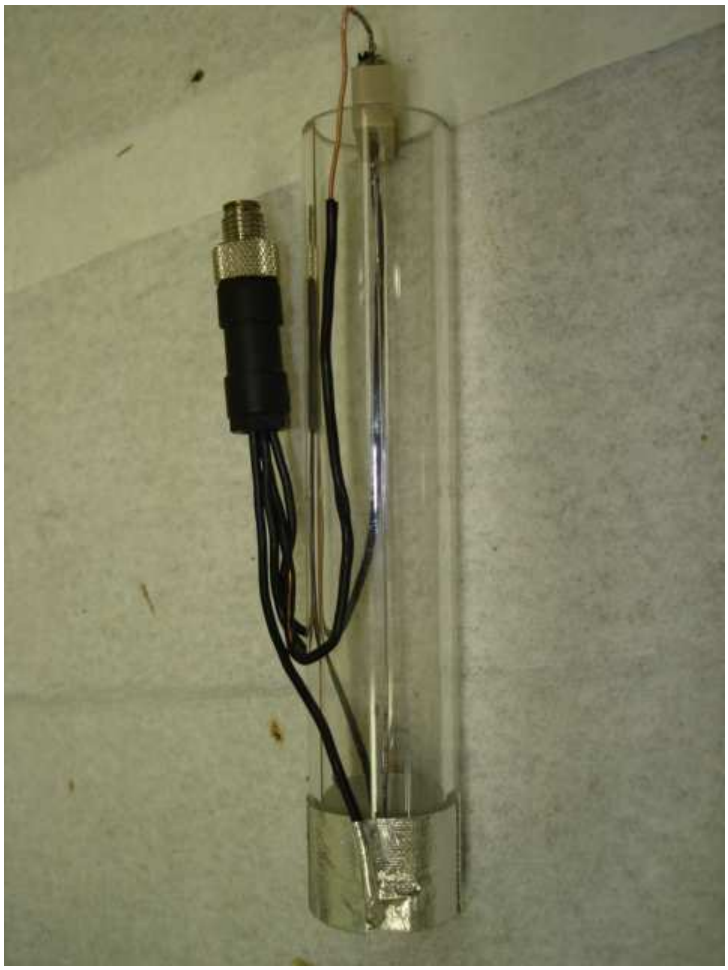

Figure 4-2 Photograph of the completed sample cylinder.

4.2 Environmental Control

The sample cylinder constitutes the measurement apparatus, but environmental control is also required. Pressure and temperature conditions were controlled in a reactor vessel that held the sample cylinder. Based on the maximum outside dimensions of the sample cylinder and the environmental requirements, a pressure vessel was selected from Parr Instruments. The vessel head includes a rupture disc, wire gland and gas port. Figure 4-3 shows a schematic representation of the experimental setup.

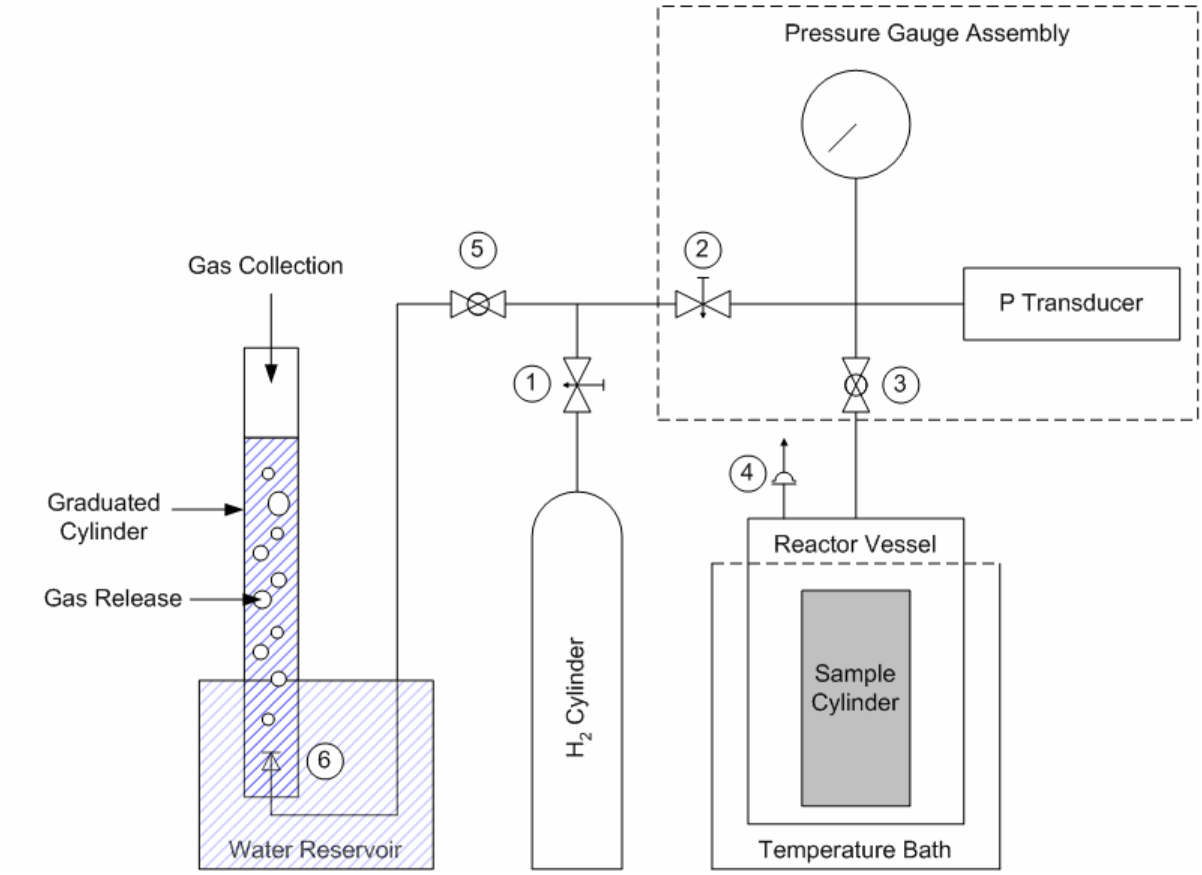

Figure 4-3 Schematic of environmental control and gas measurement equipment.

4.2.1 Pressure Control

The Parr model 4766 is a 450 mL stainless steel reactor vessel capable of handling pressures up to 3000 psi (207 bar). Pressure conditions in the reactor are controlled by regulating the amount of gas in the vessel and insuring the connections and seals are as leak-free as possible. Prior to testing the setup was pressure tested and leak detector used on all joints.

Referring to Figure 4-3, the gas is supplied by a compressed cylinder with a regulator (1) capable of output from 100 to 2000 psi (7 to 138 bar). Additionally, a needle valve (2) regulates the flow of gas into or out of the reactor. The pressure gauge assembly consists of a pressure transducer and an analog gauge. Upon closing the valve immediately above the vessel, (3), the pressure gauge assembly can be removed to fit the vessel in a glove box for sample loading. The rupture disc (4) is designed to burst at the maximum safe working

pressure of the vessel, 3000 psi (207 bar). A plug valve (5) isolates the gas measurement system, which will be described below.

All piping and tubing used in the pressure system is rated at or above 3000 psi (207 bar). Stainless steel tubing is used between the hydrogen cylinder and the pressure gauge assembly and uses swaged fittings. Tapered thread pipe fittings are used in the pressure gauge assembly and between valve (3) and the reactor. These are also stainless steel and use Teflon tape to inhibit leaks and prolong thread life.

4.2.2 Temperature Control

Control of temperature inside the reactor vessel is accomplished by a constant-temperature oil bath. The bath is capable of maintaining temperatures from 20 to 230 °C. A stirred hot plate is used to heat the oil in a container in which the pressure vessel is immersed. Control is accomplished through a custom PID controller that monitors the temperature in the oil bath. Temperature stability of ± 0.5 °C is attainable in the bath, which is damped by the large mass of the vessel.

4.3 Data Acquisition

Data is acquired from three sources: voltage and current data from the platinum hot wire, temperature data from the sample cylinder and interior of the reactor vessel, and volumetric data from a gas measurement system used to quantify the amount of hydrogen evolved during pressure-composition isotherm measurements.

4.3.1 Voltage, Current, Temperature and Pressure

As explained in Section 3.1, the thermal conductivity measurement procedure consists of supplying current to the platinum wire at a constant rate while measuring the response across the voltage leads. Resistance values are then computed by applying Ohm's law. Supply of current and measurement of voltage are accomplished with a Solartron 1480 Multistat. This is a multi-channel potentiostat that communicates directly with the data acquisition PC through a general purpose interface bus (GPIB) card.

A USB thermocouple card is used for temperature acquisition. One thermocouple is located in the ambient space inside the reactor vessel and two others are located 180 degrees apart on the wall of the sample cylinder. These three thermocouples are used to verify steady-state temperature inside the vessel and the sample and to determine the time at which the temperature disturbance reaches the outer boundary of the sample cylinder. A program was written in the LabVIEW language to acquire, display and save all thermocouple data during testing. The program synchronizes with the 1480 software when the test current is first started.

Figure 4-4 illustrates the wiring inside the sample cylinder. There are four solid copper wires that are necessary for the current and voltage measurements and two sets of iron/constantan wire pairs for the two sample cylinder thermocouples, labeled "TC_A" and "TC_B." The third thermocouple has its own connector in the vessel head and is labeled "TC_C." For convenience during test setup, connectors for the voltage/current measurement and two thermocouples are located inside the reactor. These connectors allow the sample cylinder to be detached and removed from the pressure vessel for filling and other tasks. The gland supplied with the reactor vessel will seal eight 20 awg solid wires up to 3000 psi at 100 C. The stainless hypodermic tubing, current/voltage connector and thermocouple connectors were all selected to accommodate this wire size. All connectors and other parts inside the reactor can withstand temperatures of 150 C and pressures over 3000 psi (207 bar).

The 1480 is equipped with banana plug-style connectors which are rated for the maximum current and voltage limits of the device. The wires exiting the sample cylinder gland extend uninterrupted to these connectors in order to minimize the number of wire connections in the system. Similarly, the thermocouple wires extend from the gland directly to the thermocouple card.

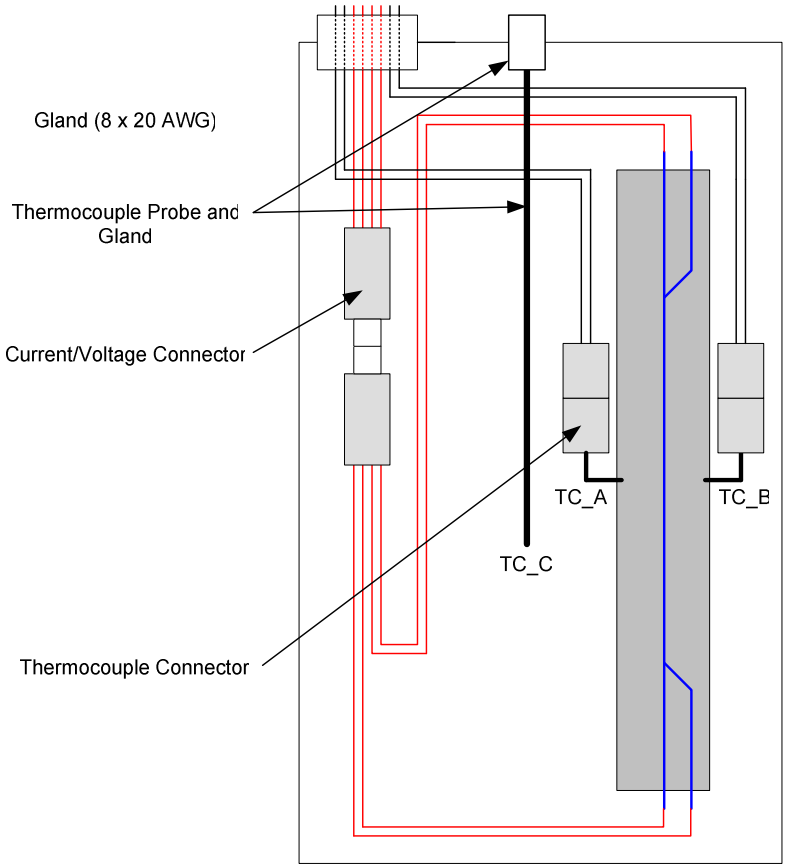

Figure 4-4 Schematic of wiring inside reactor vessel.

The pressure inside the vessel is recorded by a pressure transducer, illustrated in Figure 4-3. The transducer is capable of reading gauge pressures up to 2000 psi (138 bar), can withstand pressures up to 4000 psi (276 bar) and has an accuracy of ± 5 psi (0.3 bar). The transducer requires an excitation voltage, which is supplied by a DC power supply set at 8 volts, and outputs a signal scaled to 80 mV. The output signal of the transducer is read by the fourth channel on the thermocouple reader and scaled to read psi in the computer software.

4.3.2 Gas Evolution

During composition measurements, hydrogen gas that has evolved from the metal hydride sample will be released from the reactor vessel and measured. A gas volume measurement system is used to measure the amount of evolved hydrogen. This technique is a

batch process, in that a certain volume of gas is periodically discharged in a controlled manner through a needle valve in the system and then its volume is measured.

The schematic of the environmental control equipment in Figure 4-3 also illustrates the gas volume measurement system. The system itself is a 1 liter graduated cylinder inverted in a water reservoir which is open to the atmosphere. Prior to measurement, the cylinder is filled completely with water by submerging it; it is then inverted, keeping the mouth under water, while the top end is clamped in place. During testing, a plug valve (5) prevents gas from escaping. With the regulator (1) closed and the plug valve (5) open, the needle valve (2) controls the amount of gas released from the pressure vessel. The tubing terminates inside the graduated cylinder under water, so that escaping gas must rise into the vertical space, displacing the water downward. A check valve (6) rated at 1/3 psi (0.023 bar) prevents back flow of gas and water into the system. Graduations on the cylinder allow for measurement of the volume of the trapped gas at the completion of the release. After sufficient time for the gas to cool to room temperature, the mass of the released gas is then calculated using an equation of state for hydrogen. The temperature and pressure of the gas in the cylinder are assumed to be equivalent to ambient conditions, with the pressure corrected for the height of the remaining water column.

The graduated cylinder is sized such that full decomposition of the sodium alanate sample will yield about 10 volume measurements. This is based on a 16 gram sample with a reversible capacity of 4.68 wt%. The volume data are easily converted to mass, but must be corrected for the reduction in hydrogen gas storage within the pressure vessel as the pressure decreases along the pressure-composition isotherm. This is accomplished by measuring the dead volume in the system prior to testing and using an equation of state for hydrogen to calculate the change in mass.

4.4 Summary

A test apparatus was constructed based on results from a finite element investigation. It is designed to measure effective thermal conductivities from 0.01 to 1 W/mK. The apparatus uses the transient hot wire technique to minimize the test time and temperature differential of the metal hydride thus minimizing gas evolution during conductivity

measurements. Materials were selected to ensure the sample cylinder will withstand temperatures up to 150 °C and pressures up to 1500 psi (100 bar). Environmental control equipment provides control of pressure and temperature. Data acquisition hardware and software provide the ability to record experimental data. The following chapter describes the experimental approach, including the metal hydride test material, test apparatus validation and test procedures, while Chapter 6 describes the results of the investigation.

5 EXPERIMENTAL PROCEDURES

This chapter describes the experimental procedures. First, an explanation of the test apparatus validation is presented. Then, the synthesis and activation of the metal hydride material is described. Finally, the pressure, composition and temperature measurements are described.

5.1 Validation of Test Apparatus

The test apparatus must be validated to ensure its accuracy. First, the sensors and instruments used to collect data are calibrated to known standards. An overview of the measurement procedure and calculation of k and experimental uncertainty is provided. Then the procedures used to measure the thermal conductivity of a reference sample of known thermal conductivity are described. Lastly, a repeatability analysis that provides a statistical estimate of the repeatability of the measurement is described.

5.1.1 Instrument Calibration

The thermocouples used to acquire temperature data within the test apparatus were checked for accuracy in an ice bath. The temperature in the bath was confirmed by a secondary thermocouple measurement and a NIST-traceable mercury thermometer. No offsets larger than 0.1 °C were observed in the computer readings of the thermocouples. The pressure transducer arrived calibrated and has an accuracy of ± 0.25 % of full scale. Since the full scale range is 2000 psi (138 bar), the accuracy is ± 5 psi (0.34 bar). The graduated cylinder has an accuracy of 50 mL, or 4.4 mg of hydrogen.

Before installation in the sample cylinder, the nominal resistance of the platinum wire was measured in an ice bath with the temperature confirmed by a thermocouple and NIST-traceable mercury thermometer. Figure 5-1 shows the wire submerged in the ice bath with the readout on the thermocouple reader. The current and voltage leads of the platinum wire were connected to the multistat, a small current was passed through the wire and the voltage response was measured. The nominal resistance, R_0, was calculated using Ohm's law as 36.56 ± 0.064 mΩ at 0°C. The uncertainty in this measurement is based on the accuracy of

the multistat (± 0.1 % full scale). Data from the resistance calibration is presented in Appendix C.

Figure 5-1 Measurement of nominal platinum wire resistance.

5.1.2 Overview of Measurement Procedure and Calculation

Prior to any test, the test sample is allowed to come to steady-state temperature and pressure. As explained in Section 4.3.1, the multistat supplies the current and measures the voltage response during thermal conductivity tests. Based on Figure 3-11 and Figure 3-12, initial guesses for current and test time are made and entered into the test software. At the commencement of a test, the instrumentation applies current to the wire and measures the voltage response for the duration of the test. Once the test is complete, the data is saved and then reduced in a spreadsheet template. This template calculates k and the uncertainty based on user inputs for start and end times for the linear region of the response.

The multistat has an accuracy (or systematic error) of ± 0.1 % of full scale. Based on Figure 3-12, thermal conductivity tests will require input currents between 1500 and 4000

mA. This will require the multistat to operate in the 5000 mA current range, where the measurement accuracy is ± 5 mA. Based on the nominal resistance of the platinum wire, the measured voltages will be in the range of 50 to 150 mV. This will require the multistat to operate in the 1000 mV voltage range, where the measurement accuracy is ± 1 mV. Using this information and Equation 3.16, the uncertainty in the measurement of resistance during a typical thermal conductivity test will be between ± 0.25 and ± 0.70 mΩ.

For a typical test with a temperature rise of 3 K, Equation 3.20 shows that the change in resistance (used in the calculation of the slope, *m*) of the platinum wire is approximately 0.43 mΩ. Because the change in resistance for a typical test is of the same order of magnitude as the uncertainty in the resistance measurement, some concern is raised about the validity of the calculation of the slope, and thus the validity of the entire measurement. However, because the calculation of *k* is based on a differential measurement of resistance (Equations 3.12 and 3.15), any measurement bias (or systematic error) is eliminated, leaving only precision error. Thus, measurement precision is of primary concern. The precision of the multistat is not specified by the manufacturer[1], but can be determined statistically by repeated measurements. The effect on uncertainty in the slope, *m* can be determined by the procedure described in Section 3.1.3. The resulting uncertainty in the slope is used in the calculation of the uncertainty.

5.1.3 Reference Material

As validation of the accuracy of the measurement apparatus, a reference material of known thermal conductivity was tested. The reference material is Ottawa silica sand, acquired from the Silica Sand Company. Ottawa sand is well-known for its uniform-size spherical particles. Examination of the sand confirmed that the particles were of consistent size and shape, with most grains spherical or slightly oblong and approximately 0.6 mm in diameter. Data on the thermal conductivity of Ottawa sand in air is readily available from several sources, although no specific standard exists for this property. Table 5-1 provides thermal conductivity data for Ottawa sand in air collected from several sources. Bulk density is defined as the density of the sand/air mixture. If the solid density of Ottawa sand is

[1] The manufacturer does specify the resolution of the analog to digital converters employed in the instrument. These 16-bit converters have a resolution of 1 part in 65,536, setting a lower bound on the precision at 0.002 %.

known, bulk density is a measure of how well the sand particles are packed together. Knowledge of the bulk density is important because the thermal conductivity can change based on how tightly the sand particles are packed. The solid density of the Ottawa sand from the Silica Sand Company was measured by submerging a known mass of sand in water and measuring the volume change of the liquid. The solid density was found to be 2.7 g/cm^3, which is very close to the published value of 2.65 g/cm^3.

Prior to loading the sample cylinder into the pressure vessel, the bulk density of the sand was measured in order to compare it with the value given by the NIST Building Materials Database. Currents ranging from 500 to 3000 mA were applied to the wire and the results analyzed in accordance with the procedures described in Section 5.1.2.

Table 5-1 Reference data for Ottawa sand.

Source	Bulk Density	k
NIST Building Materials Database, 1955[1]	1615 kg/m^3	0.306 W/mK
CRC Handbook	n/a	0.33 W/mK
Dedrick [12][2]	n/a	0.30 W/mK

5.1.4 Repeatability Analysis

Two repeatability analyses were conducted on the sample of Ottawa sand in air. These analyses quantify the amount of scatter to be expected in the data and also provide an opportunity to build familiarity with the test apparatus before testing the metal hydride material.

The first analysis repeats the thermal conductivity measurement on the same sample of sand, without any disturbance to the apparatus between tests. This test evaluates the repeatability of the measurement process by itself. A current of 2000 mA is chosen based on Figure 3-12 for an expected value for *k* of about 0.3 W/mK. This current is applied for 500 seconds, then the resulting data analyzed in accordance with Section 5.1.2. A total of twelve measurements are taken.

[1] Steady-state plate method.
[2] Thermal probe method (ASTM D-5334).

The second analysis repeats the measurement on a new sample of sand each time. This analysis captures the additional measurement uncertainty associated with the way in which the sand is loaded into the cylinder. For each measurement, the sample is removed from the pressure vessel, emptied and refilled with different sand. While care is taken to be consistent in how the sand is loaded into the sample cylinder and packed, some variability is to be expected. Two levels of current, 2000 and 1500 mA, are applied to the wire for 150 seconds. Twelve measurements are taken at each current level.

5.1.5 Pressure Measurements with Sand

After using Ottawa sand to validate the measurement apparatus, a pressure study is performed with sand in hydrogen. In addition to improving familiarity with the measurement procedures, this investigation offers an opportunity to observe the Knudsen effect and to evaluate the variation in thermal conductivity with pressure. Pressures from ambient to 250 psi (17 bar) are investigated at room temperature (22-23 °C). Gas pressure is controlled by adding gas to or removing gas from the pressure vessel. A current of 4000 mA was applied to the wire and the resulting data analyzed in accordance with Section 5.1.2.

5.2 Metal Hydride Material

5.2.1 Safety

Doped metal hydrides, including sodium alanate, are extremely reactive substances and extreme care must be taken when handling them. When exposed to oxygen or any amount of moisture (including humid air), sodium alanate will react, and can react violently enough to cause high heat and fire. In addition to the safety hazard, any exposure will ruin the sample, rendering the material useless. All work with this material was conducted in an inert atmosphere, which required the use of a glove box to transfer the material from one vessel to another. In addition, any pipes that may carry gas into or out of the pressure vessel had to be purged of air so as not to contaminate the material. Exposure to even small amounts of oxygen or water can be detrimental.

5.2.2 Synthesis

Titanium-doped sodium alanate was synthesized at the Florida Solar Energy Center. The raw materials were $NaAlH_4$ powder from Sigma Aldrich (CAS #13770-96-2) and $TiCl_4$ catalyst (Acros). Batches consisting of 4 g of $NaAlH_4$ and 0.02 mL (0.25 mol %) $TiCl_4$ were ball milled together for a total of 60 minutes in a SPEX 8000 high-energy ball mill. A total of approximately 30 grams was synthesized. Before shipping to Virginia Tech, the sample was discharged by heating through temperature-programmed desorption (TPD) at 2 °C/min to 250 °C. The sample was then recharged under 665 psi (45.2 bar) hydrogen pressure at 150 °C for 24 hours, then left to cool for another 24 hours. This was considered the first desorption/absorption cycle. The solid density of the sodium alanate was reported by the Florida Solar Energy Center as 1.24 g/cm^3.

5.2.3 Activation

The sodium alanate arrived from the Florida Solar Energy Center in a sealed glass container under argon gas. In a nitrogen glove box, 28.4 g of sodium alanate powder were transferred into a stainless steel beaker and loaded into the Parr pressure vessel. The powder was dark grey in color and the particles were extremely fine. The particles tended to pack together easily and required some disturbance to loosen.

Before the commencement of testing, the sample was desorbed and recharged and then cycled a second time. The desorption step began from ambient temperature and pressure, heating to 150 °C and using the gas volume measurement system to bleed off known amounts of hydrogen and measure the amount of gas evolution. The initial desorption cycles had a hydrogen release of 4.68 wt%. Absorption was executed at constant volume at 125 °C and a starting pressure of 1500 to 1800 psi. The closed vessel was left for 24 hours. After cooling to room temperature and pressurizing again to 1500 to 1800 psi, it was left again for another 24 hours. During absorption, hydrogen uptake was not measured. After the second absorption step, the sample was cycled again. During the second cycle, the desorption step yielded the same hydrogen release (4.68 wt%) as during the first cycle.

5.3 Effective Thermal Conductivity Measurements

The effective thermal conductivity for sodium alanate was measured as a function of pressure for the fully-hydrided and the fully-dehydrided condition. In addition, an exploratory study was undertaken to determine the thermal conductivity at intermediate values of composition along a pressure-composition isotherm (PCI).

Prior to testing, the metal hydride material was loaded into the sample cylinder in a nitrogen glove box. The mass and depth of the powder in the cylinder were recorded, and the sensors connected. The head of the pressure vessel was sealed according to manufacturer specifications and the vessel was pressure tested with inert helium gas, which does not react with the metal hydride and has a leak rate similar to hydrogen. One small leak was detected and corrected by tightening the fitting. After this correction, the vessel was held at room temperature for 48 hours at 2000 psi (136 bar), which corresponds to approximately 140% of the anticipated maximum operating pressure.

5.3.1 Pressure Measurements

To isolate the effect of pressure on effective thermal conductivity of the metal hydride, the first investigation varied the hydrogen pressure at the fully-hydrided and fully-dehydrided states. Since the material was in the fully hydrided state after cycling, this was a natural first examination. The pressure range investigated was ambient to 1470 psi (100 bar), which is the maximum practical filling pressure suggested for prototype sodium alanate systems [9]. The fill gas was hydrogen.

To minimize hydrogen desorption and absorption, the temperature of the vessel was held at ambient conditions (22 to 23 °C). Holding this low temperature minimizes the reaction rate of the hydride. This minimizes the risk of desorption of hydrogen at low pressures in the fully-hydrided state and also minimizes the risk of absorption of hydrogen at high pressures in the fully-dehydrided state. Hydrogen pressure was regulated by adding gas to or releasing gas from the pressure vessel. Care was taken to avoid rapid release of gas, as this could possibly disturb the hydride powder in the sample cylinder. After each change in gas pressure, time was given to allow the vessel to return to steady temperature.

5.3.2 Exploratory Composition Investigation

The effect of composition on effective thermal conductivity was investigated by conducting a preliminary PCI curve. This technique holds temperature constant while varying composition by releasing hydrogen gas from the pressure vessel. The mass of gas released was measured by the gas volume measurement system. Using this mass information and pressure and temperature data from inside the vessel, the hydride composition was calculated using the Beattie-Bridgeman equation of state for hydrogen. The nature of the PCI curve allows a fairly constant pressure to be maintained over a wide range of compositions. The pressure is maintained at the plateau pressure of the metal hydride discussed in Chapter 1, deviating only at very high and very low compositions. The Na-Al-H system has two plateau pressures, corresponding to the two steps of decomposition.

Initially, the intent was to perform the preliminary PCI measurement at a temperature close to fuel cell operating temperatures (80 to 90 °C), but the reaction kinetics were found to be prohibitively slow, even for the faster decomposition of $NaAlH_4$. Therefore, the temperature was increased to 150 °C, where the kinetics of decomposition are known to be considerably faster [20, 24]. Previous work has shown that temperature does not have a significant effect on effective thermal conductivity, suggesting the results at 150 °C are applicable to lower temperatures [12]. The plateau pressure at this temperature is approximately 880 psi (60 bar) for the first reaction step [23]. At 150 °C the plateau pressure of the second decomposition step is roughly 70 psi (5 bar) [23]. Because of the low pressure of the second step and the slow kinetics, effective thermal conductivity measurements were taken only during the first decomposition step.

Beginning at the fully hydrided state and room temperature, hydrogen pressure is applied to 1000 psi (68 bar). After the vessel is heated, the pressure is higher, and is well above the plateau pressure of the hydride, ensuring testing begins at the fully hydrided state. At each composition tested, the sample is allowed to come to steady pressure and then at least five thermal conductivity measurements are recorded. After completion of these measurements, a portion of hydrogen gas is released and the system is given time to come to steady pressure at a new composition. Typically, full decomposition of the hydride is necessary to establish the fully-dehydrided reference state so that the composition at each

step and the total amount of hydrogen desorbed can be determined. However, due to the limited nature of this investigation, the full composition was assumed to be the same as that from the cycling tests performed during activation, 4.68 wt %.

5.4 Summary

This chapter described the experimental approach to gathering data. First, the validation of the measurement apparatus ensures the measured data is accurate. This accuracy depends on both the accuracy of the instruments and the validity of the test mechanism itself. A reference material provides confirmation that the measurement is producing reasonable data. Ottawa silica sand, for which thermal conductivity data is available, serves as this reference material. Conducting a repeatability analysis gives confidence in the ability of the apparatus to produce consistent results and builds familiarity with the measurement procedures. An investigation into the effect of pressure on the effective thermal conductivity of the Ottawa sand in a hydrogen environment provides verification of the Knudsen effect and also adds to the familiarity with the test procedures. The sodium alanate material was synthesized and subjected to one cycle at the Florida Solar Energy Center. An additional two cycles were conducted at Virginia Tech. After these preliminary cycles, tests on sodium alanate included fully-hydrided and fully-dehydrided pressure measurements and an exploratory composition investigation. All tests were conducted in accordance with applicable safety procedures for sodium alanate and for hydrogen.

The next chapter presents the results from these experiments and a discussion of the data. Chapter 7 offers conclusions and possibilities for future work.

6 RESULTS

This chapter describes the results of the experimental investigation. First, the effect of current input and the results of measurements on Ottawa sand are presented. Then, the results of measurements on the Na-Al-H system are presented, followed by a chapter summary.

6.1 Measurements on Sand

The study of Ottawa sand includes a measurement to compare experimental values with published values, a repeatability analysis and a pressure-dependence investigation. Full results are presented in Appendix D.

6.1.1 Reference Measurement

A plot of the change in temperature versus the natural log of time for a typical effective thermal conductivity measurement is shown in Figure 6-1. This plot illustrates the non-linear behavior of the temperature response at the beginning and end of the test, which is a feature observed in similar studies [12, 14]. The initial non-linearity is thought to be due to the thermal capacity of the wire or the neglected terms from Equation 3.5, while the non-linearity at the end of the test is due to the influence of the outer wall and the breakdown of the assumption of an infinite cylinder.

Figure 6-1 also shows the temperature response of the three additional thermocouples located inside the pressure vessel. TC_A and TC_B represent the temperatures recorded at opposite sides of the sample cylinder wall at the midpoint of the sample cylinder length. These two readings track closely, and provide a means to capture the interaction of the heat output of the wire with the outer wall of the cylinder. They also provide confirmation of steady-state conditions inside the cylinder prior to running a test. TC_C represents the thermocouple probe in the open space inside the pressure vessel. The response of this measurement lags behind TC_A and TC_B because it takes more time for the heat to travel through the glass outer wall of the cylinder and through the surrounding gas. It also helps in determining when steady-state has been reached. The green vertical lines represent the start

and stop times of the slope calculation. They correspond to the linear portion of the response and are chosen by visual inspection of the data.

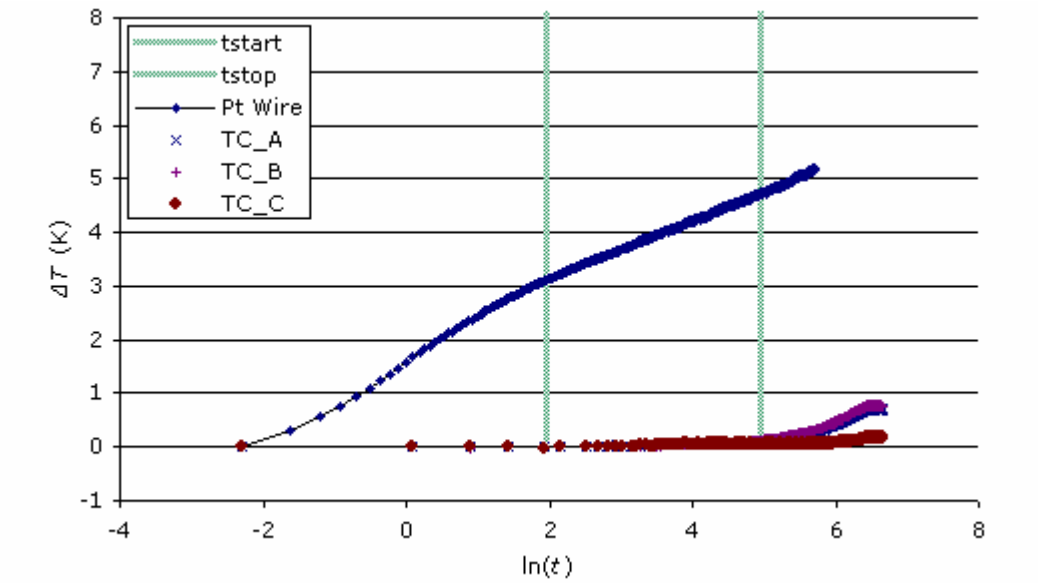

Figure 6-1 Typical results for effective thermal conductivity measurement.

A summary of values of effective thermal conductivity are presented in Table 6-1. For the present study, values for bulk density, effective thermal conductivity and uncertainty were determined for Ottawa sand in air at ambient temperature and pressure in accordance with procedures described in Sections 5.1.3, 5.1.2, and 3.1.3, respectively. The value of effective thermal conductivity used for validation of the measurement apparatus is taken from an average of the twelve measurements made in the first repeatability analysis. The largest difference from one of the published values is with that of Dedrick [12] with a difference of 5.3 %, or roughly three times the amount of uncertainty in the measurement. The uncertainty in the measurement made by Dedrick [12] was not published. The closest agreement is with the value from the NIST Building Material Database, with a difference of 3.4 %. Additionally, the current results for bulk density are within 3.2 % of the NIST data. These results show that the measurements made with the platinum hot wire technique are directly in line with the available data.

Table 6-1 Summary of measured and published data for Ottawa sand.

Source	Bulk Density	k	Uncertainty
Present Study	1.670 g/cm^3	0.317 W/mK	2.22 %
NIST Building Materials Database, 1955[1]	1.615 g/cm^3	0.306 W/mK	
CRC Handbook		0.33 W/mK	
Dedrick [12][2]		0.30 W/mK	

6.1.2 Effect of Input Current

When collecting preliminary data for the reference measurement, several experiments were run to observe the influence of varying the input current to the wire. The results of this investigation are shown in Figure 6-2 for currents ranging from 500 to 2000 mA. The start and stop times for the linear evaluation period were based on the trace for 2000 mA and applied to each of the curves for consistent evaluation. At input currents of 500 and 1000 mA, the noise in the measurement system dominates the data, and it is not possible to discern a linear region in which to calculate *k*. This noise is presumably due to the precision error in the multistat described in Section 5.1.2. Although the low temperature rise at these low input currents is desirable in terms of minimizing the effects of radiation and gas evolution, higher currents reduce the effect of noise and allow for a more accurate measurement. At current inputs of 1500 and 2000 mA, the noise is reduced to levels acceptable for determining the linear region of the trace by inspection, but temperature rise is increased. A tradeoff is apparent between the noise in the data and the assumption of a homogenous bed.

[1] Steady-state plate method.
[2] Thermal probe method (ASTM D-5334).

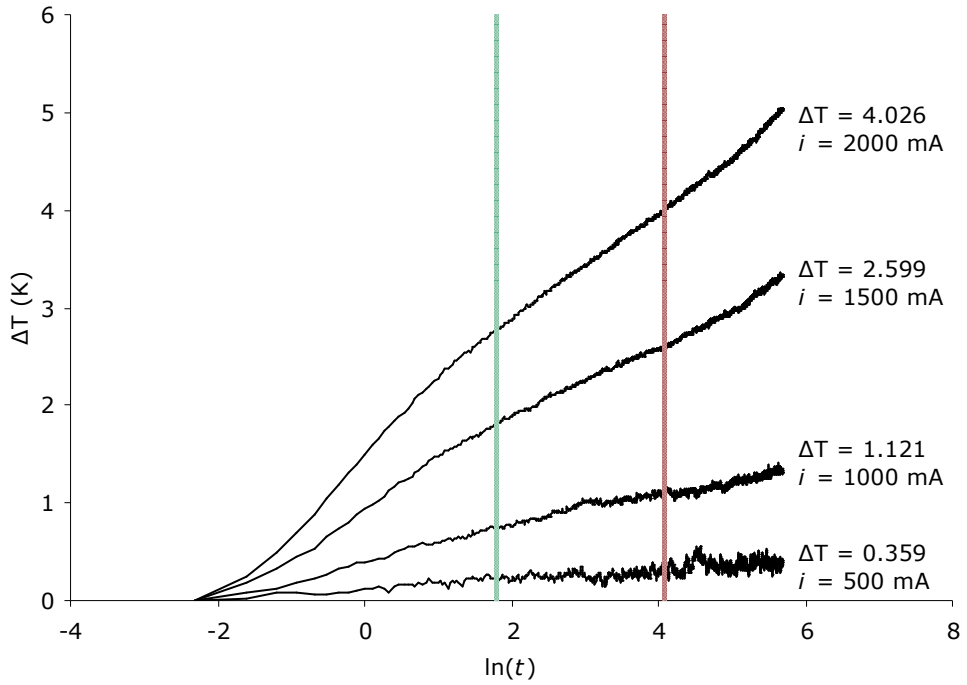

Figure 6-2 Effect of current on reference measurement.

6.1.3 Repeatability Analysis

The first repeatability analysis examines the variation in the data when the measurement apparatus is not refilled with sand or otherwise changed between tests. Table 6-2 provides tabulated results and a summary for this investigation, while Figure 6-3 shows the results of this analysis as a function of measurement number. The average uncertainty of the measurements (based on error propagation) is 0.0070 W/mK. The mean value of thermal conductivity is 0.317 W/mK, with a standard deviation of 0.0051 W/mK, or 1.58 %, which is less than the average uncertainty for a single measurement. Additionally, the average linear correlation coefficient for the fit of the slope of $dR/d(\ln(t))$ is 0.9986, indicating the linear fits of the twelve measurements are very strong. The start and stop times for all twelve of the linear fits were 7 and 140 seconds, respectively.

Table 6-2 Results of first repeatability analysis (T = 298 K, P = 1 bar).

Repetition	k (W/mK)	σ_k (W/mK)	m (Ω x 10^6)	σ_m (Ω x 10^6)	ΔT (K)
1	0.315	0.0070	54.22	0.0029	4.74
2	0.313	0.0069	54.72	0.0031	4.72
3	0.324	0.0072	52.79	0.0030	4.73
4	0.312	0.0069	54.84	0.0023	4.77
5	0.324	0.0072	52.83	0.0024	4.71
6	0.316	0.0070	54.21	0.0026	4.74
7	0.311	0.0069	54.86	0.0034	4.73
8	0.314	0.0070	54.44	0.0029	4.68
9	0.322	0.0071	53.12	0.0030	4.71
10	0.323	0.0072	52.86	0.0039	4.67
11	0.321	0.0071	53.22	0.0032	4.69
12	0.313	0.0069	54.66	0.0028	4.69
Average	**0.317**	**0.0070**	**53.90**	**0.0030**	**4.72**
Std. Dev.	**0.0051**	**-**	**0.86**	**-**	**0.028**
95% Conf.	**0.0029**	**-**	**-**	**-**	**-**

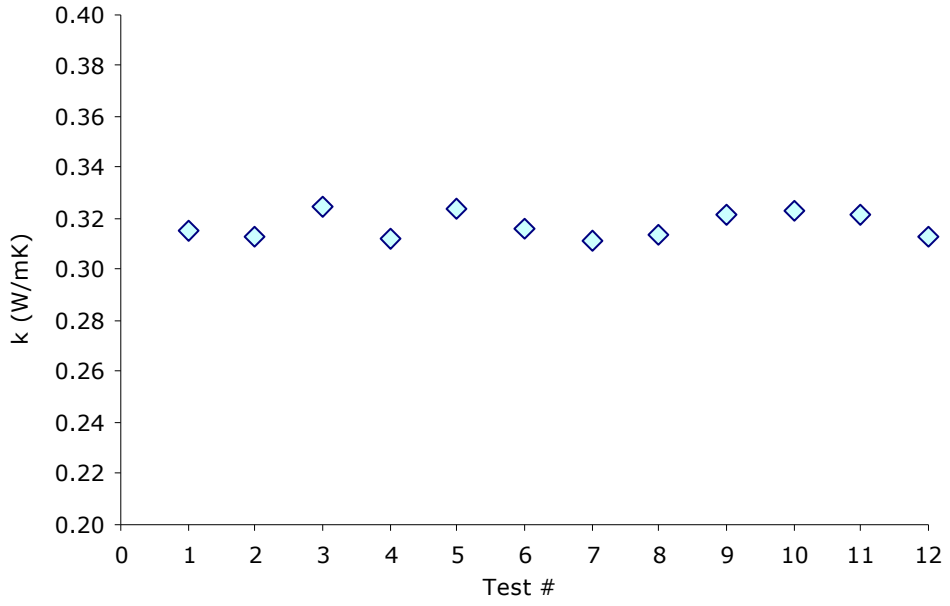

Figure 6-3 Results of first repeatability analysis (T = 298 K, P = 1 bar).

Based on Figure 3-12, the choice for input current for the first repeatability analysis was 2000 mA. The results presented in Figure 6-2 confirm that this selection for input current produces results with a well-defined linear region. However, the data from the repeatability analysis show that the temperature rise was larger than expected: the finite

element results are based on a temperature rise of 3 K, but the data show an average rise of 4.72 K. The selection of the linear "evaluation" region has an effect on both the maximum temperature rise of the test and on the value of *k*. If, for example, the upper bound of the evaluation region is decreased to from 140 seconds to 70 seconds, the temperature rise decreases to 4.02 K and the average value of *k* changes to 0.316 W/mK. If the upper bound is lowered further, to 30 seconds, the temperature rise decreases further to 3.74 K and the average value of *k* changes to 0.312 W/mK. Human error in choosing start and stop times would not be as drastic as these changes, but might be on the order of 5 to 10 seconds. These are not drastic variations in calculated values of *k*, but are indicative of the uncertainty present in the data. As illustrated in Figure 6-4, changes to the start and stop times cause some measurements of *k* to rise and others to fall. This is due to inherent scatter and noise in the recorded data that is present regardless of human input to the calculation routine. These results seem to suggest that the technique is generally robust, provided that sufficient data are collected during the test time to yield a good estimate of the slope.

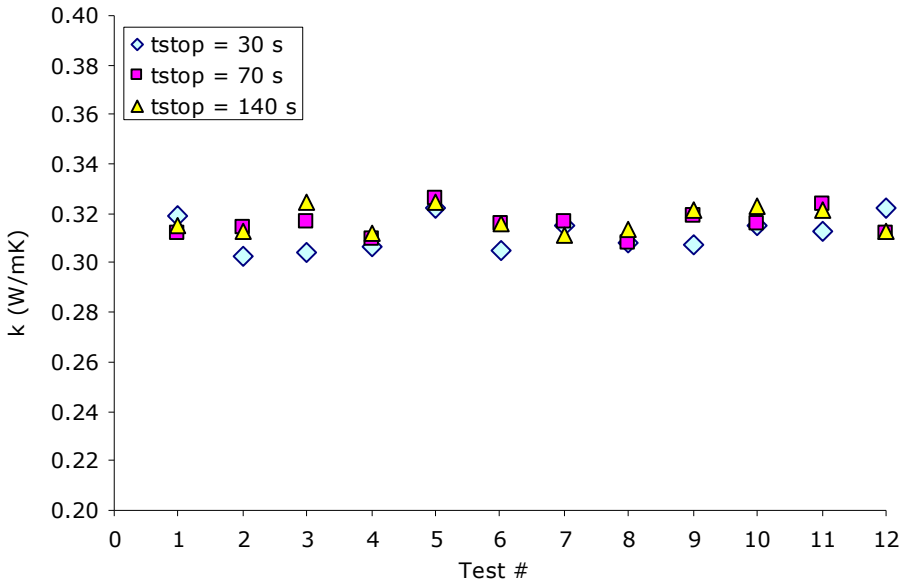

Figure 6-4 Variation of stop time on calculation of *k*.

The second repeatability analysis examines the effect of refilling the sample apparatus for each measurement. Again, twelve measurements were conducted with the apparatus emptied and refilled before each test. In this investigation, two different levels of

current were used for each fill: 1500 and 2000 mA. The bulk density was also measured for each fill to examine the consistency of the sand filling procedure. Tabulated results are presented in Table 6-3 and Table 6-4. Graphical results from this analysis are compared to the average and standard deviation of the first repeatability analysis in Figure 6-5 (as a function of test number) and in Figure 6-6 (as a function of bulk density).

Table 6-3 Results from second repeatability analysis, i = 1500 mA.

Repetition	k (W/mK)	σ_k (W/mK)	m (Ω x 10^6)	σ_m (Ω x 10^6)	ΔT (K)
1	0.288	0.0046	50.19	0.026	2.35
2	0.313	0.0050	46.24	0.017	2.29
3	0.314	0.0050	46.09	0.019	2.31
4	0.328	0.0053	44.17	0.018	2.29
5	0.323	0.0052	44.71	0.020	2.24
6	0.349	0.0056	41.22	0.018	2.23
7	0.353	0.0057	40.83	0.020	2.37
8	0.307	0.0049	46.95	0.017	2.44
9	0.341	0.0055	42.27	0.018	2.28
10	0.339	0.0054	42.24	0.016	2.33
11	0.325	0.0052	44.19	0.023	2.31
12	0.335	0.0054	42.93	0.021	2.41
Average	**0.326**	**0.0052**	**44.34**	**0.019**	**2.32**
Std. Dev.	**0.0187**	**-**	**2.708**	**-**	**0.062**
95% Conf.	**0.0106**	**-**	**-**	**-**	**-**

Table 6-4 Results from second repeatability analysis, i = 2000 mA.

Repetition	k (W/mK)	σ_k (W/mK)	m (Ω x 10^6)	σ_m (Ω x 10^6)	ΔT (K)
1	0.311	0.0047	83.07	0.016	4.16
2	0.323	0.0048	80.06	0.019	4.07
3	0.328	0.0049	78.87	0.021	4.09
4	0.327	0.0049	79.28	0.020	4.11
5	0.337	0.0051	76.24	0.016	4.02
6	0.332	0.0049	77.36	0.017	4.18
7	0.317	0.0048	81.18	0.017	4.29
8	0.330	0.0049	78.17	0.017	4.24
9	0.319	0.0048	80.88	0.015	4.25
10	0.327	0.0049	78.71	0.024	4.07
11	0.329	0.0049	78.11	0.021	4.12
12	0.310	0.0047	83.11	0.016	4.37
Average	**0.324**	**0.0049**	**79.59**	**0.018**	**4.16**
Std. Dev.	**0.0083**	**-**	**2.148**	**-**	**0.104**
95% Conf.	**0.0047**	**-**	**-**	**-**	**-**

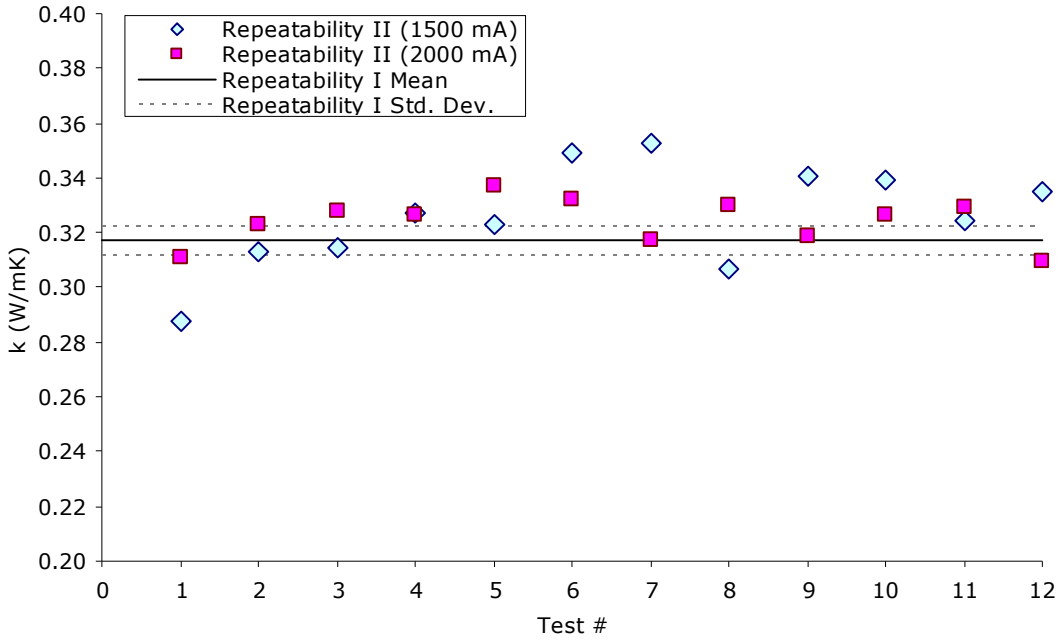

Figure 6-5 Results of second repeatability analysis compared to average and standard deviation of first repeatability analysis.

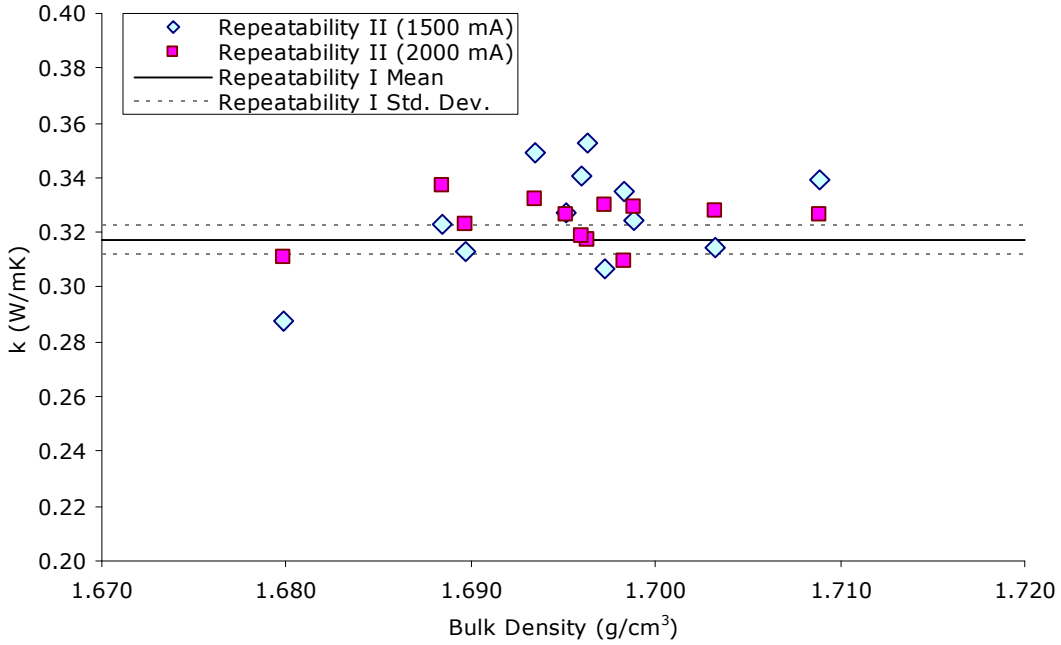

Figure 6-6 Results of second repeatability analysis as a function of bulk density compared to average and standard deviation of first repeatability analysis.

The set of effective thermal conductivity measurements taken with the higher current has lower standard deviation and less variance. However, the measurements taken at the lower current level have a temperature rise that is closer to the desired value of 3 K. Both sets of data have about the same uncertainty in individual measurements, but the data at 1500 mA has a 95% confidence interval that is about twice the measurement uncertainty based on propagation of error calculations. For the 2000 mA sample, the 95% confidence interval of the sample is about the same as the uncertainty based on propagation of error calculations. Since the two samples were taken from the same set of twelve fills, there is an identical amount of scatter in the values of bulk density.

Figure 6-7 compares the results from the first repeatability analysis and the 2000 mA data from the second repeatability analysis. For the 2000 mA study, the average uncertainty of the measurements is ± 0.0049 W/mK and the 95% confidence interval is ± 0.0047 W/mK. The uncertainty in the first repeatability analysis is ± 0.0070 W/mK and the 95 % confidence interval is ± 0.0029 W/mK. The increase in the 95% confidence interval for the second repeatability analysis indicates the fill procedure introduces some amount of additional uncertainty in the measurement.

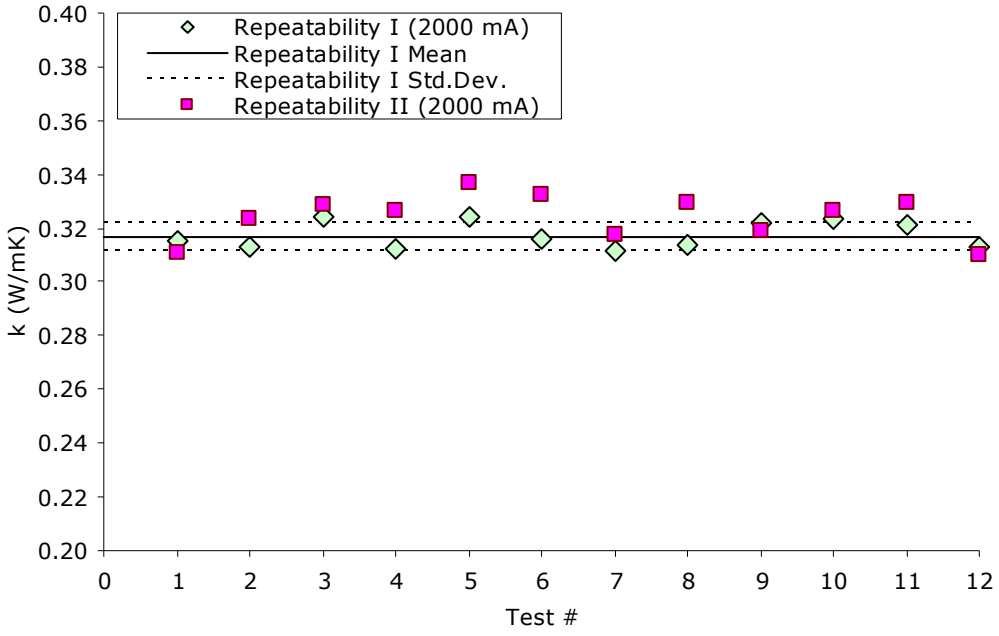

Figure 6-7 Comparison of first and second repeatability analyses.

The more important conclusion, however, is that in the second repeatability analysis the lower applied current level caused significantly more scatter in the data, a results also seen near the beginning of the chapter when the influence of input current was examined for a single measurement. This conclusion points to a fundamental tradeoff for thermal conductivity measurements on sodium alanate and on metal hydrides in general. In order to minimize the evolution of hydrogen during tests on sodium alanate, it is important to also minimize the temperature rise of the sample. The assumption of a homogenous bed depends on a small temperature rise, and thus a small risk that the evolution and transport of hydrogen gas will have an impact on the conductivity measurement. Since the applied current level is directly tied to the temperature rise, a fundamental trade-off exists between reducing scatter by increasing current and maintaining the validity of the homogenous bed assumption by reducing current and hence temperature rise. This will be an important consideration for the effective thermal conductivity measurements of sodium alanate in the next section.

6.1.4 Pressure Investigation

The effect of hydrogen gas pressure on the effective thermal conductivity of the Ottawa sand is shown in Figure 6-8. The Knudsen number is also shown as a function of pressure, calculated with d = 74 pm (diameter of H_2 molecule) and L_C = 0.6 mm (average sand grain size). For the range of pressures investigated, Kn varies between 0.002 (low pressures) and 0.0001 (high pressures). In the range of 0.002 > Kn > 0.001, the effective thermal conductivity increases sharply with pressure. For Kn < 0.001, the effective thermal conductivity is constant with pressure. This indicates the Knudsen effect transitions to a plateau region around Kn = 0.001 for this situation. Using the relations given in Equations 1.2 and 1.3, Kn = 1 is found to correspond to a pressure of 0.003 bar. Thus, the data presented here represent only a small portion of the pressure-dependent region of the Knudsen effect. If a vacuum was drawn, one would expect to see the thermal conductivity continue to decrease through vacuums of 0.0003 bar and below, then level out at much lower pressures. However, without equipment to draw a vacuum in the hydrogen atmosphere, this investigation can only look at pressures at ambient and above.

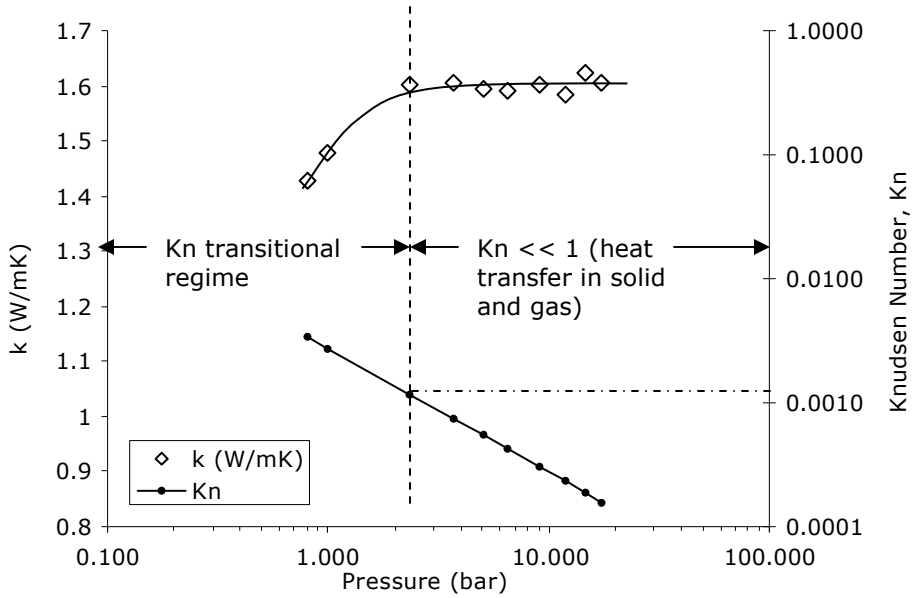

Figure 6-8 Effect of hydrogen gas pressure on *k* and Knudsen number for Ottawa sand.

It is interesting to note the dramatic increase in effective thermal conductivity of the sand in a hydrogen atmosphere compared to sand in an air atmosphere. At atmospheric pressure, the effective thermal conductivity in hydrogen is about 1.5 W/mK, as compared to 0.32 W/mK in air. This dramatic increase is due to the excellent thermal conductivity of hydrogen gas, which is a characteristic that is beneficial to the development of metal hydride storage systems. On the other hand, since the thermal conductivity of the storage system is so dependent on the hydrogen gas, the thermal conductivity decreases significantly as pressure decreases (system is emptied). Thus, the rate at which hydrogen can be released will suffer due to decreasing heat transfer. The precise quantification of the effects of operating conditions on effective thermal conductivity is crucial to storage system development, and is the focus of the next section.

6.2 Measurements on the Na-Al-H System

Measurements of the effective thermal conductivity of the Na-Al-H system include a pressure investigation on the fully-hydrided and fully-dehydrided material and an exploratory

study of the relationship of composition and effective thermal conductivity. Full results are presented in Appendix E.

6.2.1 Pressure Investigation

The pressure investigation seeks to isolate the relationship of pressure to effective thermal conductivity. To accomplish this, pressure is varied while temperature is held constant at the fully-hydrided and fully-dehydrided states. Composition is held constant by keeping the sample at room temperature, thus keeping the reaction rate low. The thermal conductivity measurement technique is applied as with the Ottawa sand, but more care is taken to keep the temperature rise to 3 K or less to prevent desorption or absorption of hydrogen.

Figure 6-9 shows the results of the fully-hydrided pressure investigation with the corresponding Knudsen numbers for the range of pressures covered. For the metal hydride powder, the characteristic length, L_C, is on the order of 5 μm [23]. In contrast to the results for Ottawa sand there is no plateau region, suggesting that the system remains within the transitional range of Knudsen numbers throughout the study, and a relatively large effect for pressure should be observed. In this range, the data vary between Kn = 0.3 at pressure near ambient and 0.002 at high pressures. Because of this range of Knudsen number, the thermal conductivity varies significantly with pressure, but there is no plateau within this range, simply a linear relationship with the log of pressure. If the investigation were extended to higher pressures, it is expected a pressure plateau would be reached somewhere around a Knudsen number of 0.001, corresponding to roughly 300 bar.

Because of the linearity of the data, a least-squares logarithmic fit results in an equation that describes the effective thermal conductivity over the range of 1 to 100 bar. The resulting equation is shown in Figure 6-9 and is applicable to the fully-hydrided phase at room temperature only, where P_0 is equal to 1 bar. A quantification of the amount of scatter is accomplished by calculating the standard deviation of the empirical data set from the linear fit. This results in a standard deviation of ± 0.0122, or 2.44 %, and a 95% confidence interval of ± 0.00014 which is better than what was found in the first repeatability analysis. Thus, it is concluded that the amount of scatter in the data is reasonable.

The form of the data compares well with the work of Dedrick [12], who found a similar linear relationship for effective thermal conductivity at the fully-hydrided state at room temperature. They tested in the range of 1 to 100 atm (0.987 to 98.7 bar) and found the effective thermal conductivity to vary linearly from 0.5 to 0.7 W/mK in the fully-hydrided phase. While the present results varied from 0.4 to 0.6 W/mK at the same temperature and over the same pressure range, the characteristic relationship remains the same, with the same change in *k* for the given pressure range. Although it is not possible to explain with certainty the offset in the results, the discrepancy could be attributed to a number of factors, including packing density, particle size, levels of catalyst, or the measurement device itself.

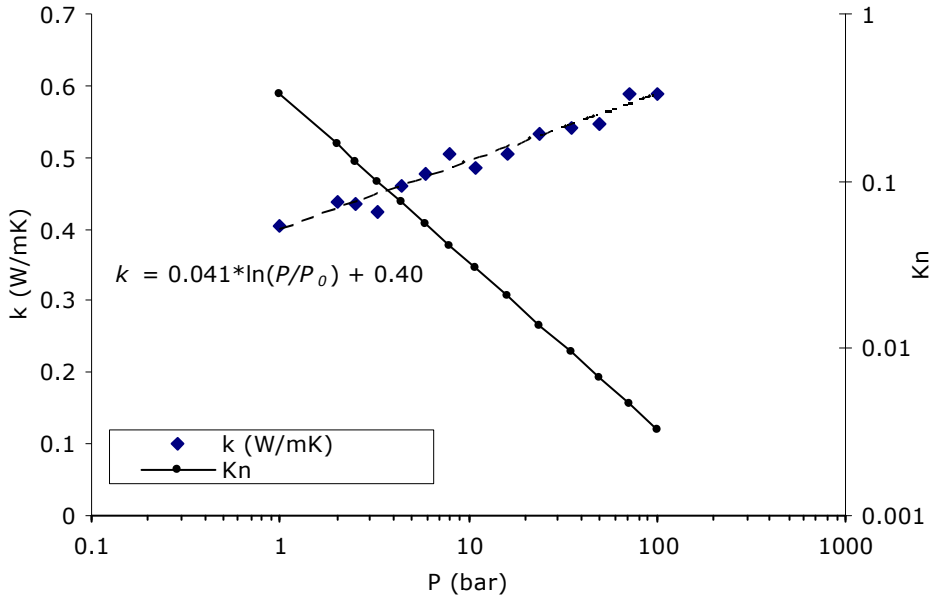

Figure 6-9 Effect of pressure on *k* for sodium alanate in hydrogen.

Figure 6-10 shows the results from the fully-dehydrided pressure investigation along side those of the fully-hydrided investigation. The thermal conductivity is significantly higher for the dehydrided sample, which is consistent with the work of Dedrick [12]. However, Dedrick found the thermal conductivity of the dehydrided sample to vary from 0.7 to 0.9 W/mK over a pressure range of 1 to 35 bar. The current work measures the thermal conductivity in this range of pressure to vary from 0.5 to 0.6 W/mK. Additionally, this study

extends the pressure range to a maximum of 50 bar, where the thermal conductivity of the dehydrided sample rises to approximately 0.65 W/mK. The data for the dehydrided sample again follow a linear trend, with a slope almost identical to that of the hydrided sample. The equation for the line based on a least-squares logarithmic fit is shown in Figure 6-10. Visually, scatter for the dehydrided sample is comparable to that for the hydrided sample, and calculation gives a standard deviation for the linear fit of ± 1.89 % and a 95% confidence interval of ± 0.00034 W/mK.

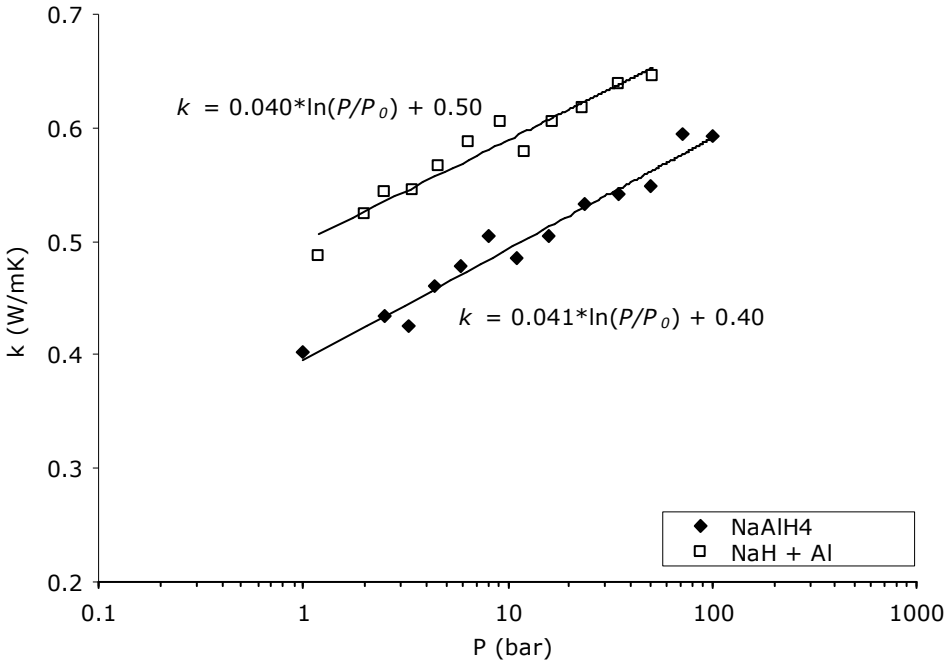

Figure 6-10 Comparison of hydrided and dehydrided pressure investigations.

6.2.2 Exploratory Composition Study

As discussed in Chapter 1, a PCI curve allows composition to be varied at a relatively constant pressure, so that for the most part, the relationship of composition to effective thermal conductivity can be observed. In this study, several data points are taken along a preliminary PCI curve. This curve is taken at an elevated sample temperature (150 °C) to increase the reaction kinetics, and thus improve the rate at which the sample comes to steady-state. Unfortunately, this encourages a higher reaction rate, making the sample more likely

to release gas when heat is transferred from the platinum wire to the sample. To reduce this effect, the temperature rise at the wire was maintained again to less than 3K.

Figure 6-11 illustrates the relationship between composition and pressure for the measurements taken at 150 °C. Testing began at full composition (approximately 4.68 wt %, based on activation), and proceeds from right to left on the graph. After an initial rapid decline in pressure between the first two points, the plateau pressure is observed to decrease slightly with decreasing composition. This behavior is typical for a real metal hydride, in contrast to the idealized PCI curve explained in Chapter 1. The plateau pressure measured in this study is roughly 70 bar (1030 psi), which corresponds well with the plateau pressure of 60 bar (880 psi) observed in the literature for the Na-Al-H system at this [23]. Because the second decomposition step occurs at a very low pressure at this temperature, a full curve was not taken. Therefore, the second decomposition step is not shown. Based on available literature [23] it is expected this step would commence around a composition of 1.5 wt %.

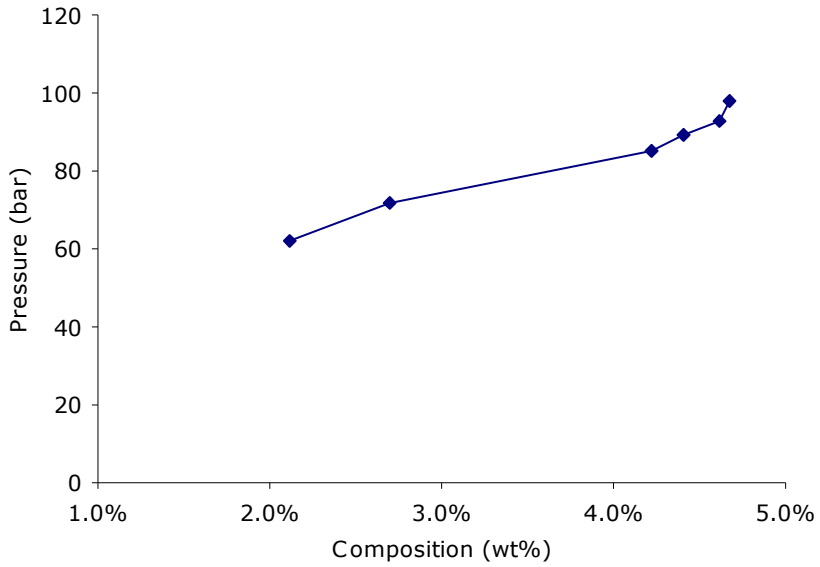

Figure 6-11 Pressure-composition results of exploratory study (T = 150 °C).

Figure 6-12 shows effective thermal conductivity as a function of composition. Each data point represents the mean of five measurements, and error bars represent one standard deviation from the mean. The effective thermal conductivity data is fairly constant at all

compositions, with each data point falling within the error bars of all other data points. Based on the results from the pressure investigation and pressure variation in Figure 6-11 (62 to 100 bar), one might expect to find some change in effective thermal conductivity over this range of compositions. However, based on the relationship derived from experimental data in Section 6.2.1 the thermal conductivity is only expected to change 0.02 W/mK for this range of pressures, which is well within the error bars shown. One other consideration is the difference in effective thermal conductivity between the fully-hydrided state ($NaAlH_4$) and the intermediate decomposition step (Na_3AlH_6). However, in the work of Dedrick [12], little variation was found between the effective thermal conductivity of these two states. There was a significant difference for the fully-dehydrided state, however. This warrants an investigation of the change in effective thermal conductivity between the intermediate decomposition step (Na_3AlH_6) and the fully-dehydrided state (NaH + Al).

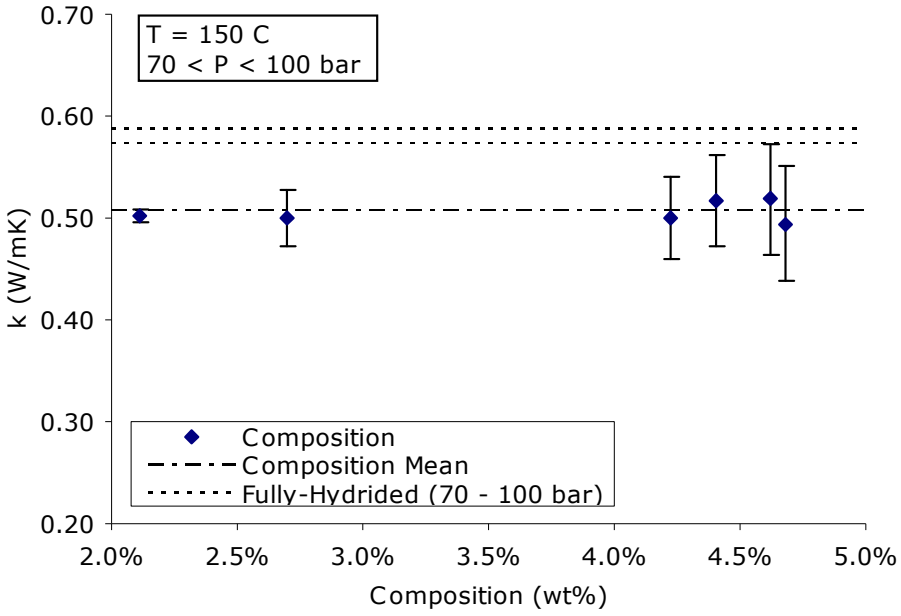

Figure 6-12 Effective thermal conductivity-composition results of exploratory study.

6.3 Summary

Several important findings were highlighted in this chapter. The validation of the effective thermal conductivity measurement apparatus was carried out by comparing measured data to published values for Ottawa silica sand. Very good agreement was found between the results of the experimental investigation and three sources of available data. This finding validates the accuracy of the measurement apparatus and provides confidence that further results are accurate.

Two repeatability analyses showed that low amounts of scatter are present in the data, especially for tests that use higher applied currents, indication a high level of precision. Additionally, the extent to which human judgment and error affect the calculation of k was deemed minimal because of the robustness of the results when varying the range of the linear fit. The effects of variation in packing, another opportunity for human influence, were shown to increase scatter, as indicated by the increase the 95% confidence interval. Unfortunately, a weakness in the test was also exposed, as there is a fundamental trade-off between the amount of scatter present in the data and the validity of the assumption of a homogenous bed with no mass transfer effects.

A pressure investigation with Ottawa sand and hydrogen gas showed that the Knudsen effect was responsible for a plateau in effective thermal conductivity above pressures of 2 bar, and was also responsible for a notable drop in effective thermal conductivity below 2 bar. A dramatic increase in effective thermal conductivity was observed in the sample of sand in hydrogen at all pressures versus the sand in air. This is due to the excellent thermal conductivity of hydrogen gas, and is seen as beneficial to hydrogen storage systems. However, the dependence on hydrogen gas to improve a system's thermal conductivity may be detrimental if the heat transfer becomes limited at low pressures.

The results of the fully-hydrided pressure investigation follow the same trend as the fully-hydrided results of Dedrick [12], the only known major investigation into the effective thermal conductivity of the Na-Al-H system. Although tested in the same range of pressures, the results of this investigation are uniformly about 0.1 W/mK lower than those of Dedrick. The relationship of effective thermal conductivity to pressure is comparable, however, as a

strong linear correlation exists between *k* and the logarithm of pressure. In this study, the effective thermal conductivity varied from 0.4 to 0.6 W/mK over a pressure range of 1 to 100 bar. There was a small amount of scatter in the data, comparable to the scatter present in the repeatability analyses.

The results of the fully-dehydrided pressure investigation also match qualitatively with Dedrick [12] in that the thermal conductivity was significantly higher in this state than in the fully-hydrided state. However, the results of the current study are 0.2 to 0.3 W/mK lower than those of Dedrick over the same range of pressure. The relationship of effective thermal conductivity and pressure in the fully-dehydrided state was again strongly linear with the log of pressure, a result also found by Dedrick [12].

The results of the exploratory composition investigation showed that effective thermal conductivity does not vary by a statistically significant amount with composition over the range tested (4.68 to 2.1 wt%). The pressure was shown to vary from 70 to 100 bar over the range of compositions tested. The results of the pressure-dependence investigation predict only a small change in *k* for this change in pressure, which is within the limits of error calculated for the composition results.

The following chapter concludes this study and offers suggestions for future work.

7 CONCLUSION

Determination of effective thermal conductivity is essential to the development of practical metal hydride-based hydrogen storage systems. This work investigated the effective thermal conductivity of the titanium-doped Na-Al-H system (sodium alanate) over a range of practical operating pressure and composition. A measurement apparatus based on an ideal linear heat source was developed and optimized using a finite element model. The goal of the study was to provide knowledge of the properties of the Na-Al-H and to compare these results with the findings of an existing similar study using an alternate measurement technique.

With regard to the design of the measurement apparatus, this study revealed the trade-off between the reduction of variance in the effective thermal conductivity data and assumptions about the homogeneity of the bed. An investigation into the effect of current input on a single measurement suggests scatter is introduced by noise in the resistance measurement. It was found that scatter, quantified by standard deviation, can be reduced significantly with an increase in applied current. However, any increase in current creates a larger temperature rise in the sample, especially at the wire-bed interface. Several important assumptions are contingent on a test that only causes a small temperature rise at all points within the test bed. For a metal hydride material, the most important of these assumptions is that an insignificant amount of gas evolution is caused by the heat generation of the wire. Any heat energy that is converted to chemical energy in the process of liberating hydrogen gas is no longer propagating outward through the medium via the process of conduction. This conversion of energy would clearly invalidate the theory of the test as described by Equation 3.1. Two other assumptions that could be invalidated by a large temperature rise in the bed are the assumption of insignificant radiation effects and the assumption that the test is conducted at a single temperature.

To reduce the variance in the data, it is recommended that a current source and voltage measurement device with lower measurement uncertainty be used. This would reduce the variance present in the measured resistance data, and thus allow for a smaller

temperature rise to be used in the measurement. When possible, a lower temperature rise is always desirable because it reduces the effects of gas evolution and radiation.

With regard to the effective thermal conductivity of the alanate material, the study demonstrated the significance of the Knudsen effect in the fully-hydrided state. Over the range of pressures investigated, corresponding to realistic operating conditions, the effective thermal conductivity varies linearly with the natural log of pressure, as described by the equation:

$$k = 0.041 * \ln(P / P_0) + 0.40 \ [W/mK] \ \ \{1 \le P \le 100 \text{ bar}\}, P_0 = 1 \text{ bar.} \qquad 7.1$$

Over this range of pressure, there was no plateau observed, which corresponds to the findings of Dedrick [12]. In contrast, the Knudsen effect was also observed in the pressure data for sand and hydrogen gas, but a pressure plateau was observed at pressures above about 2 bar (Kn < 0.001).

In the fully-dehydrided investigation, a similar linear relationship was observed. Over the range of pressures investigated, the effective thermal conductivity can be described by:

$$k = 0.040 * \ln(P / P_0) + 0.50 \ [W/mK] \ \ \{1 \le P \le 50 \text{ bar}\}, P_0 = 1 \text{ bar.} \qquad 7.2$$

Again in this range of pressure, no plateau was observed. These results were also consistent with Dedrick in that the thermal conductivity is significantly higher for the fully-dehydrided state. However, these results were 0.2 to 0.3 W/mK lower than those of Dedrick [12].

Another important finding concerns the relationship of effective thermal conductivity to hydride composition from the exploratory investigation. There was little composition-dependence found over the range of compositions tested. The pressure relationship described in Equation 7.1 above predicts a very small change in *k* for the range of pressures observed in the investigation. The change in effective thermal conductivity associated with the change in composition was within the limits of uncertainty of the prediction based solely on pressure. The work of Dedrick [12] also shows little variation in effective thermal conductivity

between the fully-hydrided and intermediate compositions, which supports the present findings.

As Table 1-1 indicates, a fill rate of 0.5 kg H_2/min is the goal in the FreedomCAR 2007 storage system targets. This rate is much higher than the target release rate of 0.0012 kg/min (0.02 g/s/kW) and is thus the more heat-transfer intensive criterion for a metal hydride storage system. Because of this, and because the fully-hydrided $NaAlH_4$ phase has the lowest thermal conductivity of the Na-Al-H system, the current results are valuable in that they capture the worst-case scenario for a sodium alanate storage system. This worst-case occurs towards the end of the filling process, where a majority of the material in the storage system has been converted to $NaAlH_4$. At this point the effective thermal conductivity is near the minimum for the Na-Al-H system, but heat transfer must still be maintained at a high rate for the remainder of the filling process.

Future work should include pressure-composition isotherm (PCI) curves at a range of temperatures to fully investigate the effective thermal conductivity-composition relationship. The goal should be to develop a comprehensive data set such as that presented for a different metal hydride in Figure 2-5 in the work of Hahne and Kallweit. This data set would describe the Na-Al-H system over the full range of operating conditions. Gathering such a data set is extremely time-consuming and was not feasible in the current investigation. Furthermore, it is difficult to investigate the pressure dependence of the fully dehydrided state at elevated temperatures because the material in this state is prone to absorb hydrogen under pressure.

A final recommendation for future work is to investigate the effect of the addition of graphite powder to the Na-Al-H system. As demonstrated by the work of Wang [29], the addition of 10 wt% graphite powder improved the kinetic performance of the Na-Al-H system dramatically, especially at lower temperatures. This benefit was thought to be due to improved heat transfer between the solid metal hydride particles. The penalty is that the graphite reduces the overall storage capacity of the material. Graphite would theoretically enhance the effective thermal conductivity of the Na-Al-H system, as it did in the investigation by Griesinger [15] for a zeolite material. This benefit of graphite might make it a practical solution for sodium alanate, despite the decrease in system storage capacity.

Finally, it should be pointed out that this study could be applied to other metal hydrides that may present themselves as more promising candidates for solving the on-board hydrogen-storage problem. As with on-board reformation of hydrocarbon fuels, it may be decided by the community at-large that sodium alanate no longer has the potential to be a viable storage solution, especially since the targets for storage systems become more and more stringent in coming years. This does not mean this work is in vain, as the knowledge gained in studying the Na-Al-H system will undoubtedly help researchers understand the next candidate metal hydride to be investigated. The transient hot-wire technique remains a simple and valuable tool to study the effective thermal conductivity of metal hydrides and other similar materials.

With continued work, it is hoped the storage problem for fuel cell vehicles will ultimately be solved. Full-scale implementation of fuel cell vehicles with effective hydrogen storage will help end fossil fuel-dependence and bring a clean alternative to transportation.

BIBLIOGRAPHY

1. Ogden, J.M., *Prospects for Building a Hydrogen Energy Infrastructure.* Annual Review of Energy and the Environment, 1999. **24**: p. 227-279.
2. DOE, O.o.E.E.a.R.E. (2006) *FreedomCAR and Fuel Partnership Targets for On-Board Hydrogen Storage Systems*. http://www.eere.energy.gov/hydrogenandfuelcells/pdfs/freedomcar_targets_explanations.pdf
3. Pinkerton, F.E. and W.B. G., *Bottling the Hydrogen Genie.* The Industrial Physicist, 2004. **February/March**: p. 20-23.
4. GM, *GM Fuel Cell Vehicles*. 2005. http://www.gm.com/company/gmability/adv_tech/400_fcv/fact_sheets.html
5. Larminie, J. and A. Dicks, *Fuel Cell Systems Explained, 2nd ed.* 2003, Sussex, England: John Wiley and Sons.
6. Hahne, E. and J. Kallweit, *Thermal conductivity of metal hydride materials for storage of hydrogen: Experimental investigation.* International Journal of Hydrogen Energy, 1998. **23**(2): p. 107-114.
7. Cogan, R., *H2 Hybrid.* Green Car Journal Online, 2005.
8. Zaluski, L., A. Zaluska, and J.O. Strom-Olsen, *Hydrogenation properties of complex alkali metal hydrides fabricated by mechano-chemical synthesis.* Journal of Alloys and Compounds, 1999. **290**(1-2): p. 71-78.
9. Anton, D.L., S.M. Opalka, and D.A. Moser, *High Density Hydrogen Storage System Demonstration Using NaAlH4 Based Complex Compound Hydrides.* DOE FY 2003 Progress Report, 2003.
10. *Wikipedia public encyclopedia*. 2006. http://en.wikipedia.org/wiki/Knudsen_number
11. Ishido, Y., M. Kawamura, and S. Ono, *Thermal conductivity of magnesium-nickel hydride powder beds in a hydrogen atmosphere.* International Journal of Hydrogen Energy, 1982. **7**(2): p. 173-182.
12. Dedrick, D.E., et al., *Thermal properties characterization of sodium alanates.* Journal of Alloys and Compounds, 2005. **389**(1-2): p. 299-305.
13. Bogdanovic, B. and M. Schwickardi, *Ti-doped alkali metal aluminium hydrides as potential novel reversible hydrogen storage materials.* Journal of Alloys and Compounds, 1997. **253**: p. 1-9.
14. Liu, Z.Y., et al., *Fast simple and accurate measurement of zeolite thermal conductivity.* Zeolites, 1990. **10**(6): p. 565-570.
15. Griesinger, A., K. Spindler, and E. Hahne, *Measurements and theoretical modelling of the effective thermal conductivity of zeolites.* International Journal of Heat and Mass Transfer, 1999. **42**(23): p. 4363-4374.
16. Pons, M., P. Dantzer, and J.J. Guilleminot, *A measurement technique and a new model for the wall heat transfer coefficient of a packed bed of (reactive) powder without gas flow.* International Journal of Heat and Mass Transfer, 1993. **36**(10): p. 2635-2646.
17. Krishpersad Manohar, D.W.Y., James R. Booth, *Measurement of Apparent Thermal Conductivity by the Thermal Probe Method.* Journal of Testing and Evaluation, 2000. **28**(5): p. 345-351.

18. Huot, J., et al., *Synthesis of Na3AlH6 and Na2LiAlH6 by mechanical alloying.* Journal of Alloys and Compounds, 1999. **283**(1-2): p. 304-306.
19. Jensen, C.M., et al., *Advanced titanium doping of sodium aluminum hydride: segue to a practical hydrogen storage material?* International Journal of Hydrogen Energy, 1999. **24**(5): p. 461-465.
20. Zidan, R.A., et al., *Hydrogen cycling behavior of zirconium and titanium-zirconium-doped sodium aluminum hydride.* Journal of Alloys and Compounds, 1999. **285**(1-2): p. 119-122.
21. Gross, K.J., et al., *In-situ X-ray diffraction study of the decomposition of NaAlH4.* Journal of Alloys and Compounds, 2000. **297**(1-2): p. 270-281.
22. Bogdanovic, B., et al., *Investigation of hydrogen discharging and recharging processes of Ti-doped NaAlH4 by X-ray diffraction analysis (XRD) and solid-state NMR spectroscopy.* Journal of Alloys and Compounds, 2003. **350**(1-2): p. 246-255.
23. Bogdanovic, B., et al., *Metal-doped sodium aluminium hydrides as potential new hydrogen storage materials.* Journal of Alloys and Compounds, 2000. **302**(1-2): p. 36-58.
24. Jensen, C.M. and K.J. Gross, *Development of catalytically enhanced sodium aluminum hydride as a hydrogen-storage material.* Applied Physics a-Materials Science & Processing, 2001. **72**(2): p. 213-219.
25. Gross, K.J., G. Sandrock, and G.J. Thomas, *Dynamic in situ X-ray diffraction of catalyzed alanates.* Journal of Alloys and Compounds, 2002. **330**: p. 691-695.
26. Gross, K.J., G.J. Thomas, and C.M. Jensen, *Catalyzed alanates for hydrogen storage.* Journal of Alloys and Compounds, 2002. **330**: p. 683-690.
27. Fichtner, M., et al., *Small Ti clusters for catalysis of hydrogen exchange in NaAlH4.* Nanotechnology, 2003. **14**(7): p. 778-785.
28. Bogdanovic, B., cacute, and M.F.S.K.A.P.K.S.F. Schüth, *Improved Hydrogen Storage Properties of Ti-Doped Sodium Alanate Using Titanium Nanoparticles as Doping Agents.* Advanced Materials, 2003. **15**(12): p. 1012-1015.
29. Wang, J., et al., *Effect of graphite as a co-dopant on the dehydrogenation and hydrogenation kinetics of Ti-doped sodium aluminum hydride.* Journal of Alloys and Compounds, 2005. **395**(1-2): p. 252-262.
30. Suda, S., et al., *Experimental measurements of thermal conductivity.* Journal of the Less Common Metals, 1980. **74**(1): p. 127-136.
31. Suissa, E., I. Jacob, and Z. Hadari, *Experimental measurements and general conclusions on the effective thermal conductivity of powdered metal hydrides.* Journal of the Less Common Metals, 1984. **104**(2): p. 287-295.
32. International, A., *Standard Test Method for Thermal Conductivity of Refractories by Hot Wire (Platinum Resistance Thermometer Technique).* ASTM C 1113, 1999. **C 1113**: p. 216-220.
33. International, A., *Standard Test Method for Determination of Thermal Conductivity of Soil and Soft Rock by Thermal Needle Probe Procedure.* ASTM D 5334, 2000. **D 5334**: p. 1226-1230.
34. Luo, W. and E. Ronnebro, *Towards a viable hydrogen storage system for transportation application.* Journal of Alloys and Compounds, 2005. **404-406**: p. 392-395.

35. Zaluska, A. and L. Zaluski, *New catalytic complexes for metal hydride systems.* Journal of Alloys and Compounds, 2005. **404-406**: p. 706-711.
36. Mamatha, M., et al., *Mechanochemical preparation and investigation of properties of magnesium, calcium and lithium-magnesium alanates.* Journal of Alloys and Compounds, 2005. **407**(1-2): p. 78-86.
37. Carslaw and Jaeger, *Conduction of Heat in Solids*. 1959.
38. Figliola, R.S. and D.E. Beasley, *Theory and Design for Mechanical Measurements, Third Edition*. Measurement Science and Technology. Vol. 12. 2001: Wiley. 1743.

APPENDIX A – FINITE ELEMENT CODE

A-1 Finite element code "k_eff_model."

```
function [t_eval,L0,Tmax,q0] = k_eff_model(k,d,l)
% Written by Michael Christopher, 2005
% FEMLAB Code Generated by FEMLAB 3.1 (FEMLAB 3.1.0.157)
% ============================================================== %
% This code defines and solves a transient finite element model
% representing a cylinder with a centrally-located line heat source.
% The inputs are:
%
%    k - Thermal conductivity (W/mK)
%    d - Diameter of cylinder (cm)
%    l - Length of cylinder (cm)
%
% The model outputs an array of temperatures values covering the
% spatial and time dimensions of the model.  This code outputs the
% following values:
%
%    t_eval - Twice the length of time it takes for the influence of
%             heat to reach the outer boundary.
%    L0 - Undisturbed length, calculated at t_eval.
%    Tmax - Maximum temperature at the wire.
%    q0 - Heat input required for Tmax = T0 + 3.

% Definition of constants
q0 = 20000;                % W/m2
T0 = 300;
Tmax = T0 + 4;

% Iterate model until Tmax criteria is reached.
while Tmax-T0 >= 3.01
    t_solve = 3000;          % s
    dt = 1;                  % s
    r1 = d/200-0.00025;      % m
    l1 = l/100;              % m

    flclear fem

    % Femlab version
    clear vrsn
    vrsn.name = 'FEMLAB 3.1';
    vrsn.ext = '';
    vrsn.major = 0;
    vrsn.build = 157;
    vrsn.rcs = '$Name:  $';
    vrsn.date = '$Date: 2004/11/12 07:39:54 $';
    fem.version = vrsn;

    % Geometry
    g1=rect2(r1,l1,'base','corner','pos',{'0.00025','0'},'rot','0');
    clear s
    s.objs={g1};
    s.name={'CO1'};
```

```
s.tags={'g1'};

fem.draw=struct('s',s);
fem.geom=geomcsg(fem);

% Initialize mesh
fem.mesh=meshinit(fem);

% Create Poisson mesh
fem.mesh=meshpoi(fem,floor(d/l*50),200);


% Application mode 1
clear appl
appl.mode.class = 'HeatTransfer';
appl.mode.type = 'axi';
appl.assignsuffix = '_ht';
clear bnd
bnd.q0 = {0,q0};
bnd.T0 = {T0,0};
bnd.type = {'T','q'};
bnd.ind = [2,1,1,1];
appl.bnd = bnd;
clear equ
equ.init = T0;
equ.k = k;
equ.rho = 1240;
equ.C = 1583;
equ.ind = [1];
appl.equ = equ;
fem.appl{1} = appl;
fem.sdim = {'r','z'};
fem.border = 1;
fem.outform = 'general';

% Multiphysics
fem=multiphysics(fem);

% Extend mesh
fem.xmesh=meshextend(fem);

% Solve problem
fem.sol=femtime(fem, ...
                'solcomp',{'T'}, ...
                'outcomp',{'T'}, ...
                'tlist',[0:1:t_solve], ...
                'tout','tlist');

% Find end time based on outer boundary influence
[H1,T_wall_RAW]=postcrossplot(fem,0,[r1;l/200], ...
          'outtype','postdata', ...
          'pointdata','T', ...
          'linstyle','-', ...
          'title','Time History r = 0.25 mm', ...
          'axislabel',{'Time','Temperature'}, ...
```

```
                'geomnum',[1]);
    T_wall = sortrows(T_wall_RAW.p');
    i = 1;
    while T_wall(i,2) == T0
        i = i + 1;
    end
    t_eval = 2*(i)

    % Transient data at wire
    [H2,t_data]=postcrossplot(fem,0,[.00025;l1/2], ...
                'outtype','postdata', ...
                'pointdata','T', ...
                'linstyle','-', ...
                'title','Time History r = 0.25 mm', ...
                'axislabel',{'Time','Temperature'}, ...
                'geomnum',[1]);

    T_center = sortrows(t_data.p');

    % Find undisturbed length from wire z-profile at t_eval
    [H3,T_wire]=postcrossplot(fem,1,[1], ...
                'outtype','postdata', ...
                'lindata','T', ...
                'cont','internal', ...
                'linxdata','z', ...
                'linstyle','-', ...
                'solnum',t_eval);

    T_w = sortrows(T_wire.p');
    csvwrite('C:\FEM\Transient.csv',T_w);

    avg5 = (T_w(298,2)+T_w(299,2)+T_w(300,2)+T_w(301,2)+T_w(302,2))/5;
    bool = zeros(601,1);
    for j = 1:1:601
        if (T_w(j,2)-T0) > (avg5-T0)*.95
            bool(j,1) = 1;
        end
    end
    L0 = sum(bool)/601;
    Tmax_new = T_center(t_eval,2);
    q0_new = 3/(Tmax_new-T0)*q0;
    Tmax = Tmax_new;
    q0 = q0_new;
end
```

A-2 Finite element code "k_eff_transient."

```
function [T_transient] = k_eff_transient(k,d,l,t_eval,q0)
% Written by Michael Christopher, 2005
% FEMLAB Code Generated by FEMLAB 3.1 (FEMLAB 3.1.0.157)
% ============================================================== %
% This code defines and solves a transient finite element model
% representing a cylinder with a centrally-located line heat source.
% The inputs are:
%
%    k - Thermal conductivity (W/mK)
%    d - Diameter of cylinder (cm)
%    l - Length of cylinder (cm)
%    t_eval - Solved for in k_eff_model
%    q0 - Solved for in k_eff_model
%
% The model outputs an array of temperatures values covering the
% spatial and time dimensions of the model.  This code outputs an
% array of temperature values over the time domain of the solution.


% Definition of constants
    T0 = 300;
    t_solve = t_eval;       % s
    dt = 1;                 % s
    r1 = d/200-0.00025;     % m
    l1 = l/100;             % m

    flclear fem

    % Femlab version
    clear vrsn
    vrsn.name = 'FEMLAB 3.1';
    vrsn.ext = '';
    vrsn.major = 0;
    vrsn.build = 157;
    vrsn.rcs = '$Name:  $';
    vrsn.date = '$Date: 2004/11/12 07:39:54 $';
    fem.version = vrsn;

    % Geometry
    g1=rect2(r1,l1,'base','corner','pos',{'0.00025','0'},'rot','0');
    clear s
    s.objs={g1};
    s.name={'CO1'};
    s.tags={'g1'};

    fem.draw=struct('s',s);
    fem.geom=geomcsg(fem);

    % Initialize mesh
    fem.mesh=meshinit(fem);

    % Create Poisson mesh
    fem.mesh=meshpoi(fem,floor(d/l*50),200);
```

```
% Application mode 1
clear appl
appl.mode.class = 'HeatTransfer';
appl.mode.type = 'axi';
appl.assignsuffix = '_ht';
clear bnd
bnd.q0 = {0,q0};
bnd.T0 = {T0,0};
bnd.type = {'T','q'};
bnd.ind = [2,1,1,1];
appl.bnd = bnd;
clear equ
equ.init = T0;
equ.k = k;
equ.rho = 1240;
equ.C = 1583;
equ.ind = [1];
appl.equ = equ;
fem.appl{1} = appl;
fem.sdim = {'r','z'};
fem.border = 1;
fem.outform = 'general';

% Multiphysics
fem=multiphysics(fem);

% Extend mesh
fem.xmesh=meshextend(fem);

% Solve problem
fem.sol=femtime(fem, ...
                'solcomp',{'T'}, ...
                'outcomp',{'T'}, ...
                'tlist',[0:1:t_solve], ...
                'tout','tlist');

% Transient data at wire
[H2,t_data]=postcrossplot(fem,0,[.00025;l1/2], ...
          'outtype','postdata', ...
          'pointdata','T', ...
          'linstyle','-', ...
          'title','Time History r = 0.25 mm', ...
          'geomnum',[1]);

T_transient = sortrows(t_data.p');
```

APPENDIX B – FINITE ELEMENT RESULTS

B-1 Results for $L/D = 6.67$, $dt = 1$ s

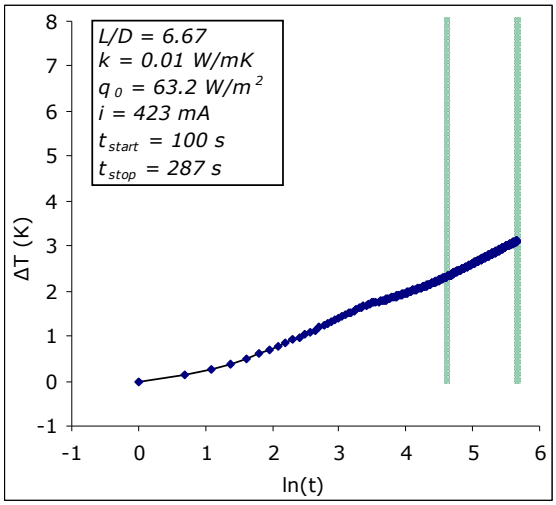

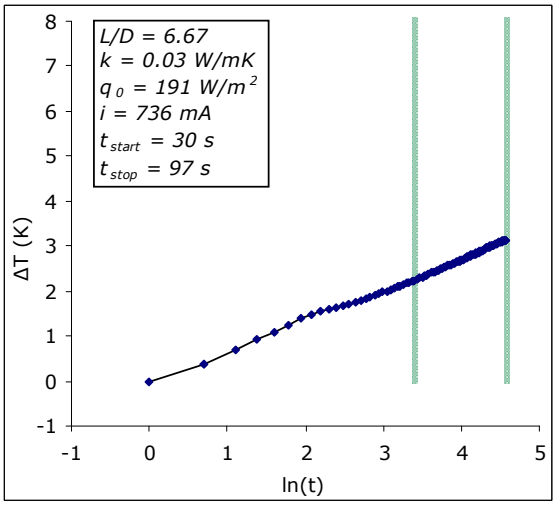

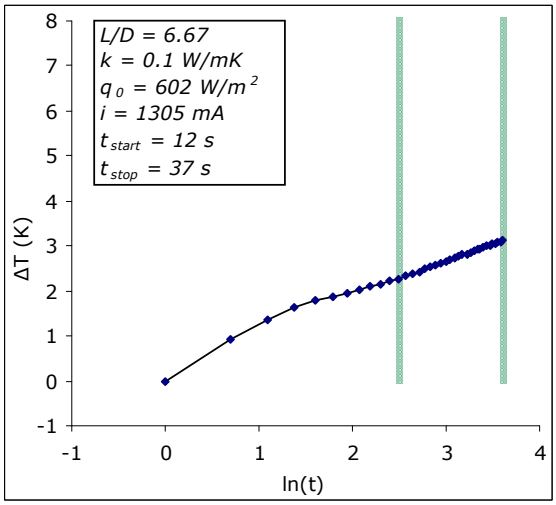

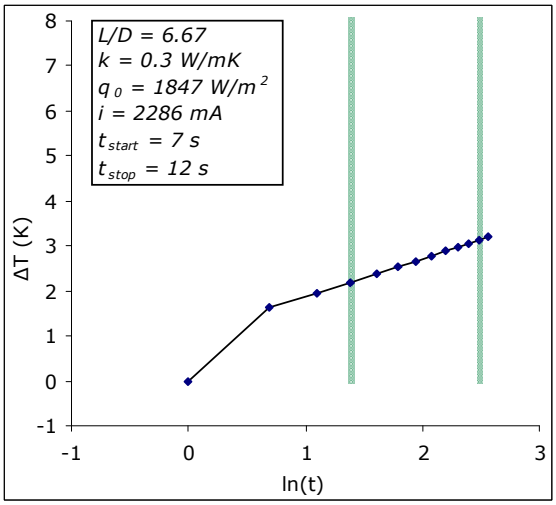

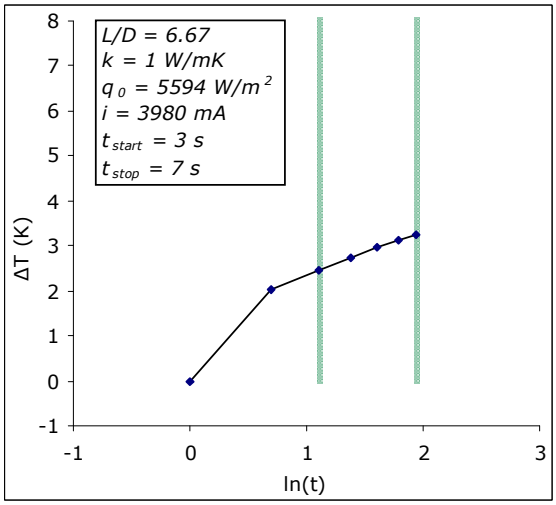

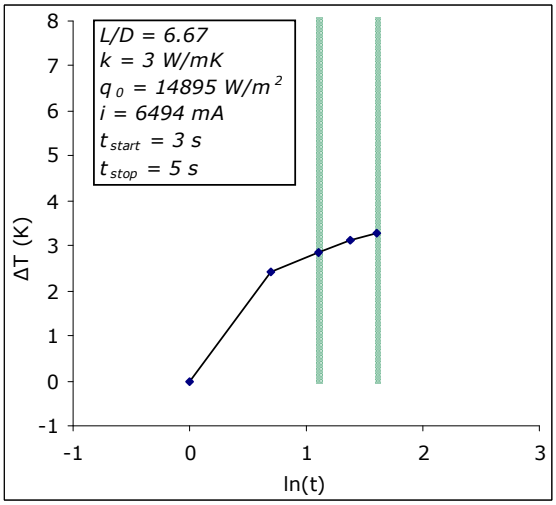

B-2 Results for $L/D = 5$, $dt = 1$ s

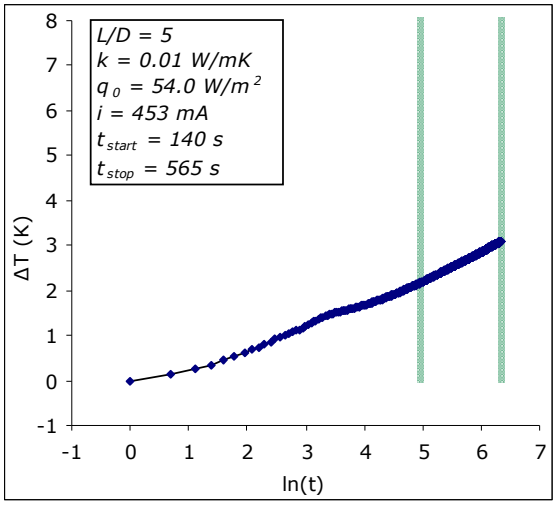

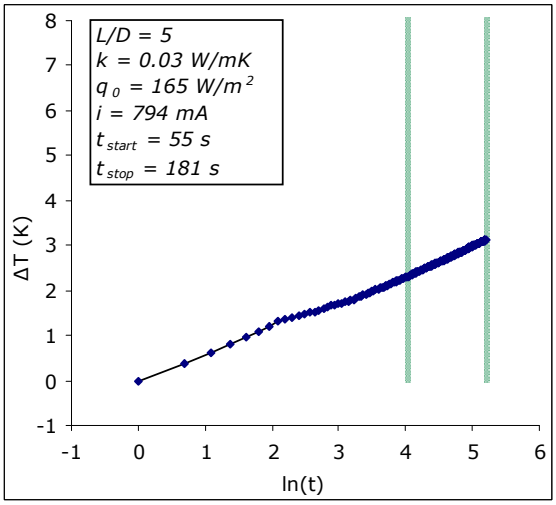

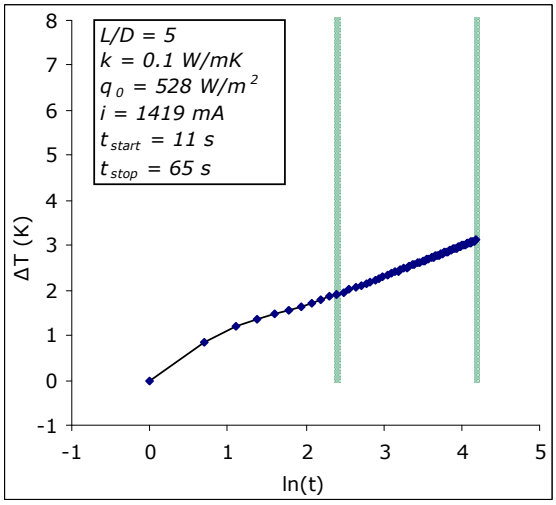

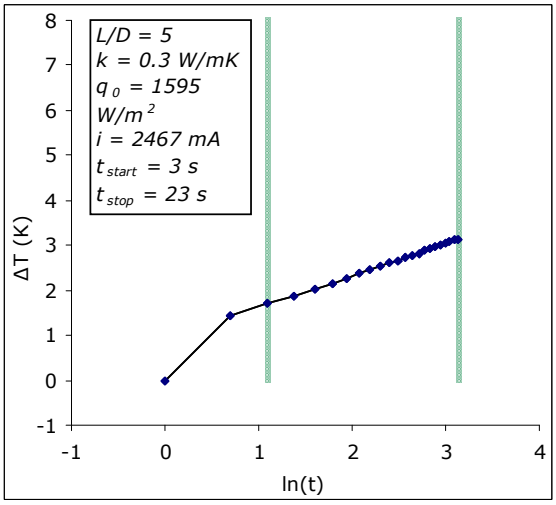

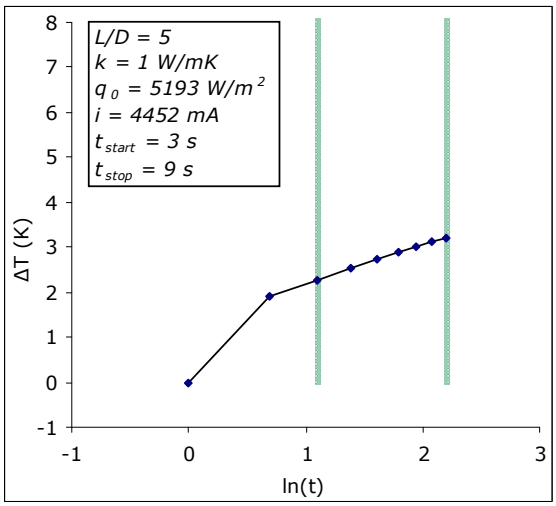

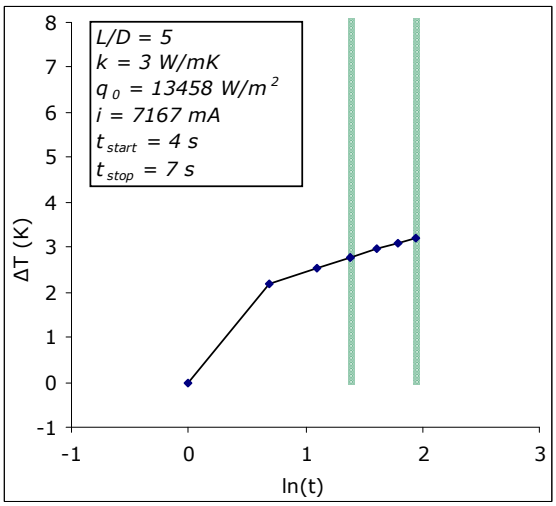

B-3 Results for $L/D = 4$, $dt = 1$ s

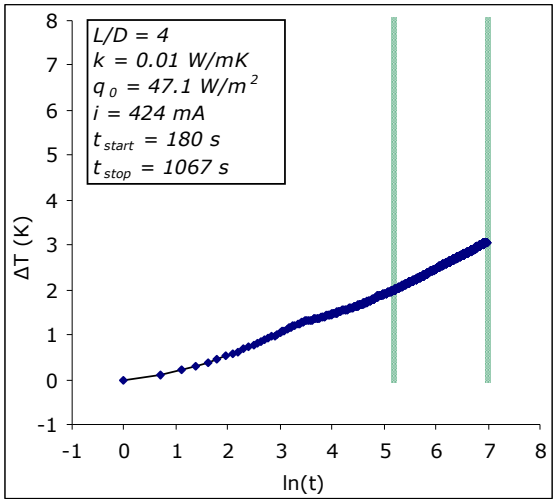

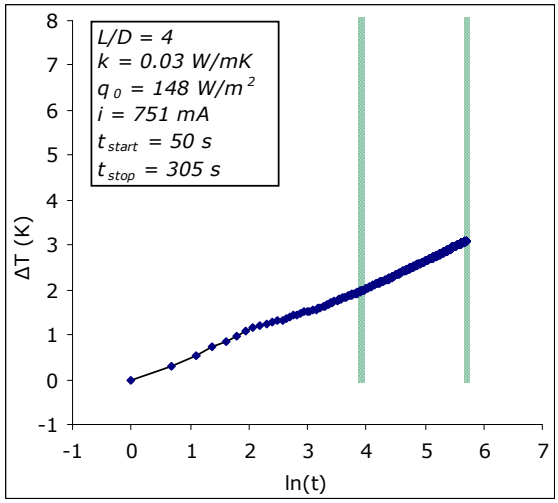

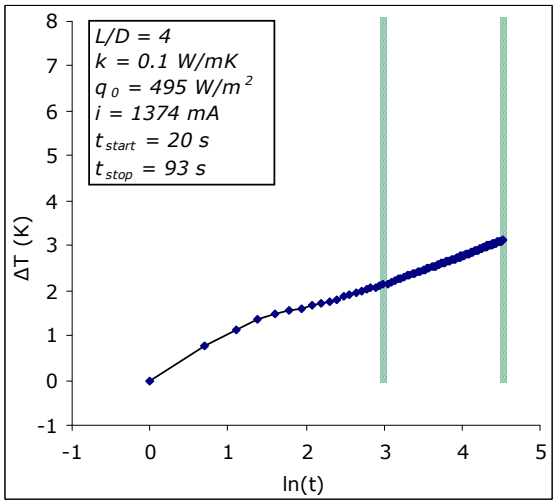

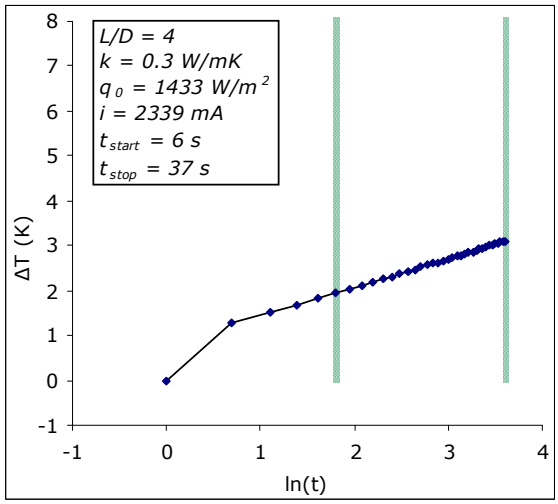

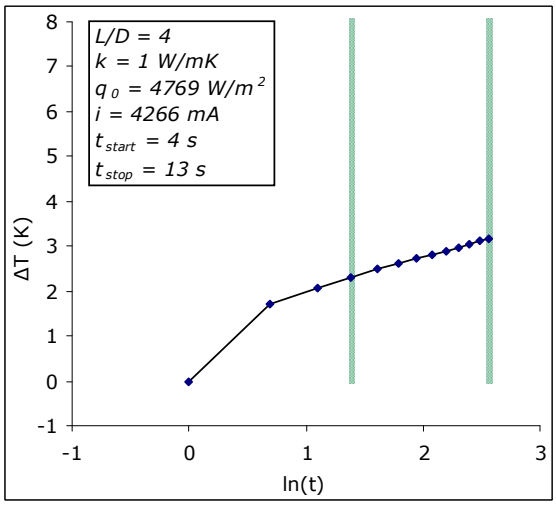

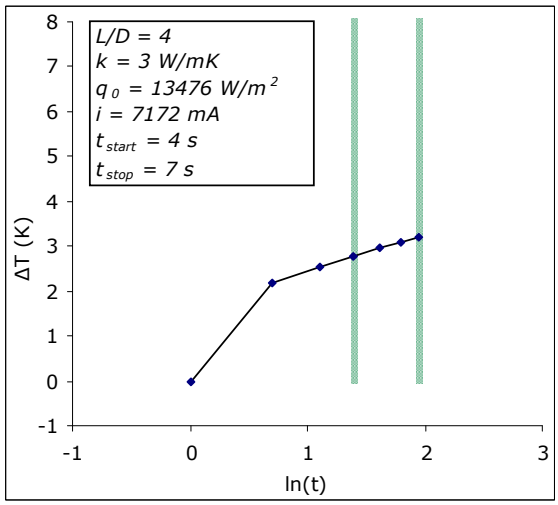

B-4 Results for $L/D = 3.33$, $dt = 1$ s

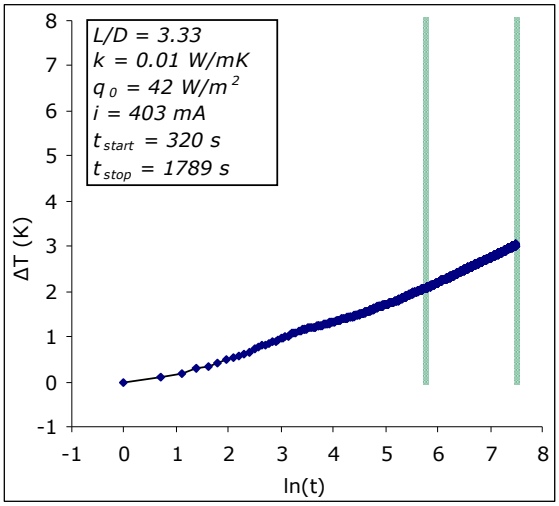

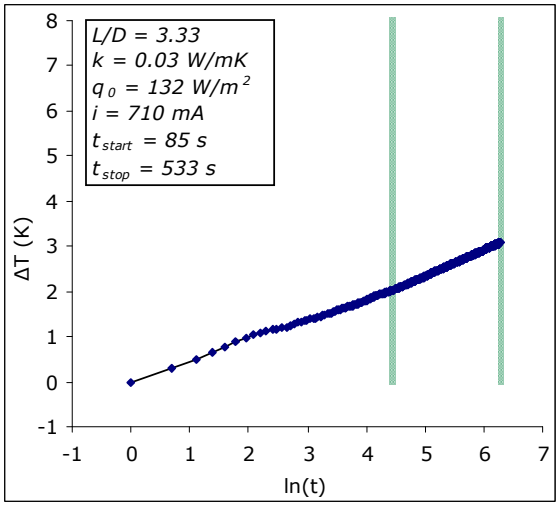

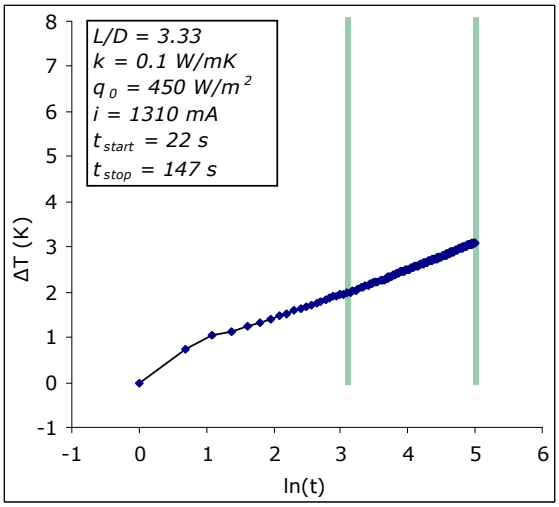

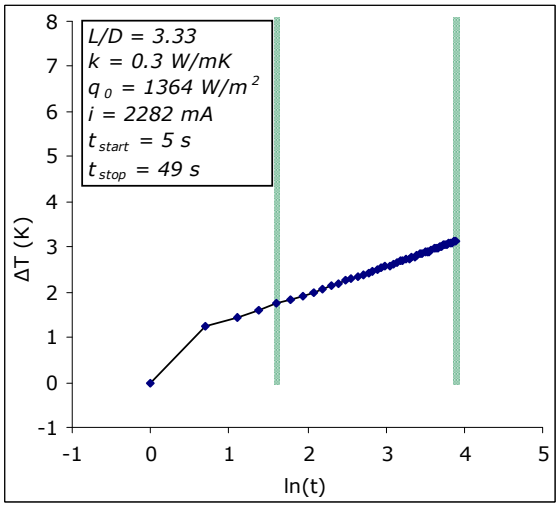

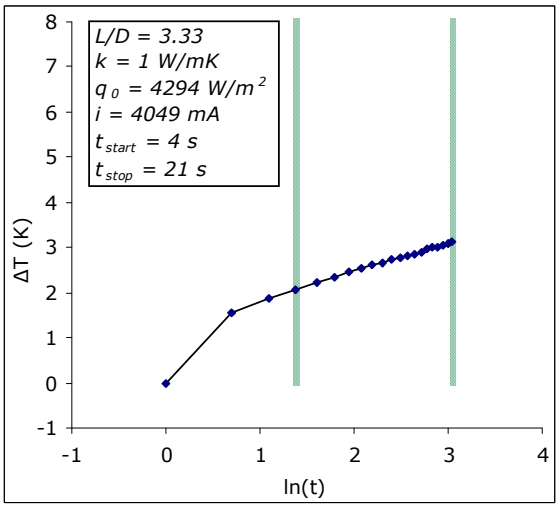

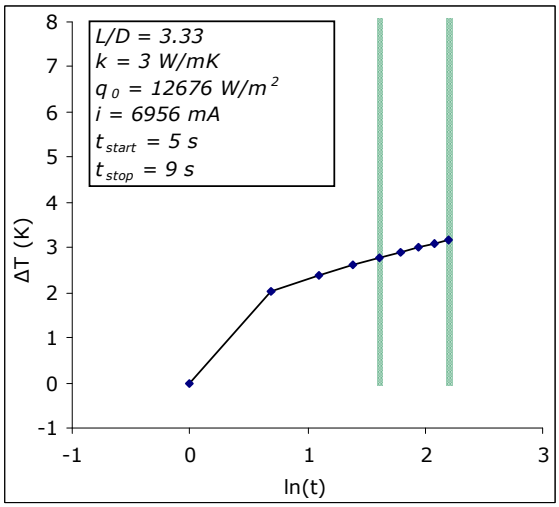

B-5 Results for L/D = 6.67, dt = 0.1 s

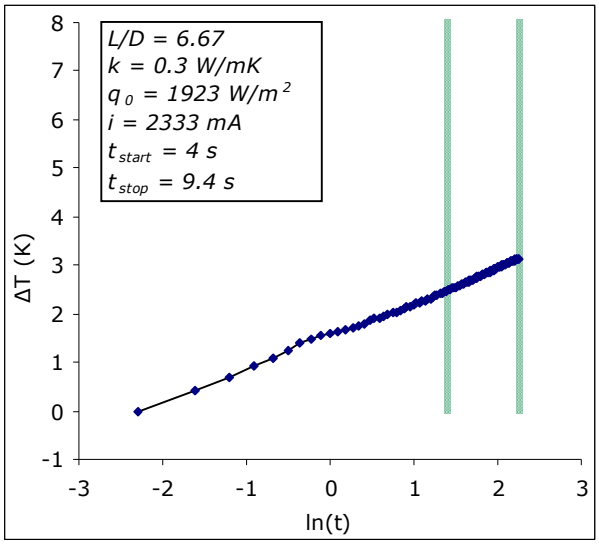

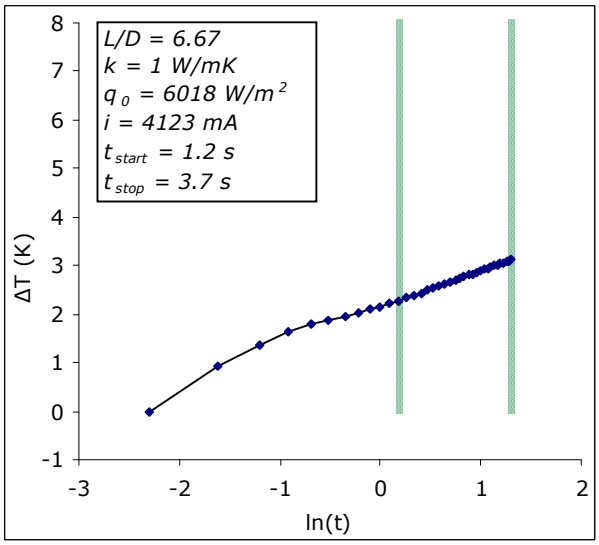

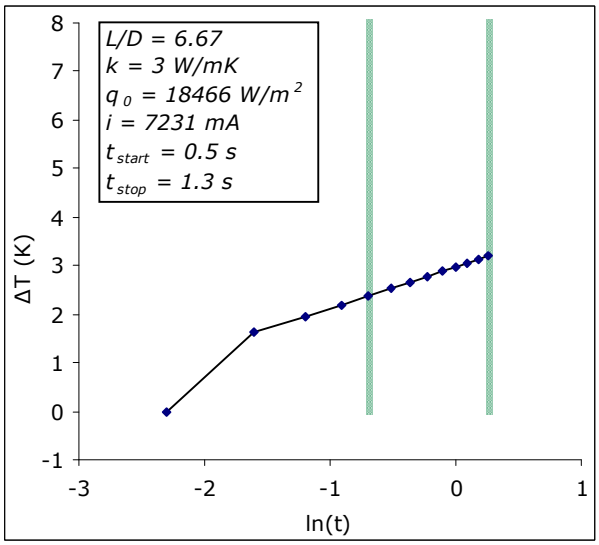

B-6 Results for $L/D = 5$, $dt = 0.1$ s

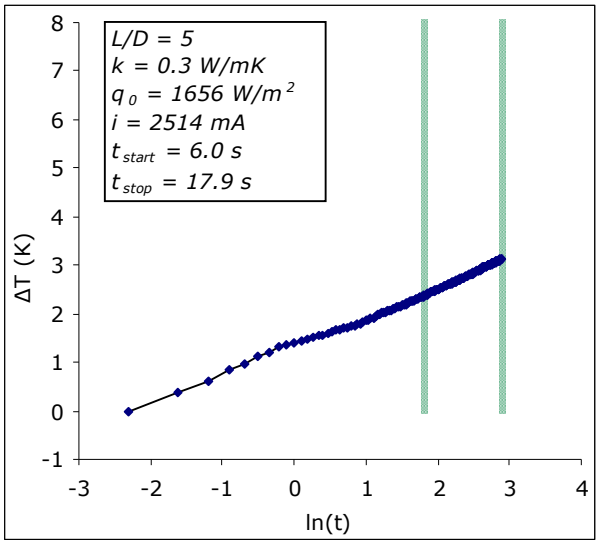

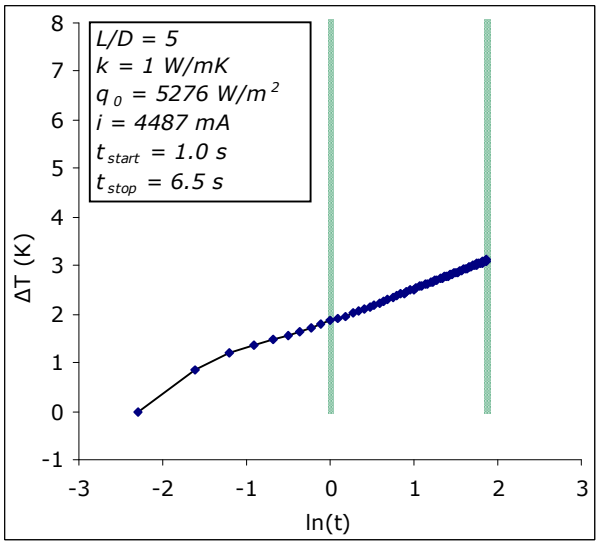

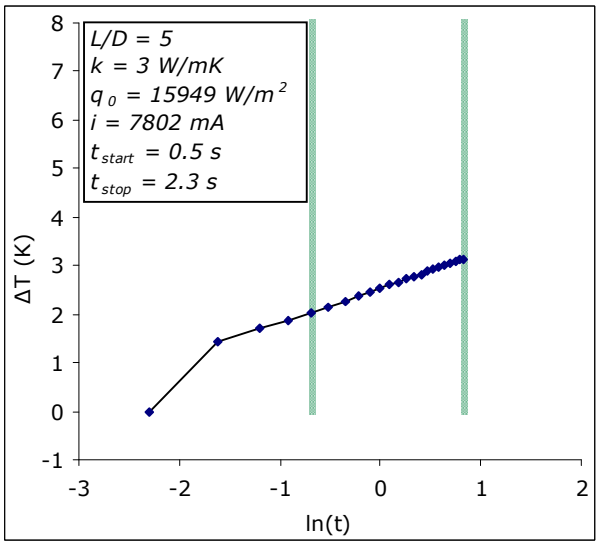

B-7 Results for $L/D = 4$, $dt = 0.1$ s

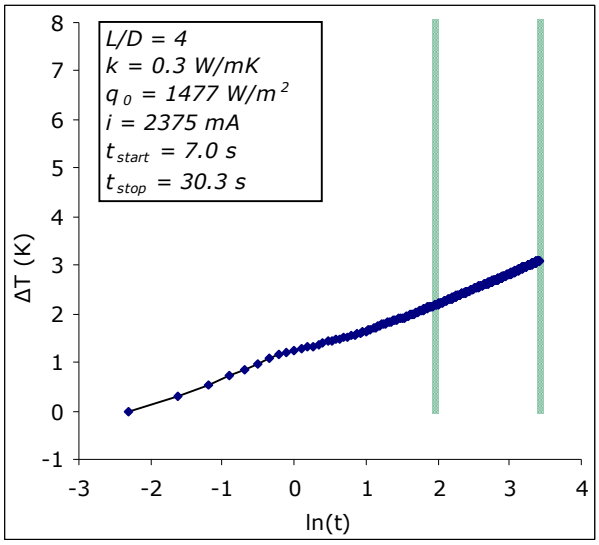

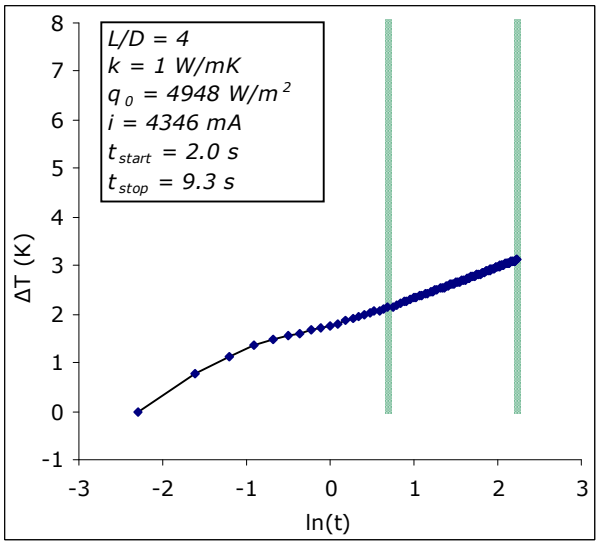

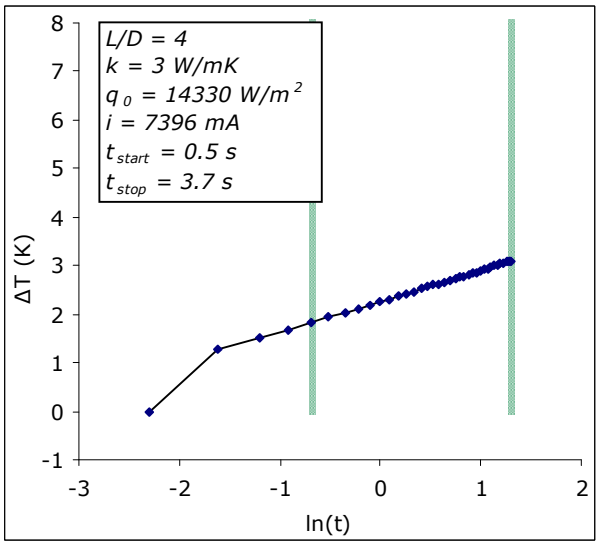

B-8 Results for L/D = 3.33, dt = 0.1 s

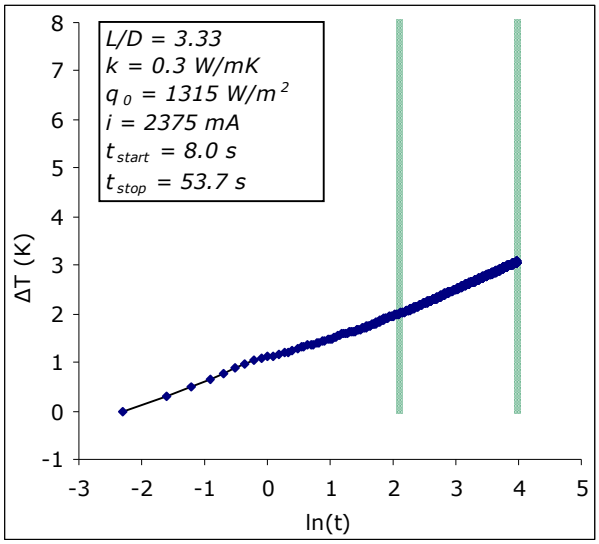

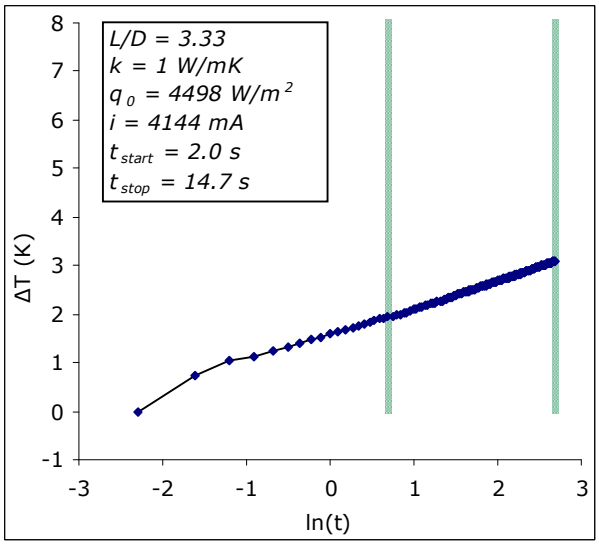

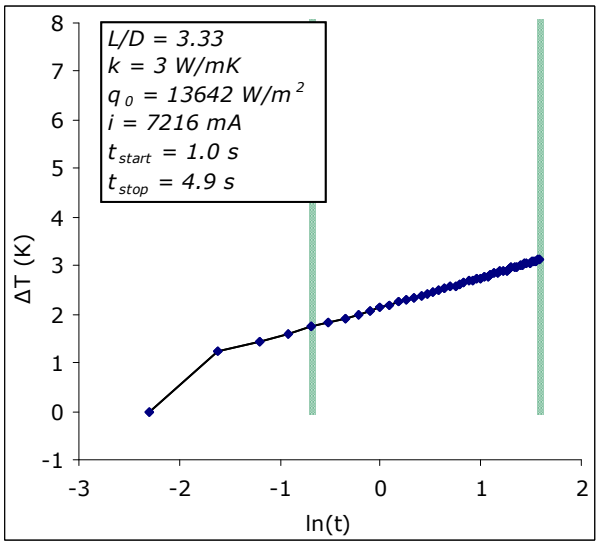

APPENDIX C – CALIBRATION DATA

C-1 Results of wire resistance calibration.

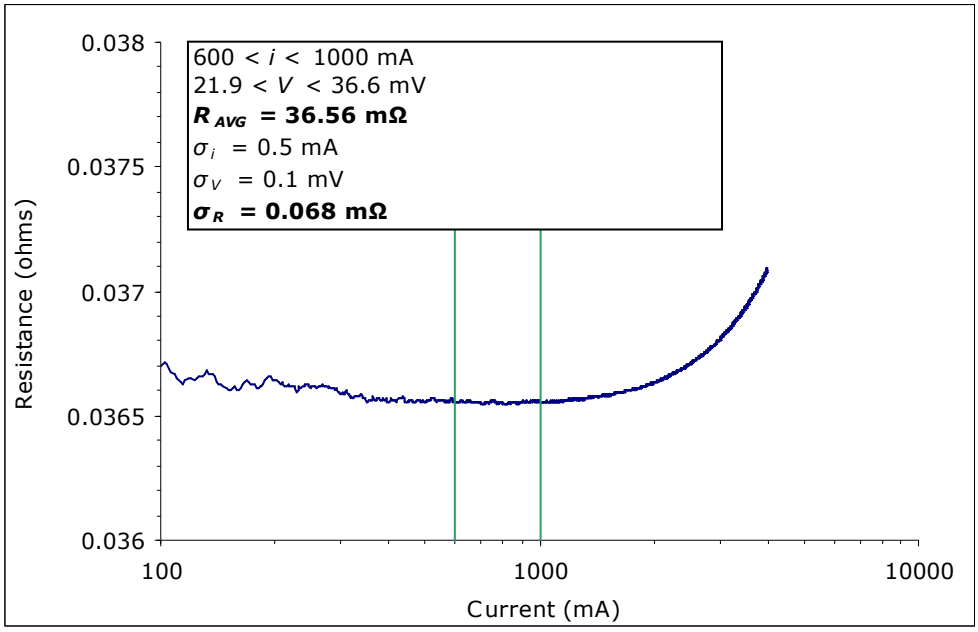

APPENDIX D – SAND INVESTIGATION RESULTS

D-1 First Repeatability Analysis (i = 2000 mA) (Measurements 1-6)

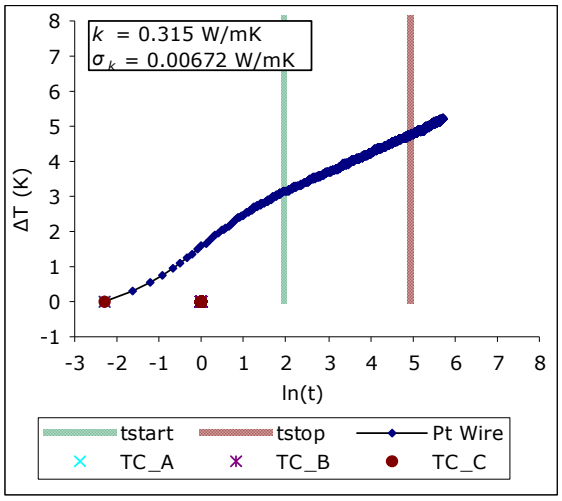

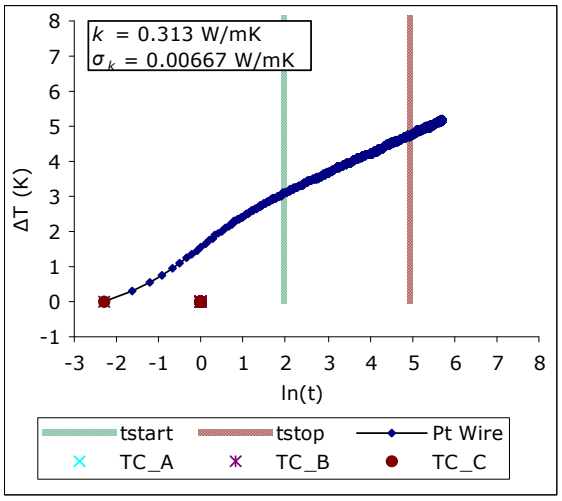

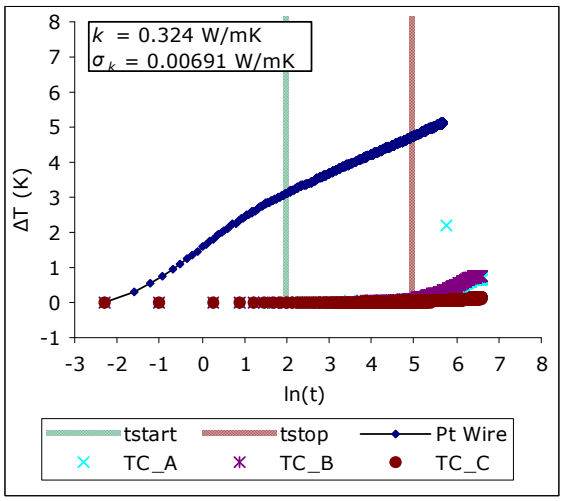

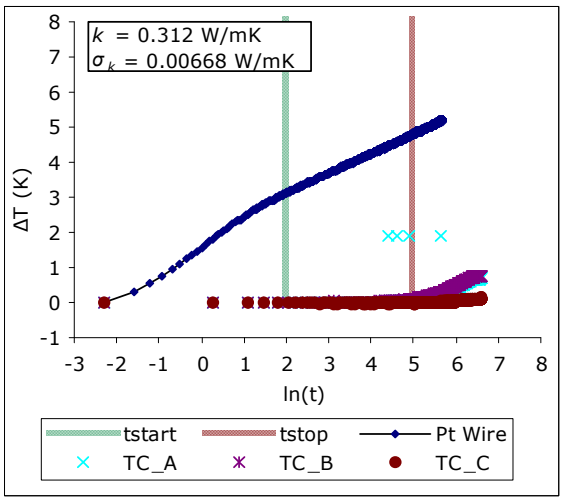

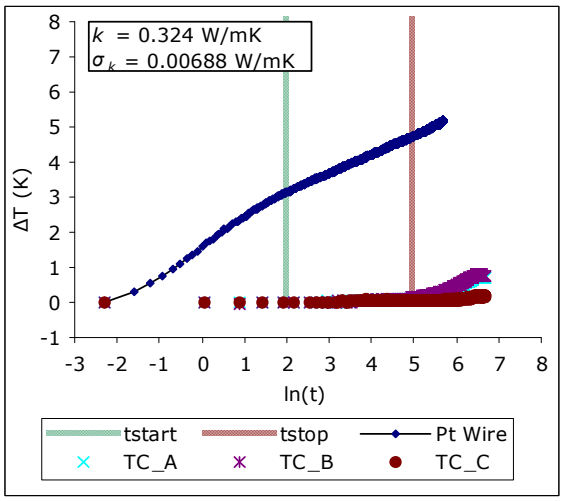

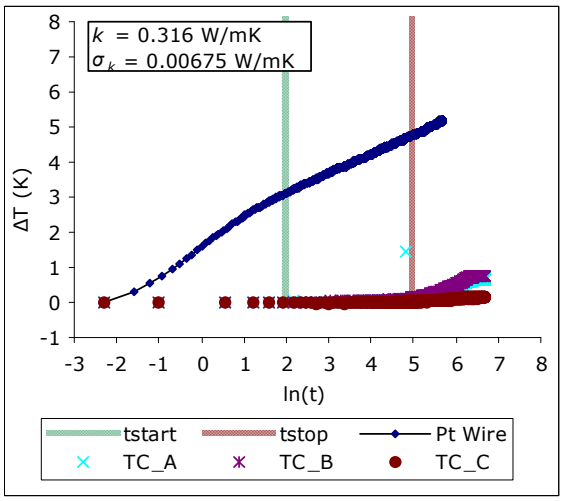

D-1 First Repeatability Analysis (i = 2000 mA) (Measurements 7-12)

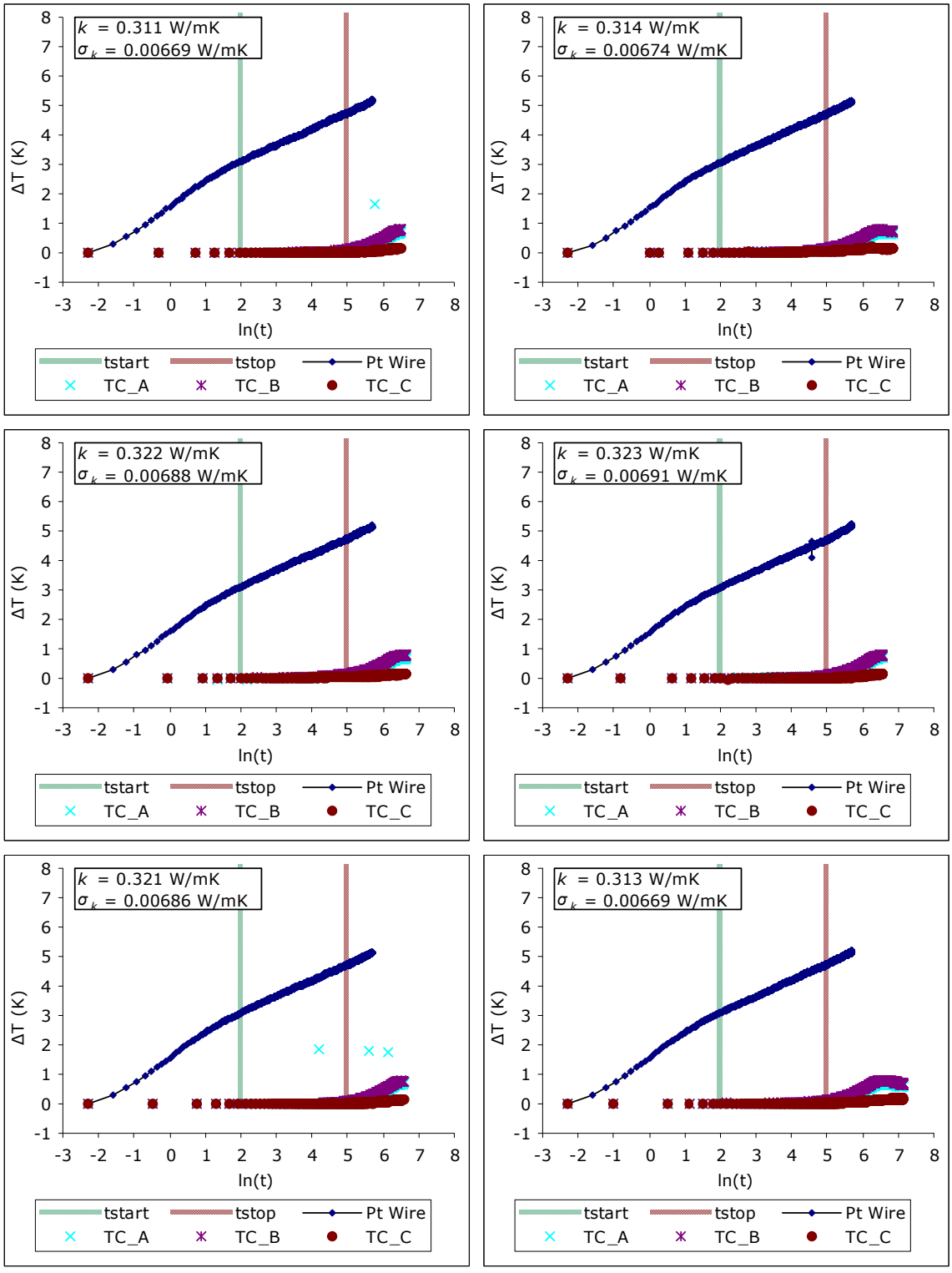

D-2 Second Repeatability Analysis (i = 1500 mA) (Measurements 1-6)

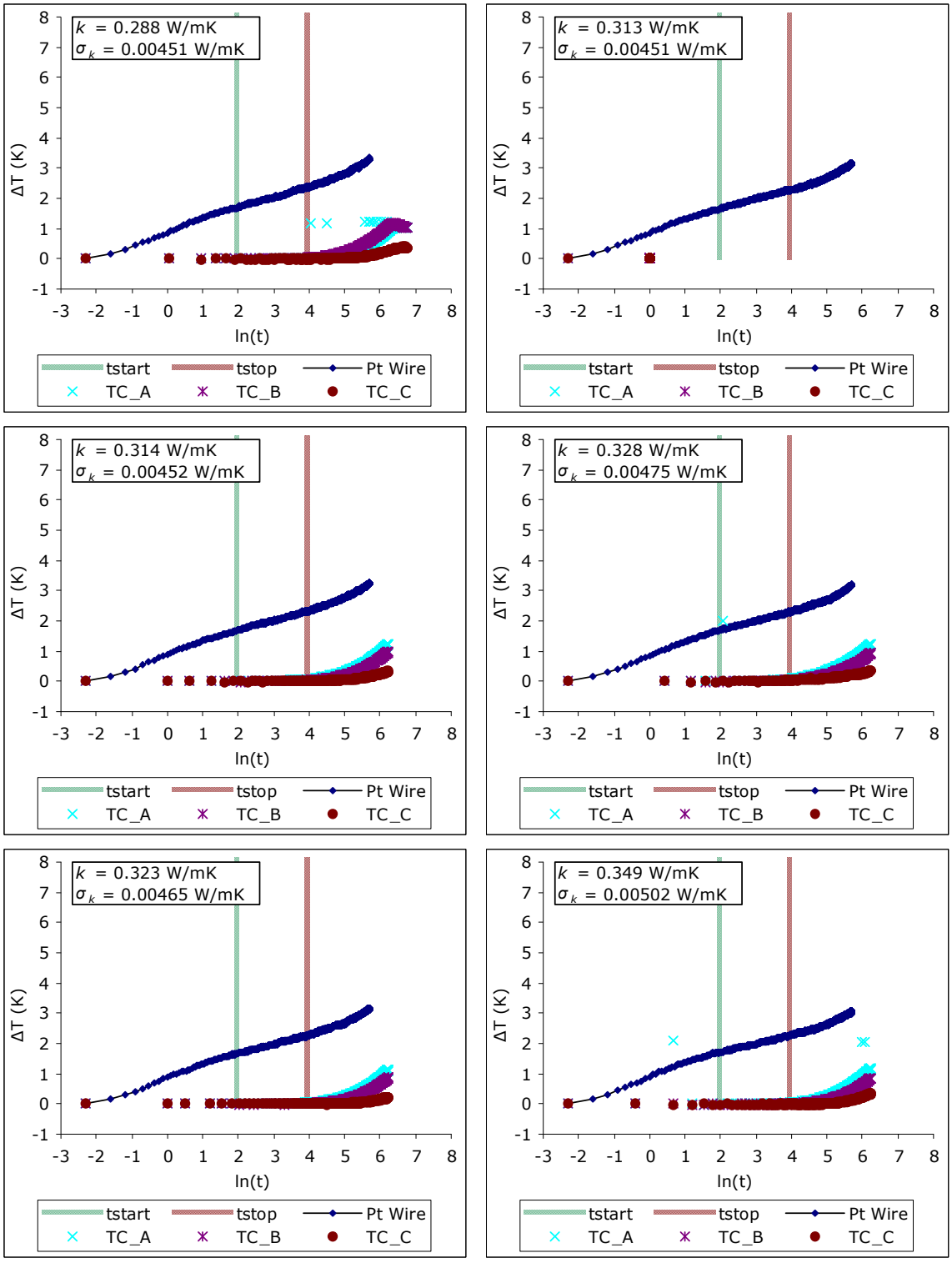

D-2 Second Repeatability Analysis (i = 1500 mA) (Measurements 7-12)

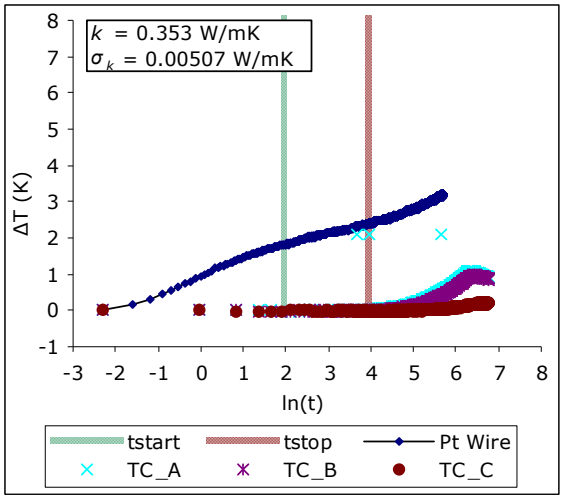

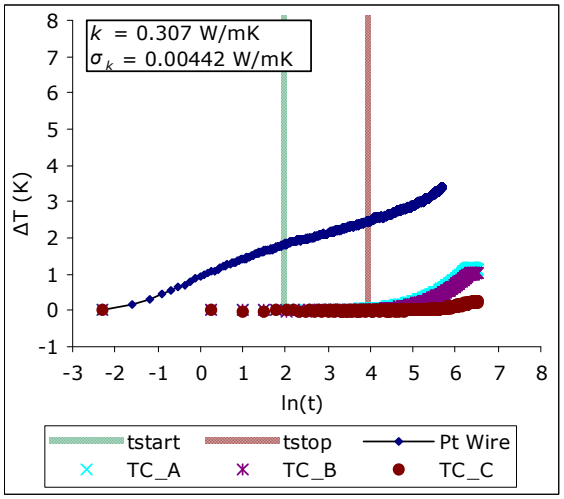

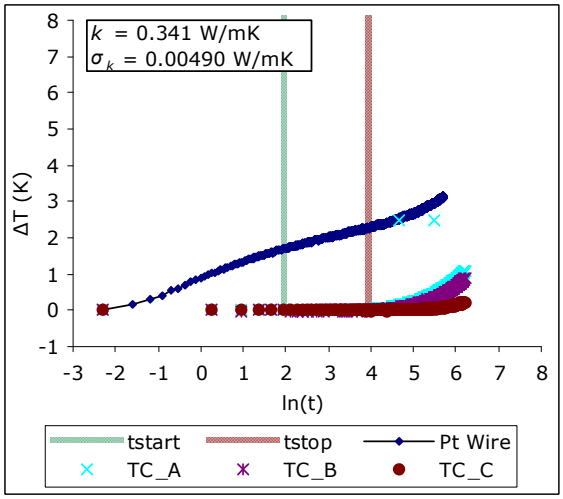

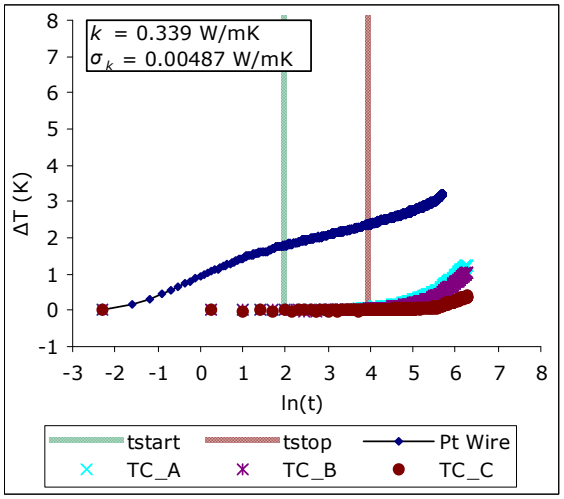

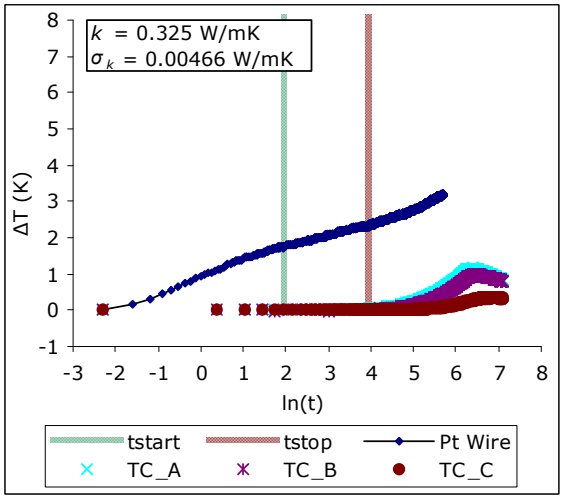

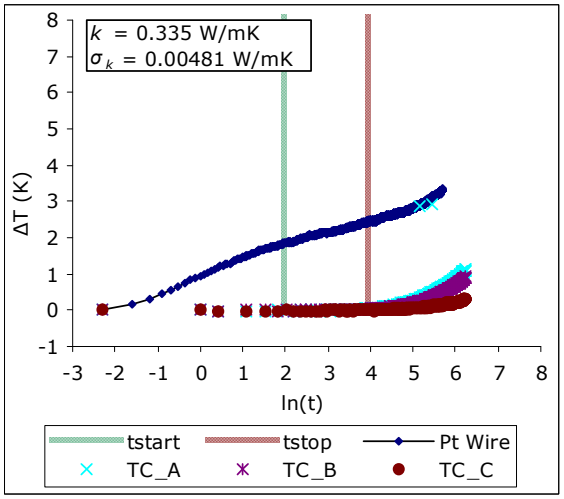

D-2 Second Repeatability Analysis (i = 2000 mA) (Measurements 1-6)

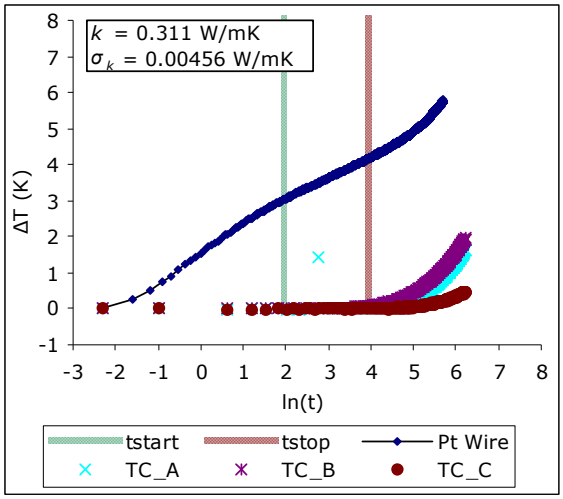

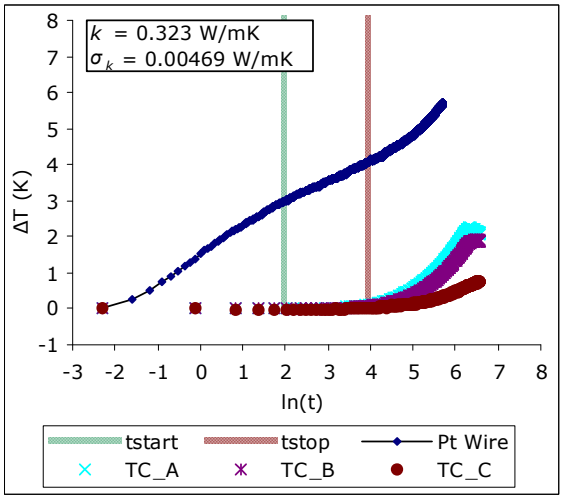

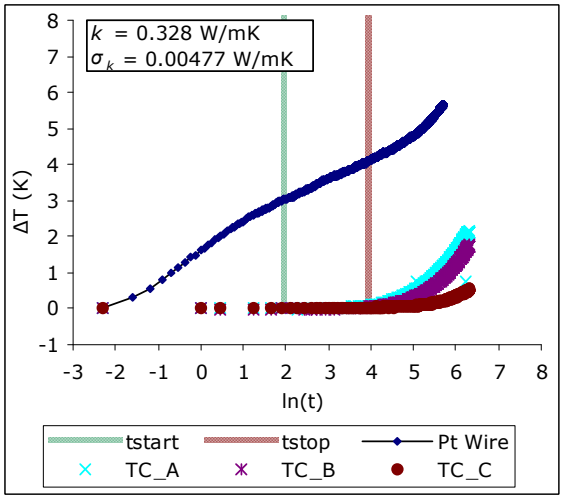

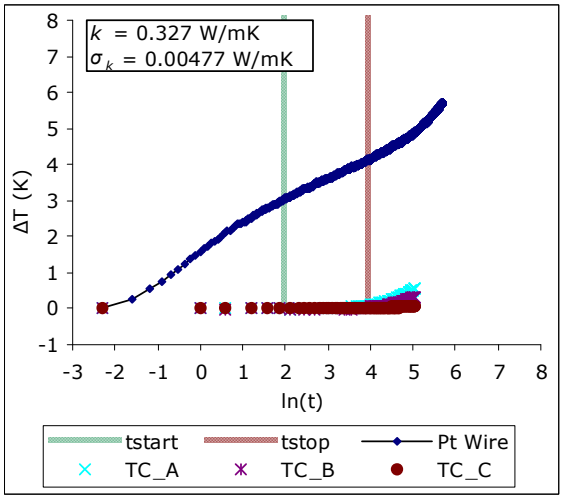

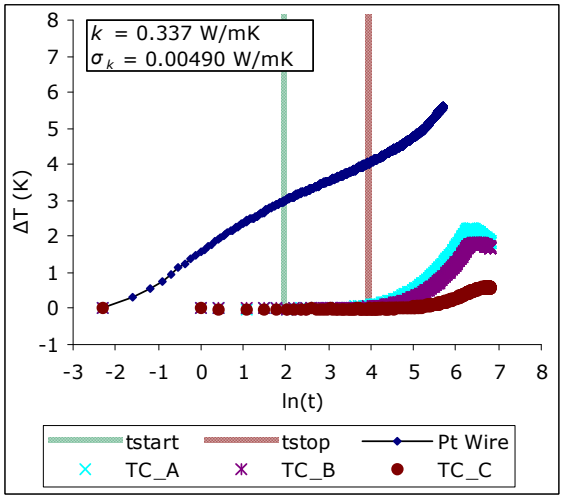

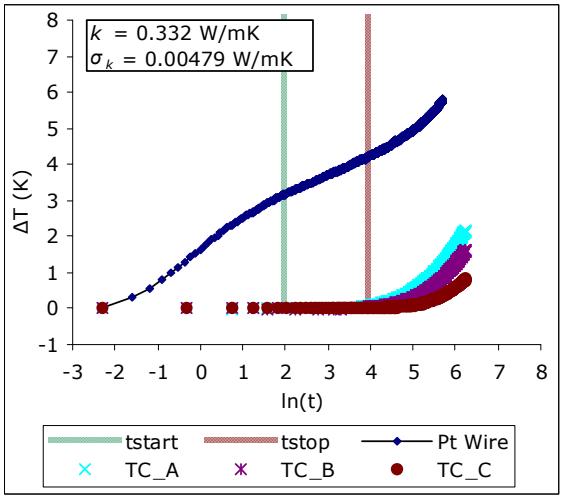

D-2 Second Repeatability Analysis (i = 2000 mA) (Measurements 7-12)

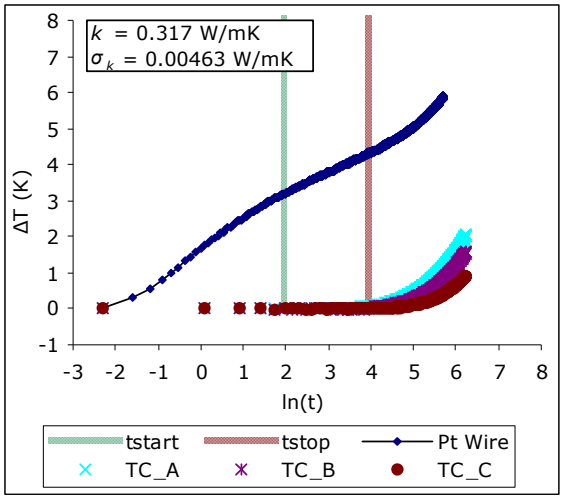

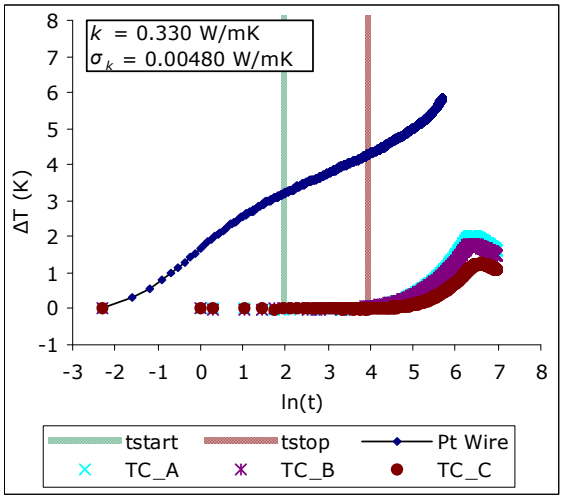

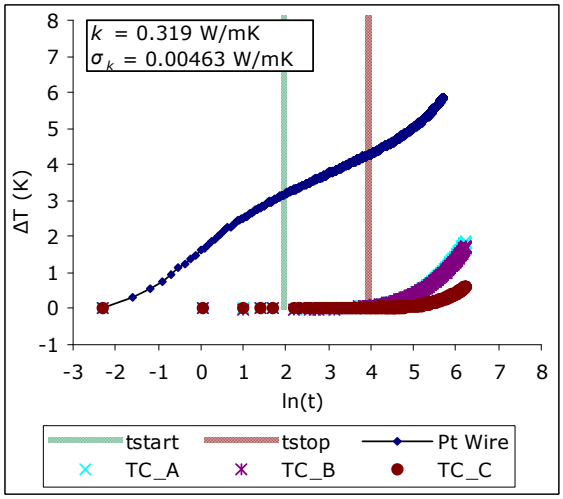

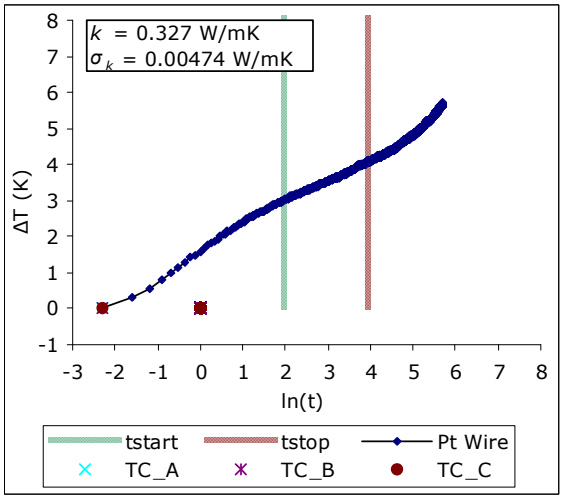

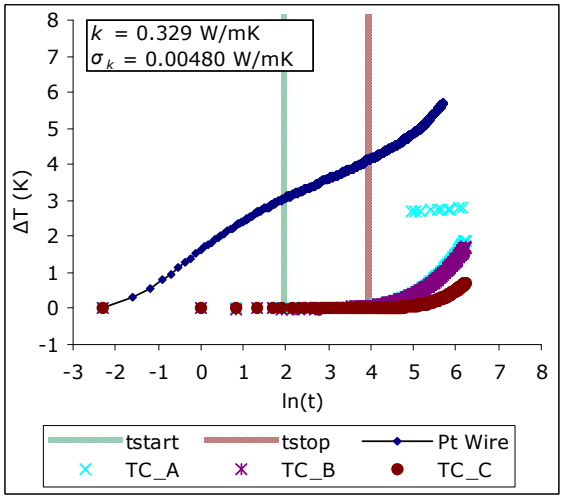

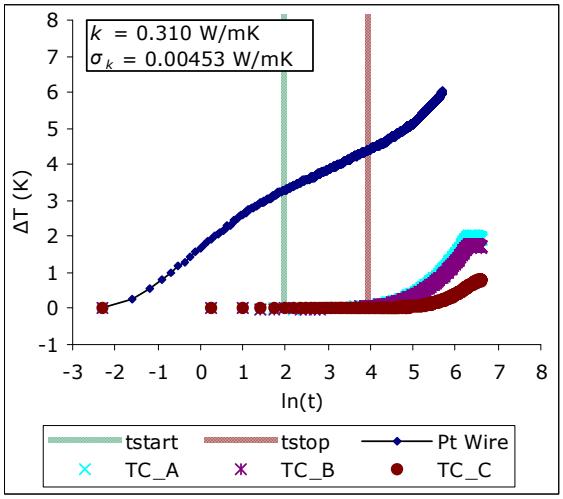

D-3 Pressure Investigation (i = 4000 mA) (Measurements 1-6)

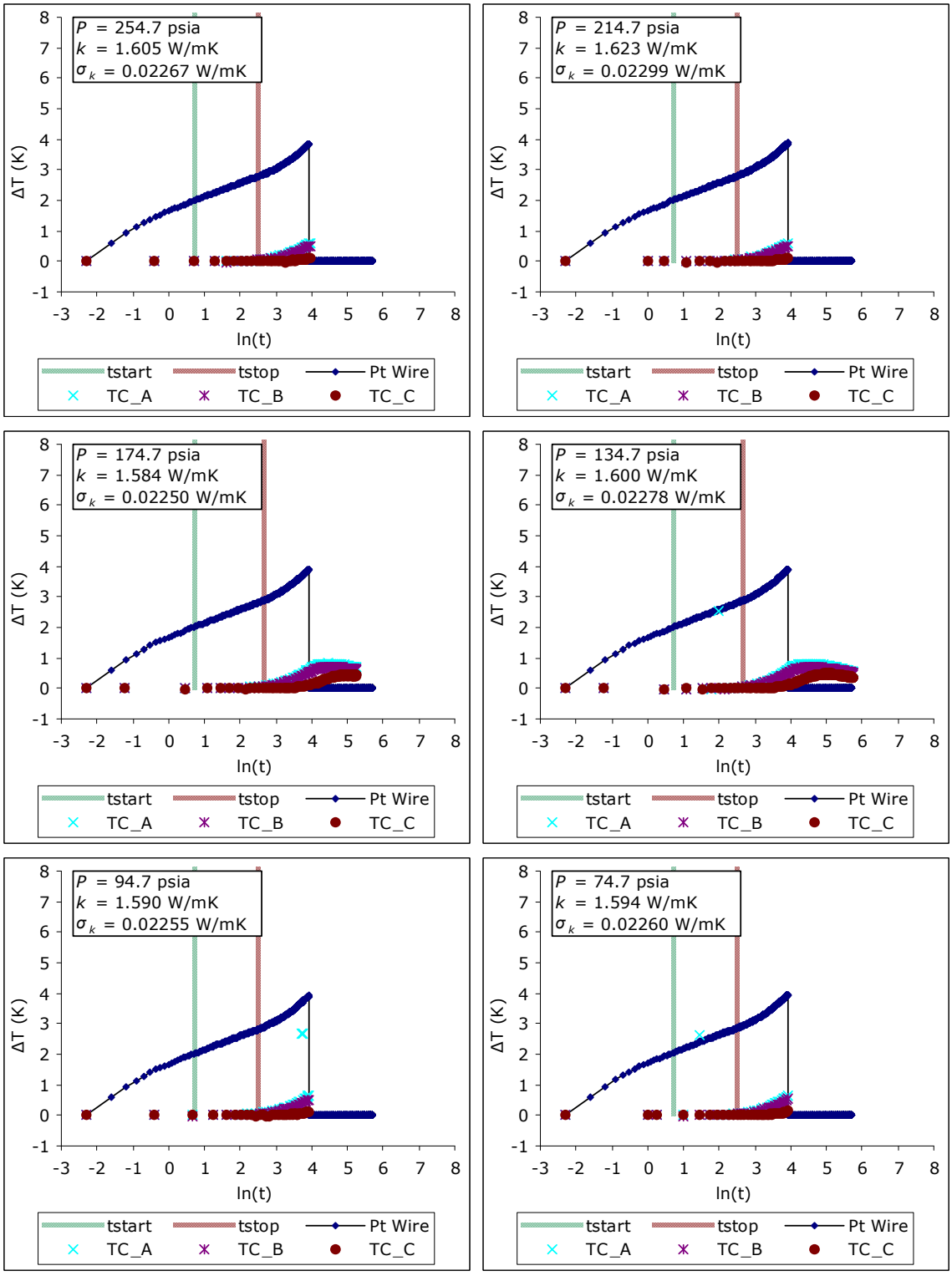

D-3 Pressure Investigation (i = 4000 mA) (Measurements 7-10)

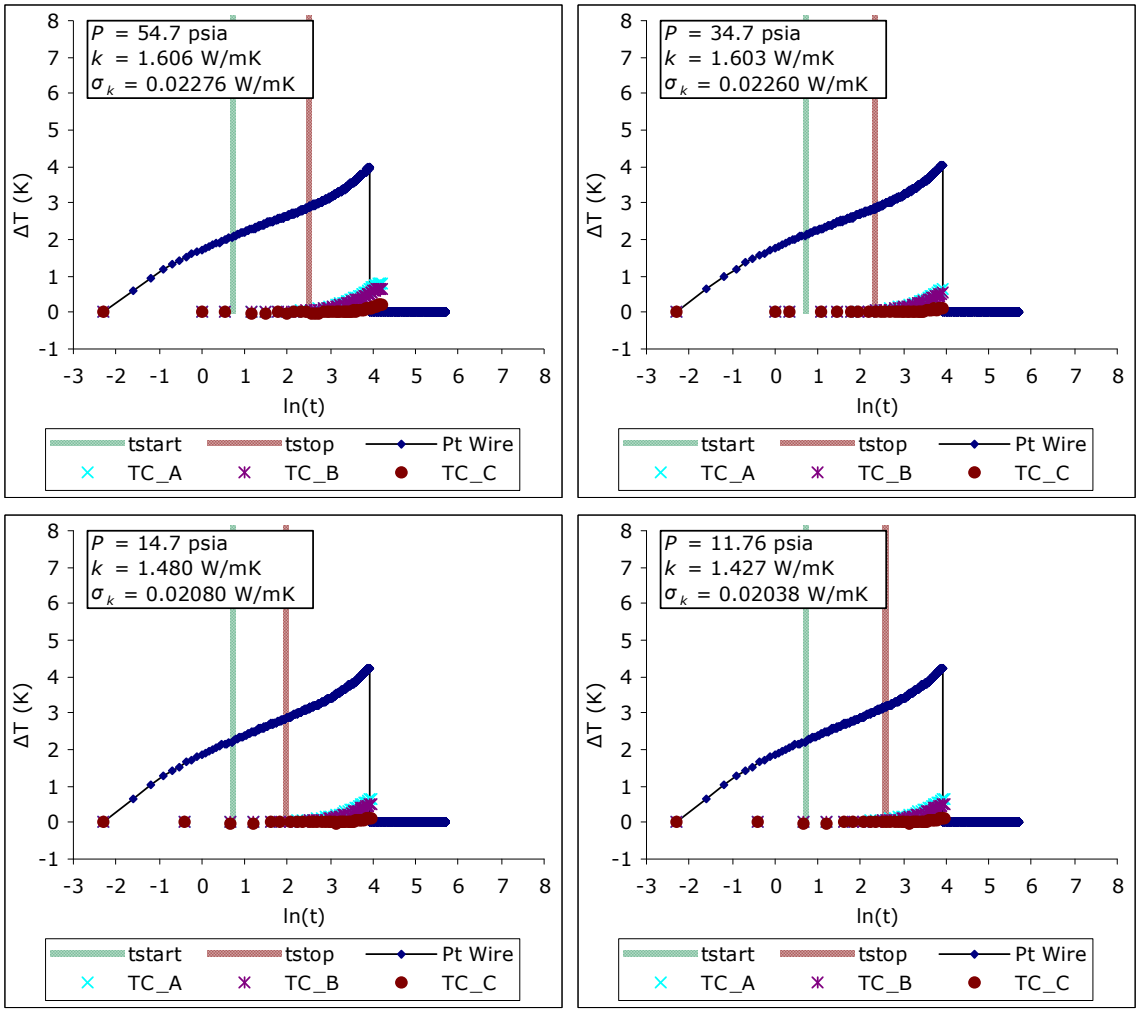

APPENDIX E – HYDRIDE INVESTIGATION RESULTS

E-1 Pressure Investigation (Measurements 1-6)

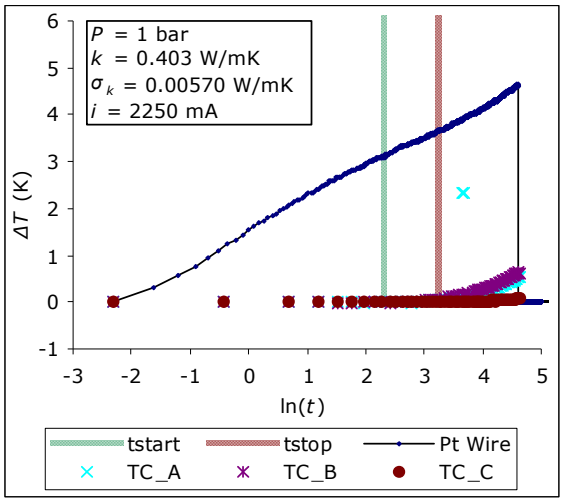

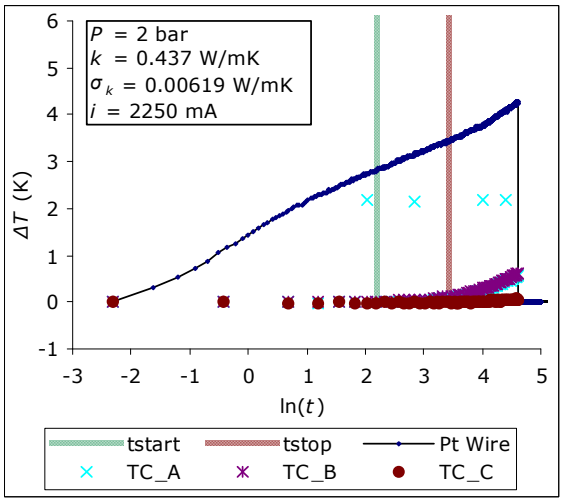

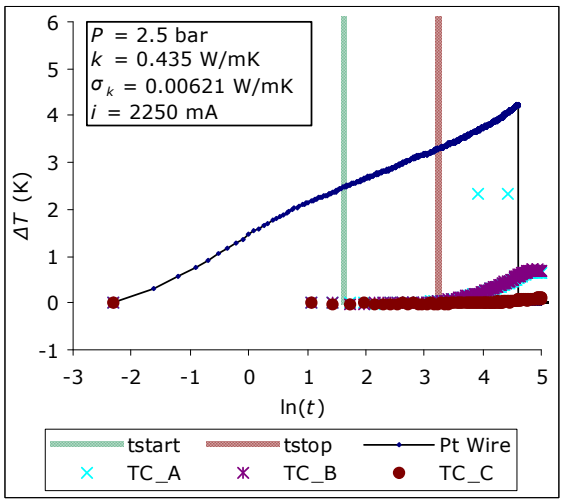

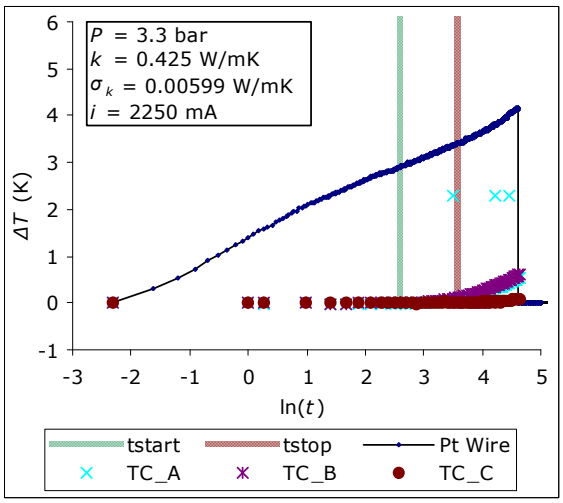

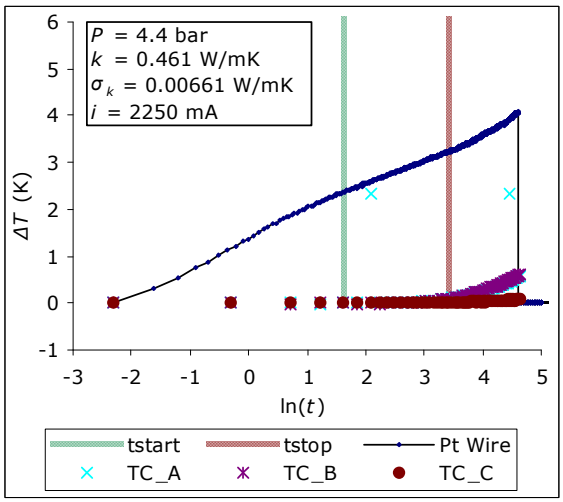

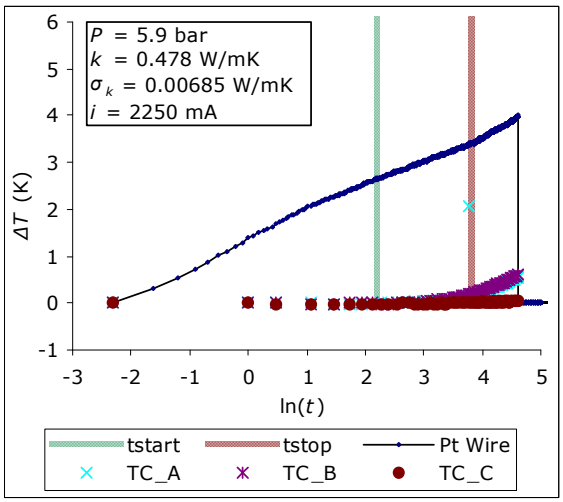

E-1 Pressure Investigation (Measurements 7-12)

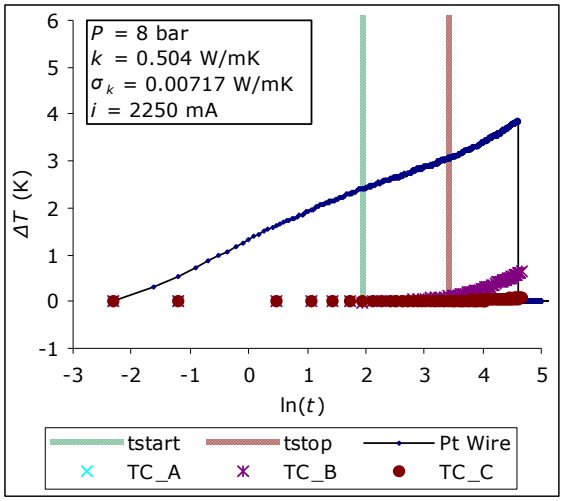

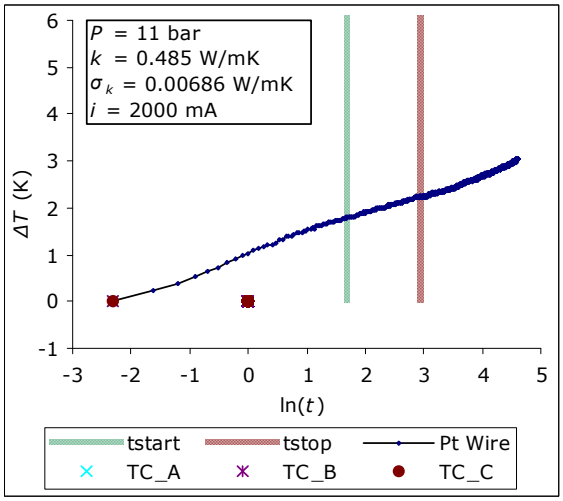

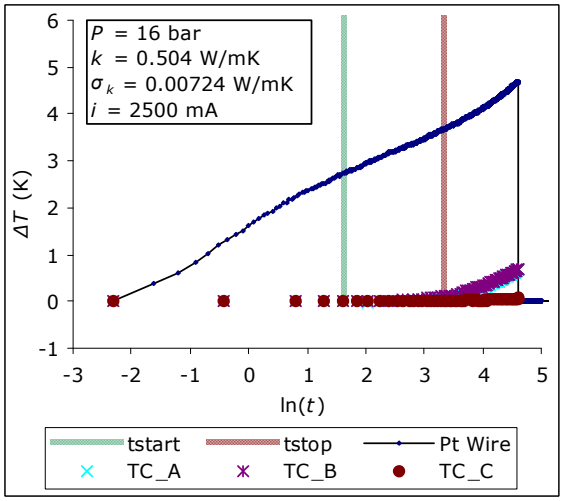

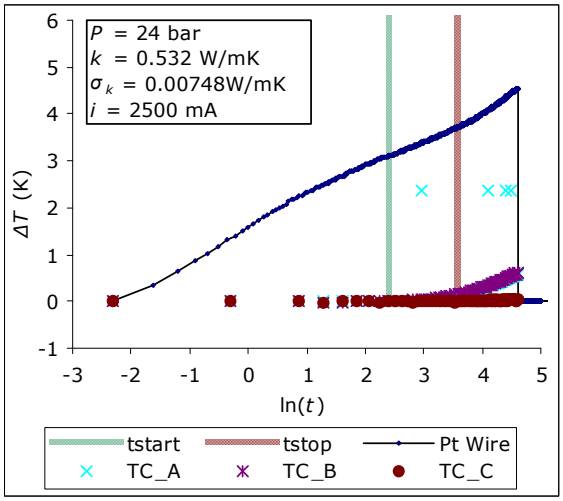

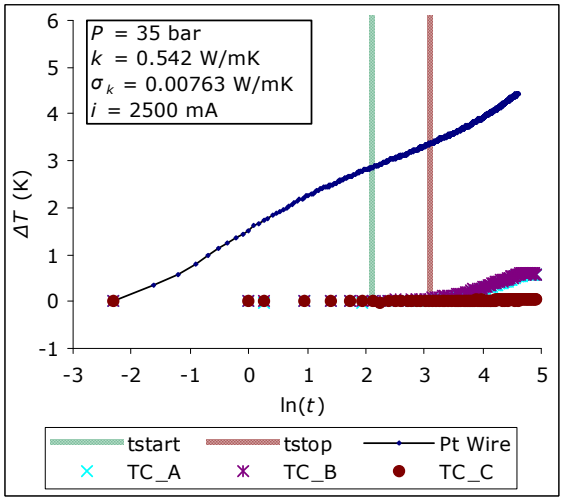

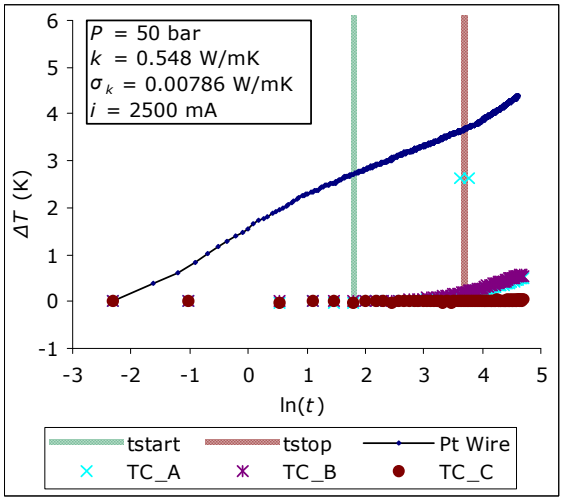

E-1 Pressure Investigation (Measurements 13-14)

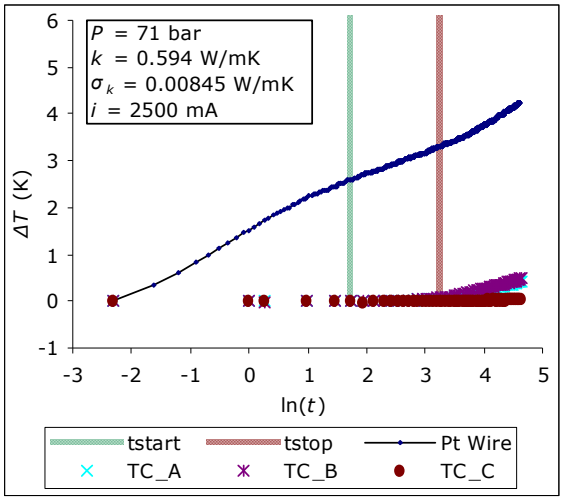

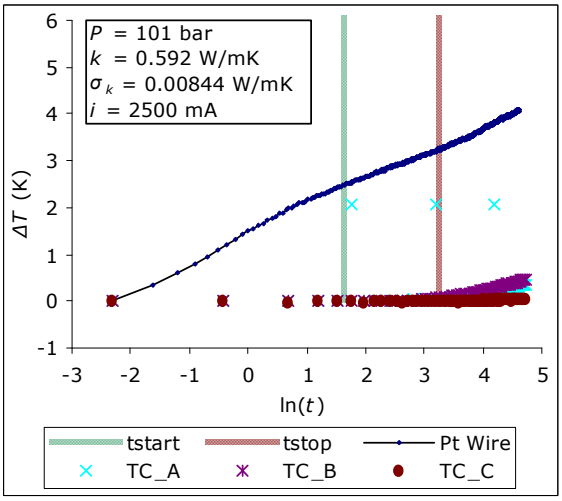

E-2 Composition Investigation (C_H = 4.68 wt%, measurements 1-5)

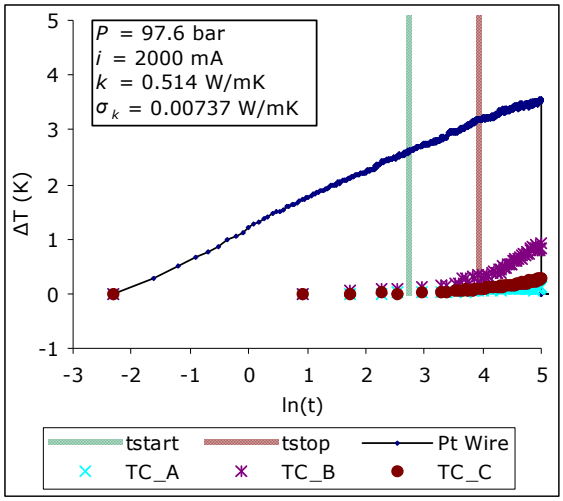

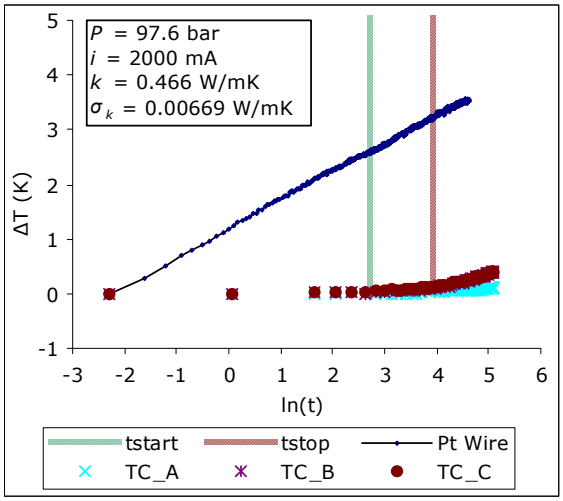

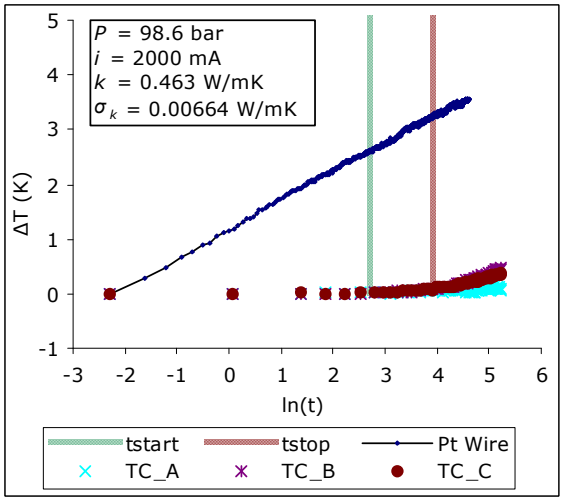

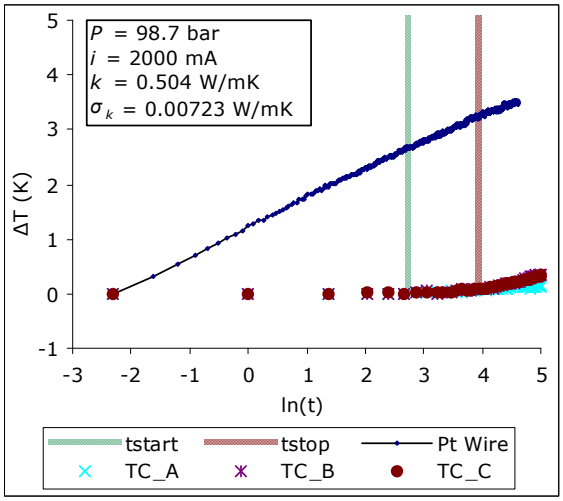

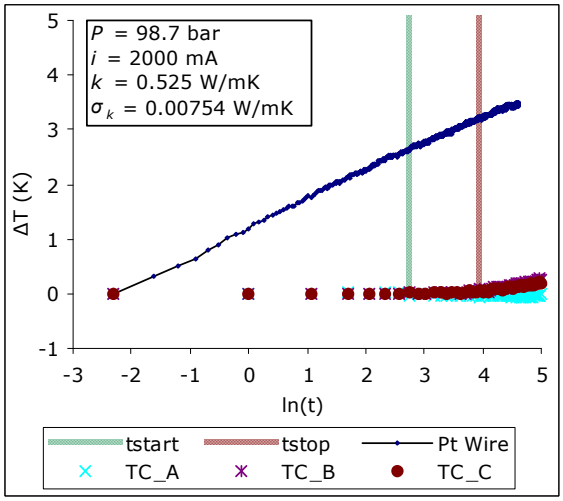

E-2 Composition Investigation (C_H = 4.62 wt%, measurements 1-5)

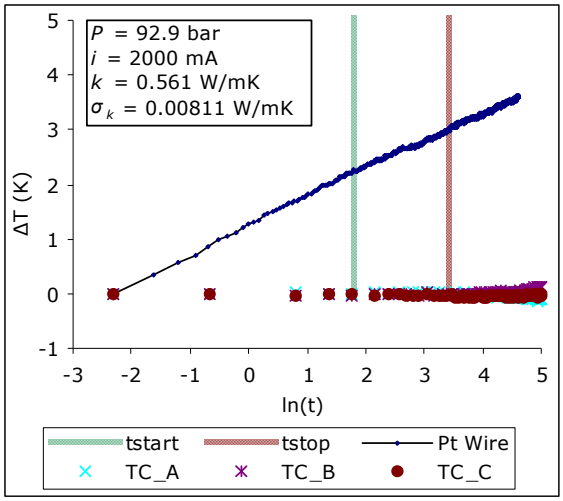

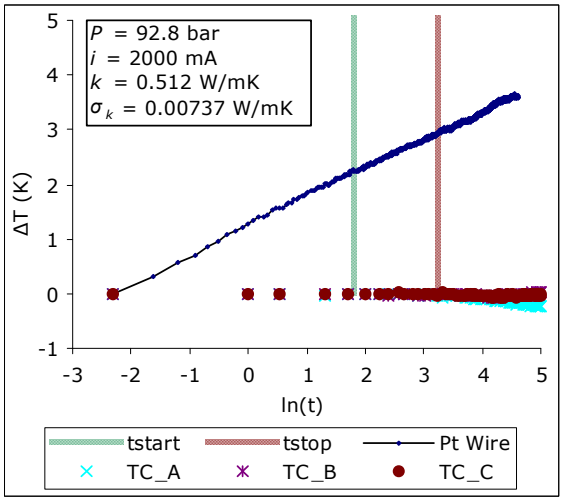

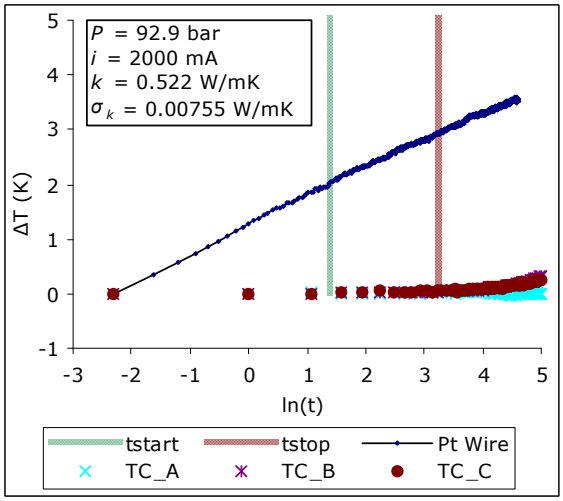

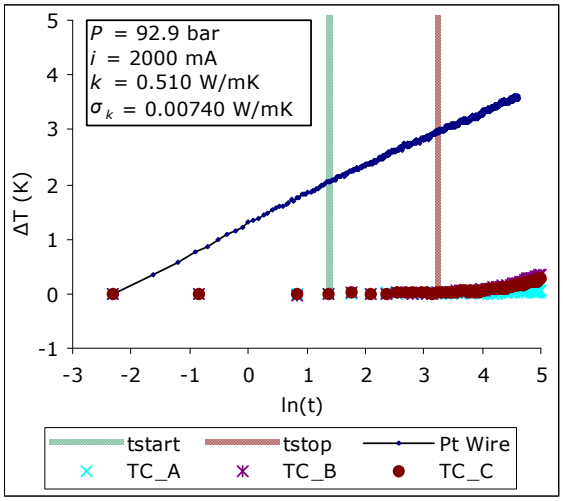

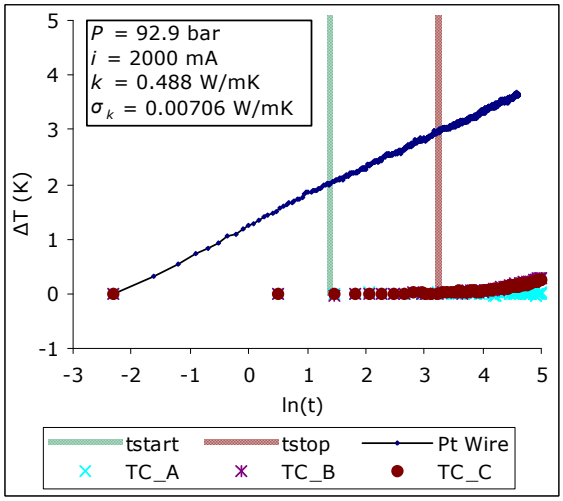

E-2 Composition Investigation (C_H = 4.41 wt%, measurements 1-5)

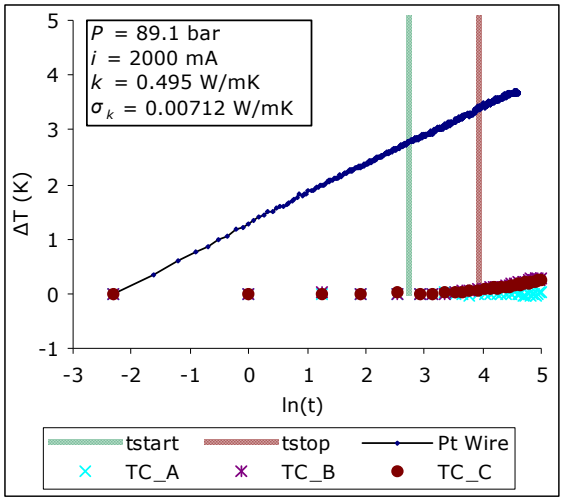

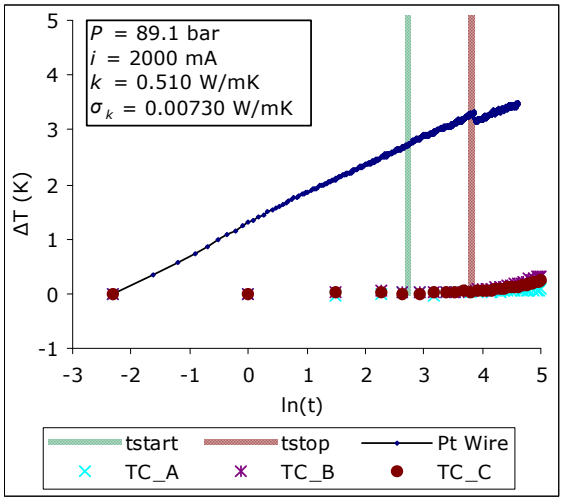

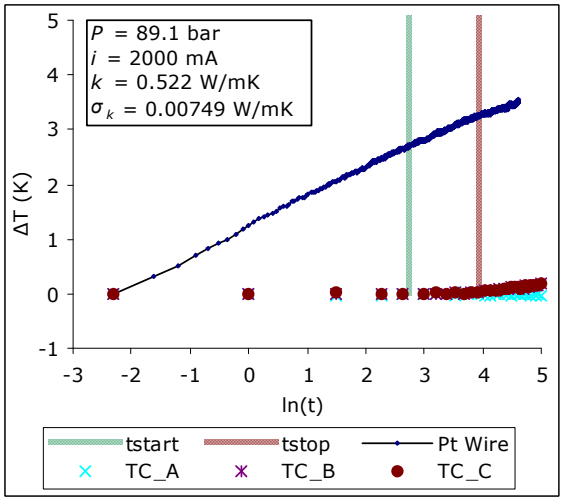

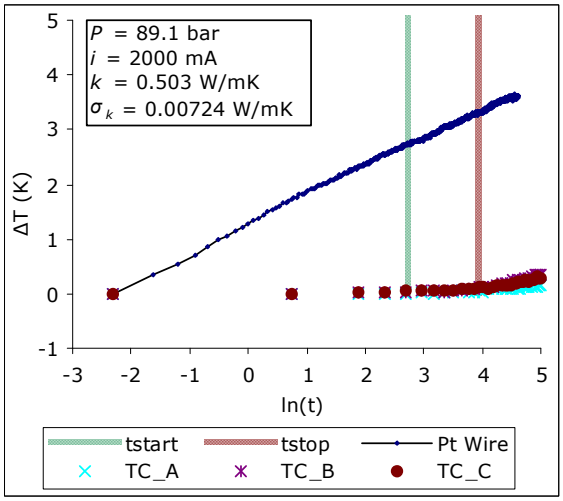

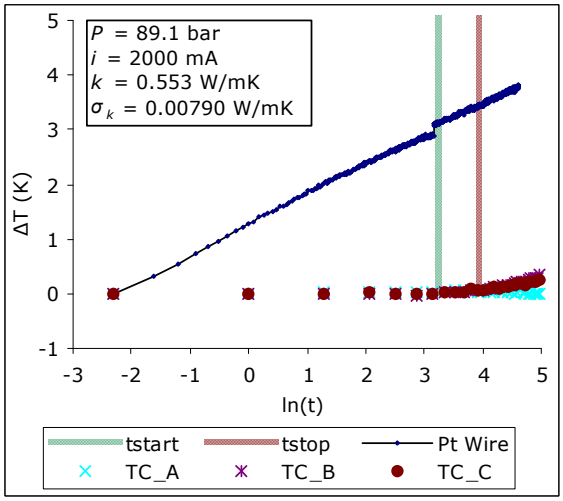

E-2 Composition Investigation (C_H = 4.23 wt%, measurements 1-5)

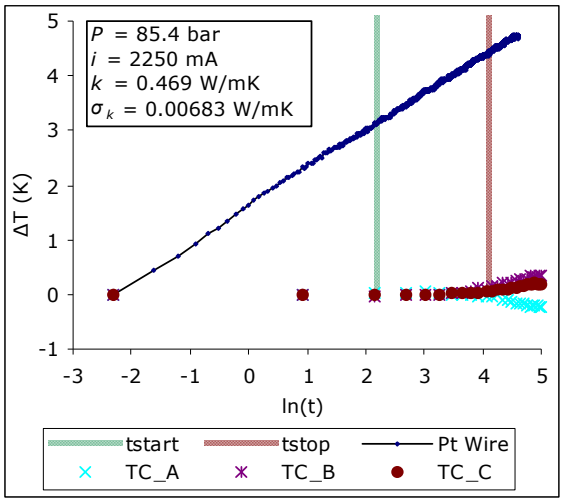

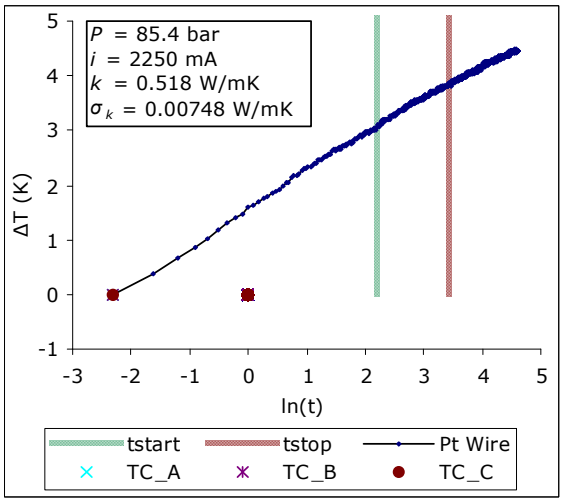

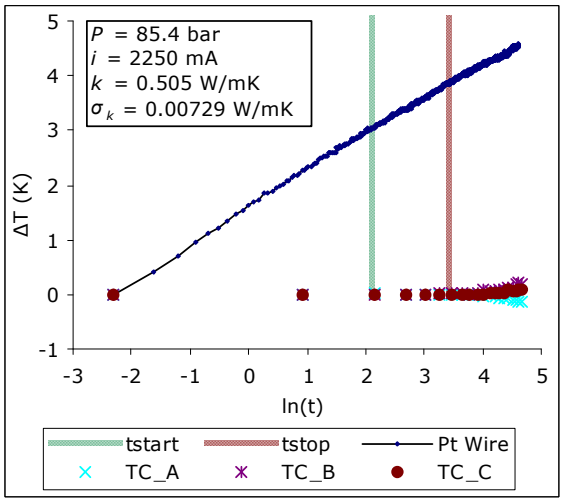

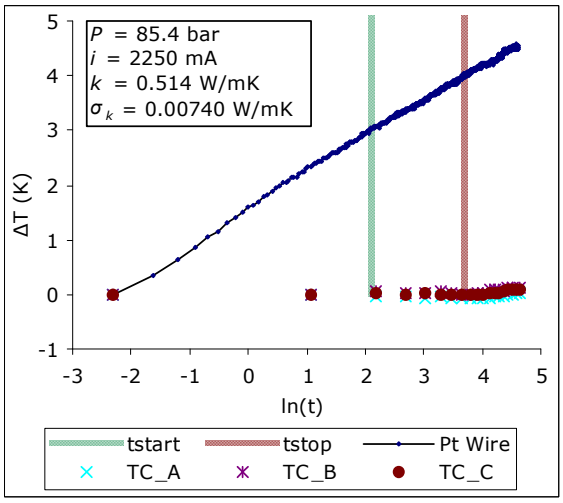

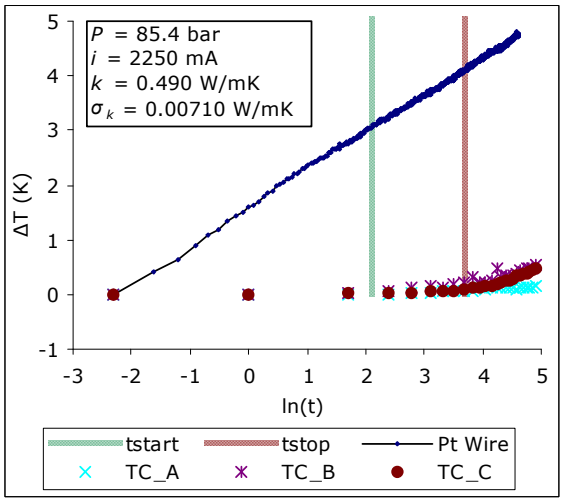

E-2 Composition Investigation (C_H = 2.70 wt%, measurements 1-5)

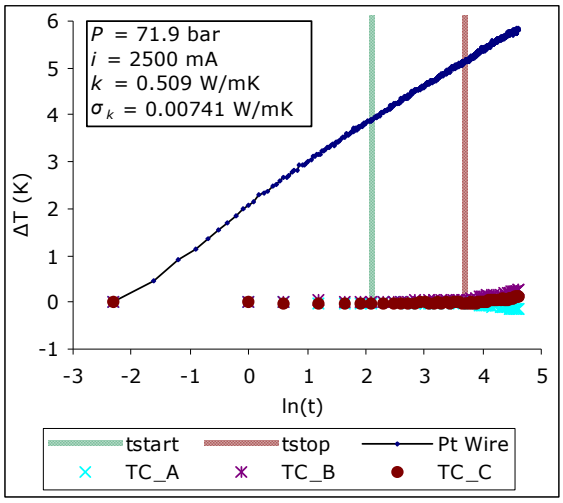

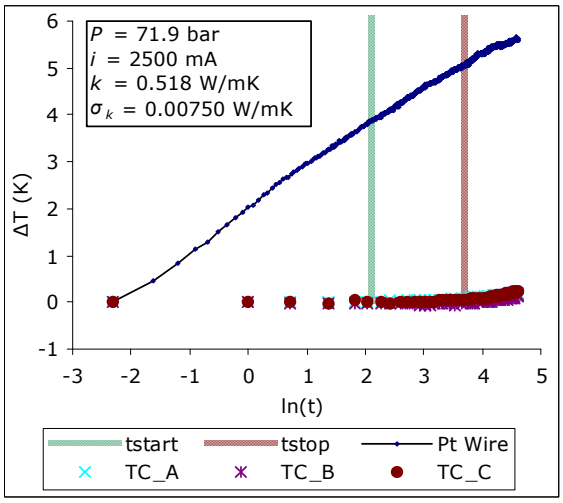

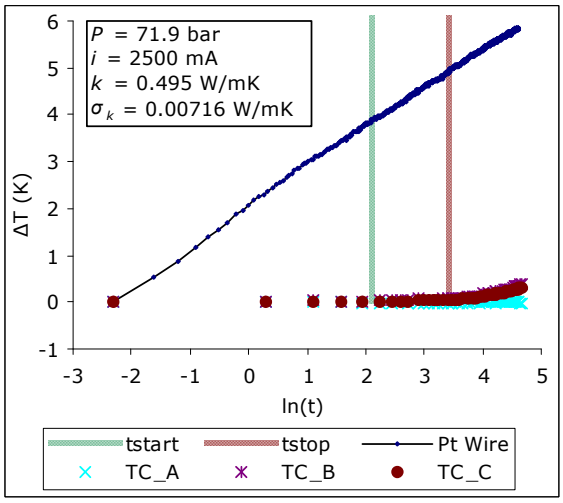

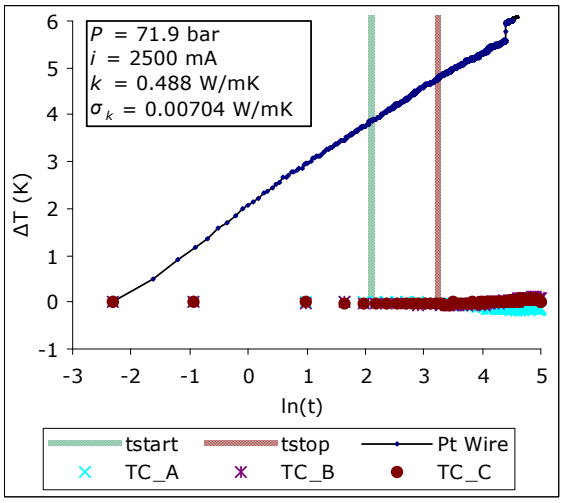

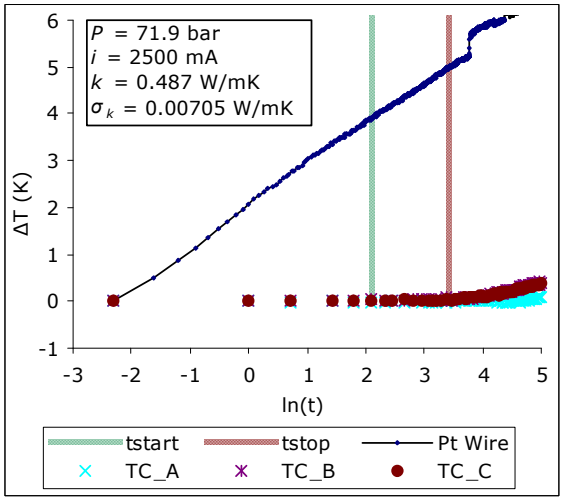

E-2 Composition Investigation (C_H = 2.11 wt%, measurements 1-5)